TECHNICAL INFORMATION SERIES

NO. 67SD358

TITLE Flow Field Computations for Blunt Bodies in Planetary Environments (Equilibirum)

AUTHOR C. Studerus, H. Rie, C. Kyriss, C. Dohner

AF 51547

FN-610-A (12-65)

FOR USE OF G-E EMPLOYEES ONLY

GENERAL ELECTRIC

TECHNICAL INFORMATION SERIES

Title Page

AUTHOR C. Studerus C. Kyriss, H. Rie C. Dohner	SUBJECT Radiative and Convective Heating	NO. 67SD358 DATE August 28, 1967
TITLE Flow Field Computations for Blunt Bodies in Planetary Environments (Equilibrium)		G.E. CLASS I GOVT. CLASS U
REPRODUCIBLE COPY FILED AT Library VFSTC L1343		NO. PAGES 162

SUMMARY

This study presents the variation of shock layer state and motion variables and the resulting variation of radiation and convective heat transfer, about two blunt bodies traveling hypersonically at zero angle of attack in an assumed Martian atmosphere whose composition (by volume) is 70% N_2 and 30% CO_2. The body configurations are a spherically-blunted 60-degree sphere-cone with spherically-rounded shoulders and a sphere-cap with sharp shoulders. The two free stream conditions for which calculations are made correspond to those encountered in a typical hyperbolic Martian entry trajectory at the point where maximum stagnation point radiative heat transfer might be expected, and to the flow conditions in a ballistic range facility which has been used to simulate the stagnation point heating environment expected for the hyperbolic entry condition.

KEY WORDS

Inviscid blunt body flow fields, laminar boundary layers, radiative heating, planetary environments.

INFORMATION PREPARED FOR Jet Propulsion Laboratory

TESTS MADE BY

AUTHOR C. J. Studerus C. Kyriss H. Rie C. V. Dohner

Studerus, C. Kyriss, H. Rie — C. V. Dohner

COMPONENT Aerodynamics Technology Component — Thermodynamics Tech. Comp.

APPROVED J. B. Arnaiz

J. B. Arnaiz, Manager, Aerodynamics Technology Component

JPL CONTRACT NO. 951647
28 AUGUST 1967

FLOW FIELD COMPUTATIONS FOR BLUNT BODIES IN PLANETARY ENVIRONMENTS (EQUILIBRIUM)

FINAL REPORT

PREPARED BY:

C. J. STUDERUS
C. L. KYRISS
H. RIE
C. V. DOHNER

This work was performed for the Jet Propulsion Laboratory, California Institute of Technology, sponsored by the National Aeronautics and Space Adminstration under contract NAS7-100.

GENERAL ELECTRIC
RE-ENTRY SYSTEMS DEPARTMENT
A Department Of The Missile and Space Division
P. O. Box 8555 • Philadelphia, Penna. 19101

SUMMARY

This study presents the variation of shock layer state and motion variables, and the resulting variation of radiative and convective heat transfer, about two blunt bodies traveling hypersonically at zero angle of attack in an assumed Martian atmosphere whose composition (by volume) is 70% N_2 and 30% CO_2. The body configurations are a spherically-blunted 60-degree sphere-cone with spherically-rounded shoulders and a sphere-cap with sharp shoulders. The two free stream conditions for which calculations are made correspond to those encountered in a typical hyperbolic Martian entry trajectory at the point where maximum stagnation point radiative heat transfer might be expected, and to the flow conditions in a ballistic range facility which has been used to simulate the stagnation point heating environment expected for the hyperbolic entry condition.

The computations of the shock layer flows were made on the basis of a separate non-radiating equilibrium inviscid flow field analysis, and an associated non-radiating equilibrium viscous boundary layer analysis, together with a calculation of radiation from this combined inviscid-viscous shock layer. The effect of self-absorption of the flow field is accounted for in the radiation calculations, and the effect of the radiation on the convective heating is evaluated.

The following conclusions can be drawn as a result of the computations performed in this study:

1. For the sphere-cap configuration, good simulation of the radiative heating is achieved near the shoulder while poor simulation is evidenced toward the stagnation point. For the sphere-cone configuration, good simulation occurs on the conical portion of the body, while poor simulation is achieved at the spherical nose and at the spherically-rounded shoulder.

2. Non-optically thin calculations are necessary, particularly in the case of the sphere-cap configuration.

3. Treatment of the radiation in a spectral manner is necessary for determination of the total radiative heating at a point.

4. The inviscid-radiative and convective-radiative coupling effects are negligible.

5. The peak radiative heating for the sphere-cone configurations occur near the rounded shoulder, whereas it occurs at the stagnation point for the sphere-cap configurations.

TABLE OF CONTENTS

LIST OF ILLUSTRATIONS

LIST OF ILLUSTRATIONS

LIST OF ILLUSTRATIONS

LIST OF TABLES

Section 1

INTRODUCTION

The work reported herein was performed by the General Electric Company Re-entry Systems Department, Philadelphia, Pa. under Jet Propulsion Contract No. 951647. The authors would like to acknowledge the valuable assistance of the following consultants, who were active participants in the program: Mr. W. G. Browne for the determination of the equilibrium compositions, the thermodynamic and transport properties of the gas mixture, and Mr. J. S. Gruszczynski for the determination of the radiative properties of the gas mixture in the form of spectral absorption coefficients. The authors also acknowledge the considerable assistance of Mr. P. C. Townsend and Mr. A. Birnbaum in obtaining and presenting the numerical results of the inviscid and viscous analyses, respectively, and of Mr. M. Y. Goodman and Mr. R. E. Dallison for the programming analysis of the Hot Gas Radiation Program.

1.1 STUDY OBJECTIVE

The objective of this study is to determine, by numerical techniques, the state and motion variables and heat transfer distributions about two blunt bodies traveling at hypersonic velocities in an assumed Martian atmosphere whose composition (by volume) is 70% N_2 and 30% $C0_2$. Calculations are made at two free stream conditions. One free stream condition is similar to that encountered in a typical hyperbolic Martian entry trajectory at the point where maximum stagnation point radiative heat transfer might be expected. The other free stream

condition corresponds to the flow conditions in a ballistic range facility which has been used to simulate the stagnation point heating environment expected for the hyperbolic entry condition, and from which experimental heat transfer data has been obtained. The results of the theoretical study can then be used to evaluate the experimental measurements and to determine possible scaling procedures for utilizing the experimental data at conditions of flight.

1.2 STUDY CONFIGURATIONS

The blunt body configurations for which calculations are made are presented in Figure 1-1. The first is a spherically-blunted 60-degree half-angle cone with spherically rounded shoulders; the second is a sphere-cap with sharp shoulders. The base diameter for each of the configurations is specified with the free stream conditions.

1.3 STUDY FREE STREAM CONDITIONS

The two free stream conditions for which flow field and heating computations are made are presented in Table 1-1.

Table 1-1. Free Stream Conditions

	Ballistic Range	Hyperbolic Entry
Mach No.	15.0	31.7
Flight Velocity	15,800 ft/sec	19,600 ft/sec
Ambient Density	5×10^{-4} slugs/ft^3	10^{-6} slugs/ft^3
Ambient Temperature	540°R	180°R
Ambient Pressure	409.1 lbs/ft^2	.2727 lbs/ft^2
Atmospheric Composition (by volume)	70% N_2 - 30% CO_2	70% N_2 - 30% CO_2
Base Diameter	0.4 inches	12.0 feet

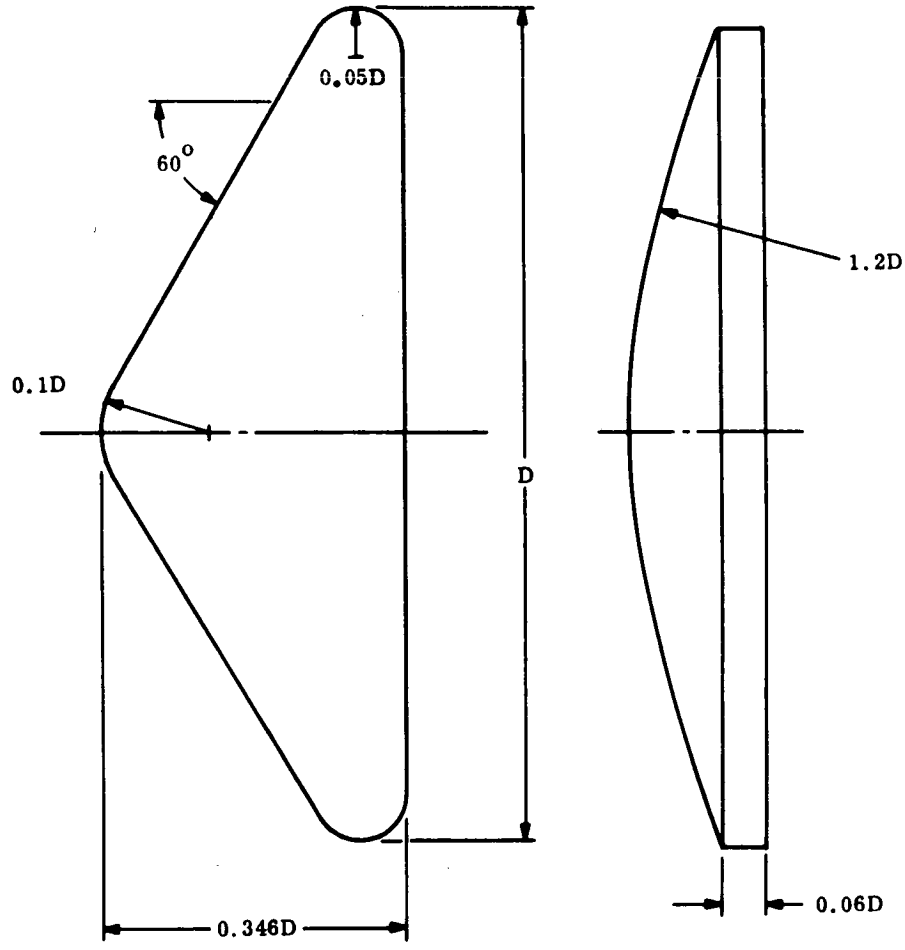

Figure 1-1 Study Configurations

1.4 STUDY CASES

The two proposed aerodynamic configurations together with the two free stream conditions represent four study cases which are analyzed. These study cases are:

Case 1 - Sphere-Cone - Hyperbolic Entry Case

Case 2 - Sphere-Cap - Hyperbolic Entry Case

Case 3 - Sphere-Cone - Ballistic Range

Case 4 - Sphere-Cap - Ballistic Range

The analytical flow model used for these analyses is discussed in Section 2. The determination of the gas properties is described in Section 3 and the methods of analyses discussed in Section 4. The results of the computations are presented in Section 5.

Section 2

ANALYTICAL FLOW MODEL

The general fluid dynamic equations describing a steady-state, viscous, radiating shock layer flow in chemical equilibrium are the continuity equation, the Navier-Stokes equations, and a general energy equation which includes the effects of radiant emission and absorption:

$$\text{div } (\rho \bar{V}) = 0 \tag{2-1}$$

$$\bar{V} \cdot \text{grad } \bar{V} = -\frac{\text{grad } p}{\rho} + \frac{1}{\rho} \text{ div } \bar{\bar{\tau}} \tag{2-2}$$

$$\rho T \ \bar{V} \cdot \text{grad } S = \rho \bar{V} \cdot \text{grad } H = \text{div } \bar{Q} + \mu \Phi \tag{2-3}$$

where $\bar{\bar{\tau}}$ is the viscous stress tensor

$\bar{Q}$ includes the conductive and radiative heat transfer

Φ is the dissipation function

H is the total enthalpy

S is the entropy

These equations display the two modes of coupling present:

a. The viscous-inviscid coupling due to the presence of the viscous terms in the momentum and energy equations,

b. the radiation coupling due to the presence of the radiation term in the energy equation.

Each of these coupling modes will be examined to determine its strength

with respect to the specific configurations and flight conditions of this study.

2.1 VISCOUS-INVISCID COUPLING

The structure of the viscous, non-radiating, hypersonic shock layer in the forward stagnation regions of blunt entry vehicles has been studied by many investigators (References 2.1 through 2.12). The studies of Goldberg (Reference 2.12) characterize such flow fields in terms of three dimensionless quantities:

$$\text{the shock Reynolds number} = Re_s = \rho_s u_s R_N/\mu_s = \rho_\infty u_\infty R_N/\mu_s \ , \qquad (2.4)$$

$$\text{the normal shock density ratio} = \epsilon = \rho_\infty/\rho_s \ , \qquad (2.5)$$

$$\text{the Prandtl number} = Pr = \mu C_p/k \qquad (2.6)$$

In flows of sufficiently high Reynolds number, the shock layer can be analyzed as two distinct flow fields: an inviscid flow bounded by the bow shock and the body surface, and a viscous boundary layer flow along the surface of the body. With decreasing Reynolds number, departures from predictions utilizing boundary layer theory become evident. One significant effect is that the ratio of viscous boundary layer thickness, δ, to shock detachment distance, Δ, is no longer small, i.e., $\delta/\Delta \ll 1$ is no longer valid. Under such conditions, the order of magnitude reduction of the basic equations leading to the classical boundary layer

equations must be re-examined to determine the proper governing equations.

In the analysis of Reference 2. 2, the Navier-Stokes equations were suitably expanded in a body-oriented coordinate system in the forward region of a blunt body and all terms of order $1/Re_s$ and larger were retained. This produced the so-called low Reynolds number equations. The method of separation of variables was used to reduce these low Reynolds number equations to a set of coupled non-linear ordinary differential equations which were solved by numerical methods, subject to boundary conditions which included the effects of transport of mass, momentum, and energy in a thickened shock wave concentric with the body. Numerical solutions were obtained over a wide range of flight conditions in air and the results correlated.

Two significant results of the study can be used to evaluate the applicability of utilizing the usual (high Reynolds number) boundary layer equations in a given flow situation. First, the viscous layer thickness produced by the low Reynolds number equations is less than that predicted by classical boundary layer theory. Therefore,

$$\delta/\Delta \ll 1 \qquad .(2\text{-}7)$$

is a conservative test of the applicability of the usual boundary layer theory. Second, since the viscous layer is thinner in the low density

case, the gradients are greater, producing larger heat transfer rates than predicted by the usual boundary layer theory. Figure 2-1, taken from Reference 2.12, presents the ratio of heat transfer based on various viscous layer solutions to the heat transfer based on the usual boundary layer solutions. The basic parameter used to correlate this ratio is $\epsilon^2 Re_s$. Goldberg's separation of variables method of solution produces the heat transfer rate as the sum of two separate quantities Q_{w_1} and Q_{w_2}, combined as:

$$Q_w = Q_{w_1} \cos^2(s/R_N) + Q_{w_2} \sin^2(s/R_N) \tag{2-8}$$

where s is the distance along the surface. Therefore at the stagnation point $Q = Q_{w_1} = \dot{q}_{c_{st}}$.

The above results can be used to make both a priori predictions and a posteriori evaluations of the validity of using of an uncoupled inviscid flow plus boundary layer flow calculations. In this section of the report, only the a priori predictions are discussed. The a posteriori evaluations are discussed in Section 5.

From normal shock calculations, values of ϵ and Re_s can be determined for the cases of interest.

Table 2.1 Bow Shock Parameters

Case	Body	Flight Condition	ϵ	Re_s	$\epsilon^2 Re_s$
1	Sphere-Cone	Hyp. Entry	.0645	7680.	32.
2	Sphere-Cap	Hyp. Entry	.0645	92200.	385.
3	Sphere-Cone	Ball. Range	.0852	9290.	67.
4	Sphere-Cap	Ball. Range	.0852	111500.	809.

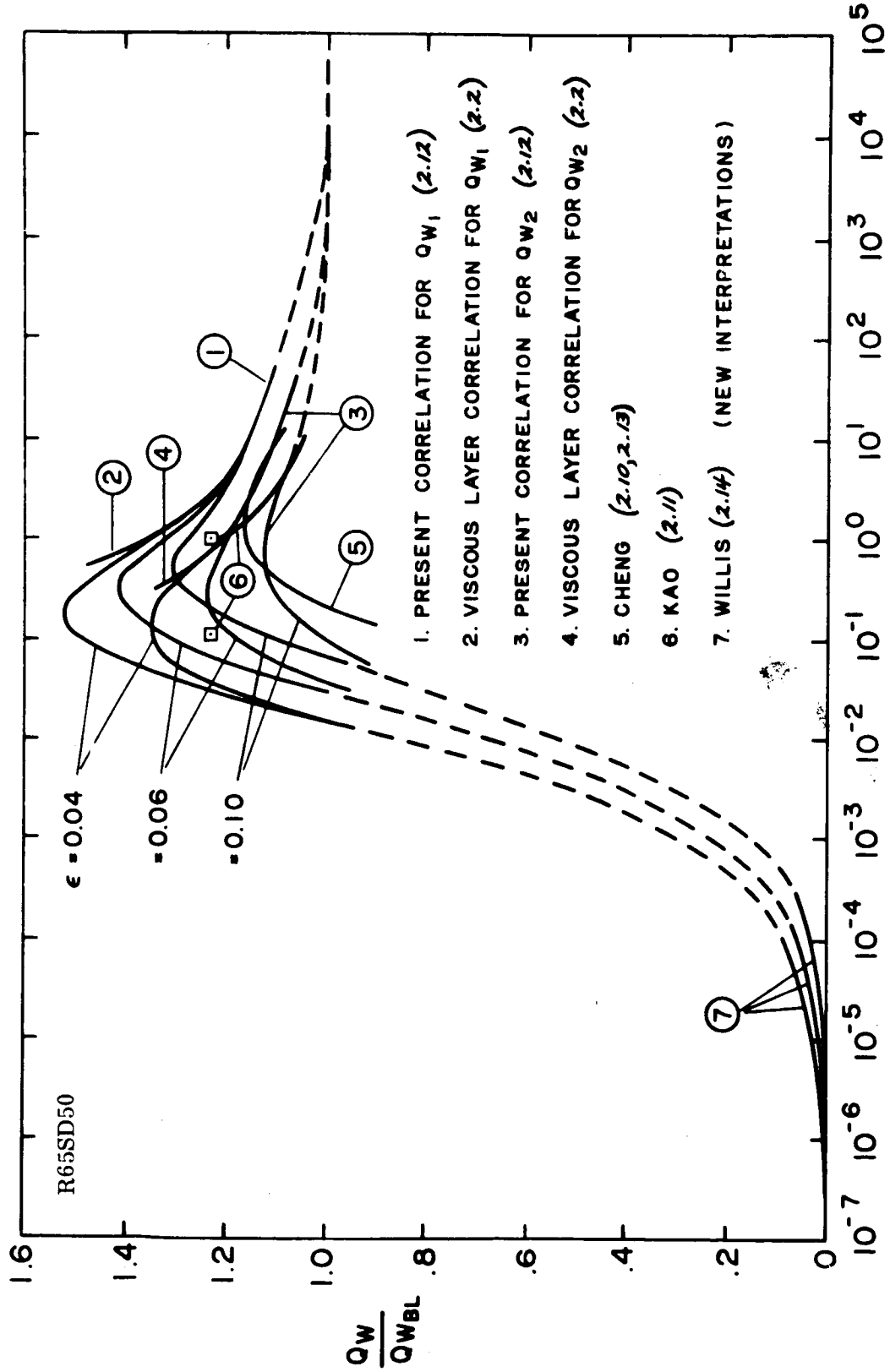

FIGURE 2-1 NORMALIZED HEAT TRANSFER FROM STAGNATION REGION VISCOUS LAYER SOLUTIONS

The lowest value of $\epsilon^2 Re_s$ is 32 for the low density, small nose radius Sphere-cone Hyperbolic Entry Case. Based on Figure 2-1, the increase in heat transfer to be expected by use of a low Reynolds number form of the Navier-Stokes and energy equations, rather than the usual boundary layer equations, is approximately ten percent. For the ballistic range cases, the increases will be much less. Therefore, the determination of the convective heating can be made on the basis of an uncoupled viscous flow model in which the shock layer is treated as separate inviscid and boundary layer flows.

2.2 RADIATION COUPLING

Consider now the radiation coupling. In the radiationless case the entropy and the total enthalpy are constant along streamlines in the inviscid flow field. With radiation present, the total energy is reduced by the amount radiated to other parts of the flow field. The computation of a radiating flow field can therefore be divided into two parts: (1) the determination of the local radiant intensity along with the usual local flow field properties, such as pressure, temperature, density, and velocity, and (2) the computation of the resulting radiant emission or absorption of energy by a fluid element (given the state of the fluid). Obviously, the magnitude of the energy of a local fluid particle, which determines the amount radiated to other parts of the flow field, is itself

dependent upon the dynamic and thermal behavior of, and the energy absorbed from, the other parts of the flow field. This is the inviscid flow field coupling or the direct dependence of one particle of the flow on the remainder of the flow field. A second effect of the radiative coupling is the reduction in radiative heat transfer which may occur when appreciable amounts of energy are radiated from the flow field, thus reducing the enthalpy and temperature levels in the flow. A simple measure of these coupling effects is the ratio of the energy loss due to radiation to the total flow energy. If this ratio is small, the flow field can be considered to be uncoupled; i.e., the flow field can be computed independently of the radiation, since the total enthalpy is essentially unchanged. Also, the radiation heat transfer should then be essentially that value predicted by utilizing the uncoupled flow field values.

Again, a priori predictions of the magnitude of the energy ratio, or coupling parameter can be made. (The a posteriori evaluations are left for Section 5). For the hyperbolic entry into the Martian atmosphere, the total equilibrium radiance, J_t, is estimated to be on the order of 0.2 watt/cm^3-str. This estimate is based on the theoretical radiance prediction over all wave lengths for a 60 percent CO_2 - 40 percent N_2 gas mixture given in Figure 2-2 (Reference 2.15) at $V = 19,600$ ft/sec., normalized by the density ratio to the 1.45 power.

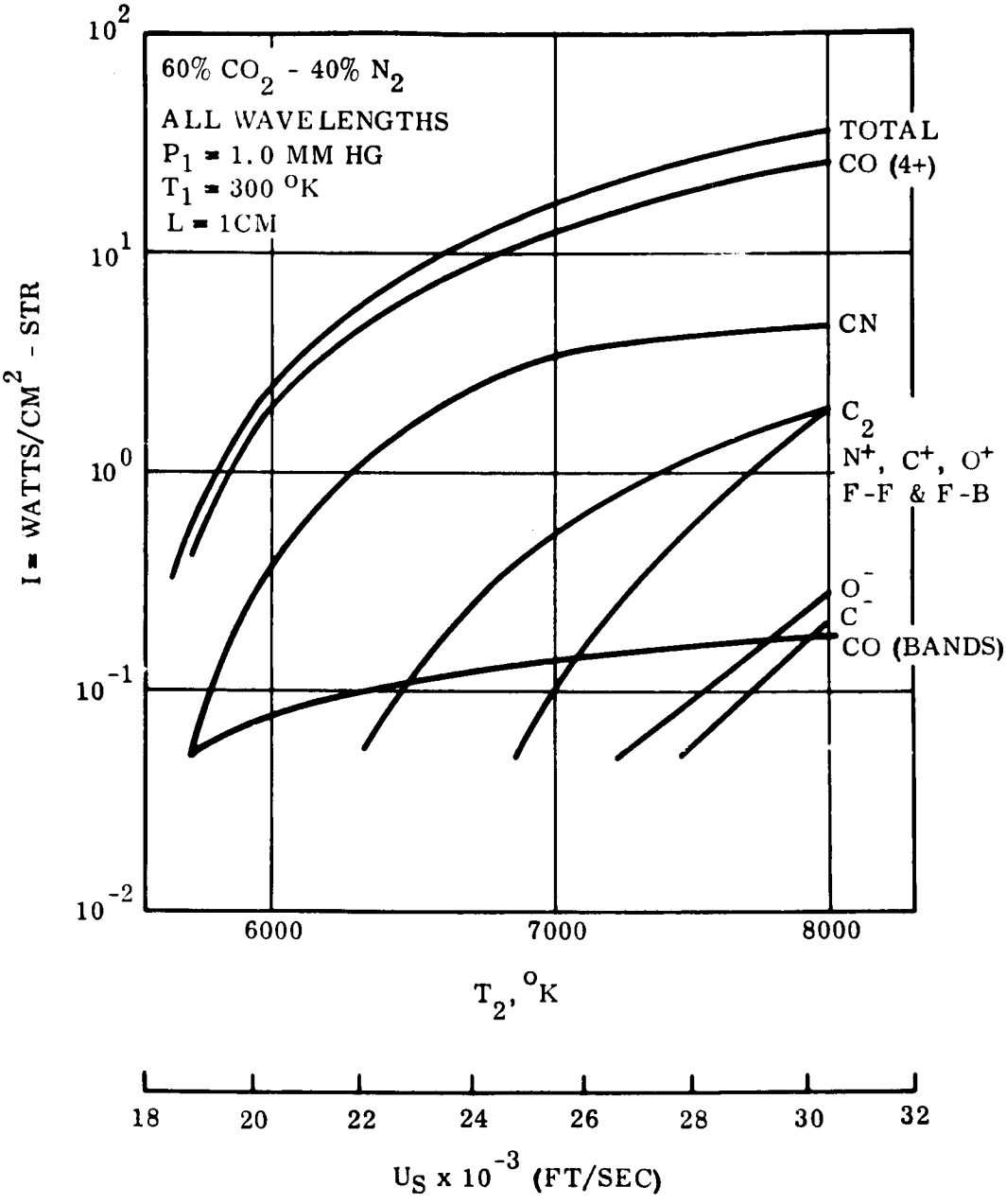

Figure 2-2 Radiance of Species for 60% CO_2 - 40% N_2 Gas Mixture

Since the total radiance of this mixture is predominantly due to large CO (4+) contribution, this estimate should provide a reasonable upper bound to the radiance expected in a 30 percent CO_2 - 70 percent N_2 system. Thus the total energy emission rate per unit volume, E_t, is approximately 2.5 watts/cm^3 for the hyperbolic encounter. The total radiation results of Thomas and Menard (Reference 2.16) for a 70% N_2 - 30% CO_2 mixture confirm this general level, Figure 2-3. Their total radiation values are normalized by the density ratio to the 1.64 power. For the hyperbolic entry case, the above total emission rate corresponds to a normalized total radiation $(I/(\rho/\rho_o)^{1.64})$ of approximately 10^{+4} watts/cm^3. In the stagnation region, assuming that the shock layer is optically thin, the energy loss per unit time and flow area is $E_t \Delta$, where Δ is the shock standoff distance. For the case of the sphere-cap, the shock standoff distance is assumed equal to the uncoupled value of .05 R_N corresponding to the normal shock density ratio of .0645 (See Section 5.1). The estimated radiated energy is then 48 Btu/ft^2sec.

The total available energy stored in the fluid crossing the shock is $\rho_s V_s H = \rho_\infty V_\infty H$, also per unit time and flow area. Then for the sphere cap in the hyperbolic encounter, the ratio of the energy lost from the shock layer to the total available energy stored in the shock layer is $\Gamma = 0.01$. Thus for the worst case to be considered in this study, the

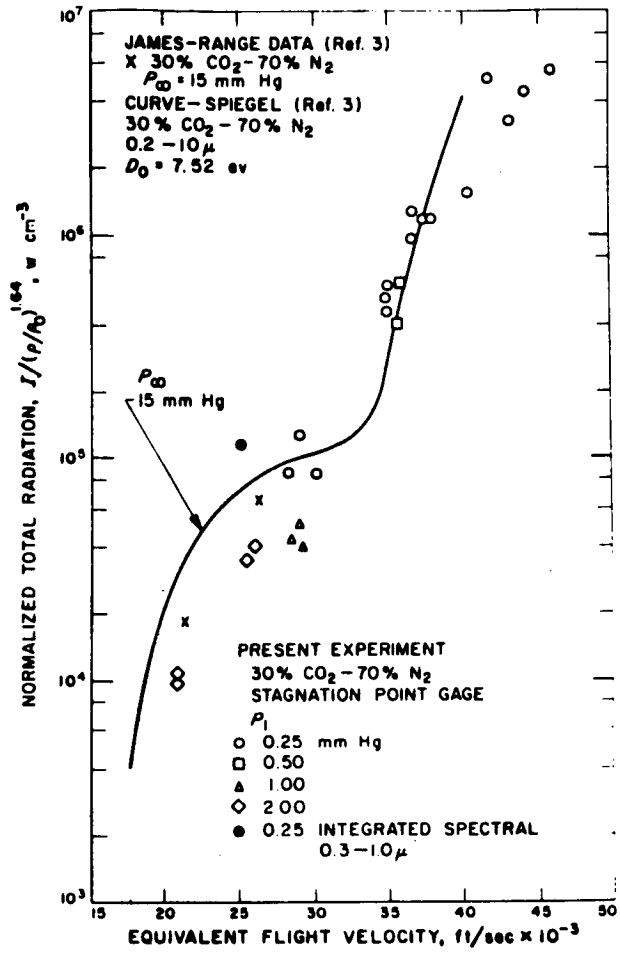

Figure 2-3 Stagnation Point Total Radiation and Integrated Spectral Measurements

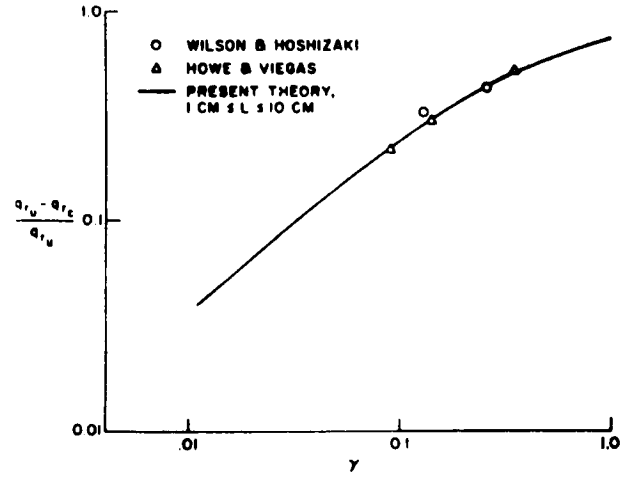

Figure 2-4 Effect of Coupling on Reduction of Radiation Heat Transfer

radiation coupling factor Γ is less than 1 percent in the stagnation region. Using a simple stagnation flow model, Goulard (Reference 2.17) has shown that for $\Gamma = 0.01$, the radiation flux at the wall is within 10 percent of the uncoupled prediction. Furthermore, when self absorption is considered, the coupling becomes even more insignificant.

Gruszczynski and Warren (Reference 2.18) have attempted to evaluate the second coupling effect by utilizing the uncoupled radiative heating results of Biberman (Reference 2.19). For shock layer thicknesses ranging from 1 to 10 cm., they calculated the Biberman $\dot{q}_r$ values for a given flight condition, assigned the radiated energy loss uniformly across the shock layer (isothermal assumption) to produce a lower average stagnation region enthalpy, recalculated $\dot{q}_r$ for the new enthalpy condition, and iterated the procedure for better accuracy. The resulting reduction of radiative heating as a function of the coupling ratio is shown in Figure 2-4. The calculation procedure seems in agreement with results of Wilson and Hoshizaki (Reference 2.20) and Howe and Viegas (Reference 2.21). For a value of the coupling parameter of .01, the reduction in radiative heating is expected to be only 5 percent of the uncoupled value.

2.3 NUMERICAL METHODS OF SOLUTION

In order to predict the heat transfer to a vehicle entering the atmosphere, a detailed accurate description of the flow field about the

vehicle is required. The need for accuracy is especially acute for the vehicles which have "irregular" shapes. The irregular shape causes the existence of very large gradients in the flow field - both along the surface and normal to it. The gradients along the body surface will no doubt have a pronounced effect on the convective heating to the body through influences on the boundary layer. Radiative heating depends on the distribution of the flow variables throughout the shock layer, not simply the conditions on the body surface. Radiative heating, then, will be greatly influenced by the gradients normal to the body.

The problem of determining flow fields about blunt bodies has received considerable attention in the past. For axisymmetric bodies at zero angle of attack, three broad classes of numerical methods have been developed. These are:

a. "Indirect" methods which begin from an assumed shock shape and find the body which produced it,

b. "Direct" or"continuity" methods which begin with the proper body shape and iterate to find the flow field by assuming, for example, a sequence of shock shapes and body pressure distributions, and

c. "The method of integral relations" in which the distributions of flow variables across the shock layer are assumed in such a manner that the governing equations can be reduced to relate

conditions at the shock to conditions at the body by means of a set of ordinary differential equations.

The indirect method is widely used for the prediction of axisymmetric flow fields. In general, indirect methods work quite well for regular bodies which are not too far from spheres. They do not work well (or possibly do not work at all) for irregular bodies which have relatively sharp corners influencing the region of locally subsonic shock layer flow. The reason they do not work for such bodies is traceable to the insensitivity of shock shapes to body shapes, i.e., because bodies which are radically different produce shocks which are only slightly different.

The method of integral relations is as widely used as the indirect methods. The method yields fairly accurate shock shapes and body pressure distributions for regular bodies but is rather poor in providing the details of the flow between the body and shock (Reference 2.22) at least for a "one strip" approximation. Because of this poor representation of details within the field, it is questionable that this method has any value for flows in which large gradients of flow properties normal to the body are important. The flow about irregular bodies of the Apollo type is of this class. The use of more strips may improve the results, but it is not known whether or not this is the case. There is a definite possibility that the use of a large number of strips will result in numerical instabilities similar to those encountered in

indirect methods.

Direct or continuity methods are not quite as widely used as indirect methods. The method used at GE-RSD (See Section 4.1) over the past ten years is such a direct method and has been successfully applied to a wide range of re-entry vehicle problems. For equilibrium conditions in air, a veritable library of solutions have been obtained covering a Mach number range from 2 to 36 and altitudes from 20,000 to 300,000 feet. For general configurations like sphere cones, solutions have been obtained over a wide range of cone angles. Furthermore, the direct method is capable of treating irregular bodies of the Apollo type (Reference 2.24). Results of typical calculations for bodies in planetary atmospheres are presented in Reference 2.25.

2.4 SUMMARY OF TECHNICAL APPROACH

In light of the preceding discussions of the nature of the flow model and the types of numerical methods, the following technical approach was utilized in the study. The computation of the shock layer flows was accomplished on the basis of a separate non-radiating equilibrium inviscid flow field analysis, and an associated non-radiating equilibrium viscous boundary layer analysis, together with a calculation of radiation from this combined inviscid-viscous shock

layer (wherein the effect of self-absorption of the flow field is taken into account and the effect of the radiation on the convective heating is also determined).

The following guidelines were followed in the course of the study:

a. The complete shock layer or flow field was considered to be in the continuum flow regime.

b. The gas was assumed to be in thermal and chemical equilibrium.

c. The angle of attack of the body with respect to the flight path was assumed to be zero.

d. The flow region near the body surface was considered as viscous and hence was treated as a boundary layer flow.

e. The fluid model included the effects of dissociation and ionization on the flow field and heat transfer modes.

f. The flow field and heating analyses were accomplished through computerized numerical techniques utilizing a minimum number of simplifying assumptions.

Section 3

GAS PROPERTIES

3.1 RANGES OF TEMPERATURE AND DENSITY

The thermodynamic, transport, and radiative properties were determined over ranges of temperature and density which were expected to include the extremes produced by both sets of free stream conditions. At the beginning of the study, computations of flow conditions downstream of normal and oblique shocks were made for both free stream conditions using two available model planetary atmospheres:

9% CO_2 - 90% N_2 - 1% A

48.8% CO_2 - 51.2% N_2

Based on these computations, the maximum expected flow conditions were:

$T_{max} = 7000^{o}K$

$\left(\rho/\rho_0\right)_{max} = 3.0$ where $\rho_0 = 1.29313(10^{-3})$ gr/cm^3

The minimum expected flow conditions were the lowest free stream condition.

The thermodynamic properties of the 30 percent CO_2 - 70 percent N_2 gas mixture were therefore evaluated over the following ranges of temperature and density:

$100^{o}K \leq T \leq 500^{o}K; \quad \Delta T = 100^{o}K$

$500^{o}K \leq T \leq 7000^{o}K; \quad \Delta T = 500^{o}K$

and

$$10^{-5} \leq \rho/\rho_o \leq 10^{1}; \qquad \Delta(\rho/\rho_o) = 10^{.5}$$

The transport properties were evaluated over the following ranges:

$$100^{o}K \leq T \leq 7000^{o}K; \quad \Delta T = 1000^{o}K$$

and at

$$\rho/\rho_o = 10^{-5} \text{ and } 10^{1}$$

The radiation properties were initially evaluated at temperatures of 5000, 6000, and 7000°K and density ratios from 10^{-3} to 10^{1} for wavelength numbers between 1000 and 75000 cm^{-1}. Later in the study, when interest was shown in radiative heating on the rounded shoulder of the sphere-cone cases, radiative property calculations were extended to 4000°K over the same density ratio range.

3.2 THERMODYNAMIC PROPERTY ANALYSES *

For evaluation of thermodynamic properties, quantum - statistical - mechanical formulations were utilized in order to evaluate the partition function, i.e., the sum over all states, for each of the species of interest in the system. The partition function was then related directly to the ideal gas thermal functions, i.e., enthalpy, free energy, and specific heat, of the individual species.

The ideal gas thermal functions and thermodynamic properties for

* Summarized from Reference 3.26

atoms and atomic ions have been computed and are tabled in earlier reports (References 3.1 through 3.5). The calculation procedure in this instance involved the evaluation of the translational and electronic partition functions and their contribution to the thermal functions. The electronic energy level summation was extended over all energy levels up to and beyond the ionization level given in Moore (Reference 3.6). This procedure has been demonstrated (References 3.2 through 3.5) to yield essentially the same thermodynamic properties for atoms and atomic ions at temperatures below 15,000°K as predicted by using one of the more exact electronic cutoff procedures (Reference 3.7).

The ideal gas thermal functions and thermodynamic properties of diatoms and diatomic ions constitute a composite of low and high temperature calculations. The low temperature calculations were based on the rigid rotator-harmonic oscillator approximation with centrifugal stretching and vibrational anharmonicity corrections included (References 3.2 and 3.3). The high temperature calculations are based on the virial method. Here the classical second virial coefficient, in conjunction with its first and second temperature derivative, is, in turn, related to the thermal functions of the diatom through the partition function. A consistent set of thermodynamic properties is then obtained by smoothly joining the results of the low and high temperature procedures. The

polyatomic molecular thermodynamic properties are based on the rigid rotator-harmonic oscillator approximation. A comparison of the thermal functions used in these calculations with data reported in the literature has been issued recently (Reference 3.5).

In addition to the thermal functions of each species, the heat of formation is required. This data is often inferred from thermochemical, spectroscopic, or ionization potential measurements. The spectroscopic and thermochemical data, and the values of the Morse potential parameters utilized in the determination of the above properties are tabulated in the References mentioned above, as are also the sources used for obtaining those data. The heats of formation of the twenty-eight species considered in determining the equilibrium thermodynamic mixture are tabulated in Table 3.1.

The dissociation energy of a particular molecule can be obtained from the tabulated heats of formation of the species involved. Of particular interest is the dissociation energy utilized for CN. The heats of formation of CN, C, and N in Table 3.1 indicate a dissociation energy for CN of 173.5 kcal/mol or 7.52 electron volts. This value is actually based on the corresponding dissociation energy of C_2N_2. The results of many investigations (References 3.8 through 3.24) indicate some uncertainty concerning the dissociation energy of C_2N_2. The thermal properties of

Table 3.1 SPECIES HEATS OF FORMATION

Specie	(kcal/mol) Heat of Formation	(kcal/mol) Dissociation Energy
O	58.9725	
N_2	0.000	125.0
CO	- 27.202	256.0
e^-	0.000	
CO_2	- 93.9643	125.7
NO_2	8.766	71.7
N_2O	20.309	113.7
C_3	188.000	178.3
C_2N_2	73.400	145.0
CO^+	295.977	
N_2^+	359.306	
NO	21.477	150.0
NO^+	234.836	
O^-_2	10.100	
O_2	0.000	117.9
O_2^+	277.918	
C_2	195.000	145.0
CN	109.000	173.5
C	169.990	
N	112.507	
O^-	25.193	
C^+	429.370	
O^+	372.942	
N^+	447.564	
C^{++}	991.689	
O^{++}	1182.600	
N^{++}	1130.218	
C^-	141.000	

CN used in this study were based on the reported results of Knight and Rink (Reference 3.22) which indicate a dissociation energy of 145. kcal/mol for C_2N_2.

Once a set of thermodynamic properties of the individual species of interest is available over the requisite temperature range, it is then possible to evaluate the thermodynamic state of gaseous mixtures given any two state variables. The mixture equilibrium composition calculation procedure is the well-known Brinkley method (Reference 3.25) in which the mixture is considered to be composed of ideal gases without charge interaction. The system of algebraic equations expressing the free energy constraints is solved along with the atomic conservation statements by use of the Newton-Raphson technique. The independent parameters for the equilibrium composition calculation are temperature T and the logarithm to the base ten of the density ratio ρ/ρ_o, where $\rho_o = 1.29313 \times 10^{-3}$ g/cm^3. The equilibrium composition in concentrations c_i, particles of i per cubic centimeter, is found from

$$c_i = \frac{\rho x_i N_o}{M} \tag{3.1}$$

where x_i is the mol fraction of species i, M is the mixture molecular mass, and N_o is Avogadro's number.

Knowing the equilibrium composition, the thermodynamic properties

of the mixture, namely, enthalpy, entropy, etc., can then be readily determined. Further details of the calculation procedures and the resulting thermodynamic properties of the 70%N_2 - 30%CO_2 mixture are described and presented in Reference 3.26.

3.3 TRANSPORT PROPERTY ANALYSES

Transport properties of gases and gaseous mixtures were evaluated based on molecular theory (Reference 3.27). The Chapman-Enskog solution of the Boltzmann equation was used in the first approximation in order to specify the coefficients of thermal conductivity and viscosity. The intermolecular potential was represented by the modified Buckingham exponential six potential (Reference 3.27). This three-parameter potential is somewhat more flexible in reproducing experimental transport properties than the more commonly used Lennard-Jones (6-12) potential. The coefficient of viscosity is adequately described by a molecular model which does not contain internal structure. For the coefficient of thermal conductivity, the modified Eucken correction (Reference 3.28) was used to allow for contributions of internal degrees of freedom. In the mixture formulations, the Buddenberg-Wilkie approximation (Reference 3.27) was used to compute the viscosity of a gaseous mixture; Hirschfelder's equation (Reference 3.28) for the thermal conductivity of a gaseous

mixture was utilized. Given the thermodynamic properties of the planetary atmosphere, the transport property computer program was then utilized to generate the coefficients of viscosity and thermal conductivity for the gas mixture.

Transport properties for the equilibrium mixture were based only on the contributions of those species which represent more than .01 percent of the total mixture. The values of the parameters of the Buckingham exponential six potential utilized for those species are tabulated in Table 3.2. The variations of the mixture viscosity and conductivity with temperature and density are presented in Figure 3-1.

3.4 RADIATION ABSORPTION COEFFICIENT ANALYSES *

The calculation of radiative transport of energy in a hypersonic flow requires the knowledge of the radiative properties of the gas as a function of temperature and density. For cases in which local thermochemical equilibrium exists, the radiative properties of the medium can be defined by the spectral absorption coefficients.

The spectral absorption coefficients, $\kappa(\nu)$, for a gas mixture are computed by summing up at each wave number ν the contributions of the individual radiating systems in the spectral range 1000-75,000 cm^{-1}, which in the present case include molecular bands and free-bound continuum. In the calculations for molecular band systems, the model

* Summarized from Reference 3.42

Table 3.2

MODIFIED BUCKINGHAM EXPONENTIAL POTENTIAL PARAMETERS

$$\phi(r) = \frac{\epsilon}{1-\frac{6}{\alpha}}\left[\frac{6}{\alpha}\, e^{\alpha(1-r/r_m)} - \left(\frac{r_m}{r}\right)^6\right]$$

Specie	α	ϵ/k (^oK)	r_m (^oR)	Reference
N_2	15	120.2	4.046	(3.29), (3.30)
O_2	17	132	3.726	(3.30), (3.31), (3.32)
NO	14	200	3.93	(3.27)
CO	17	30.8	4.30	(3.33), (3.34 - 3.38)
CO_2	14	300	4.165	(3.29)
O	14	100	3.3	(3.30)
C_2	14	150	4.269	(3.40)
CN	15	80	4.35	(3.40)
N	13	500	2.745	(3.30)
C	15	80	3.56	(3.40)

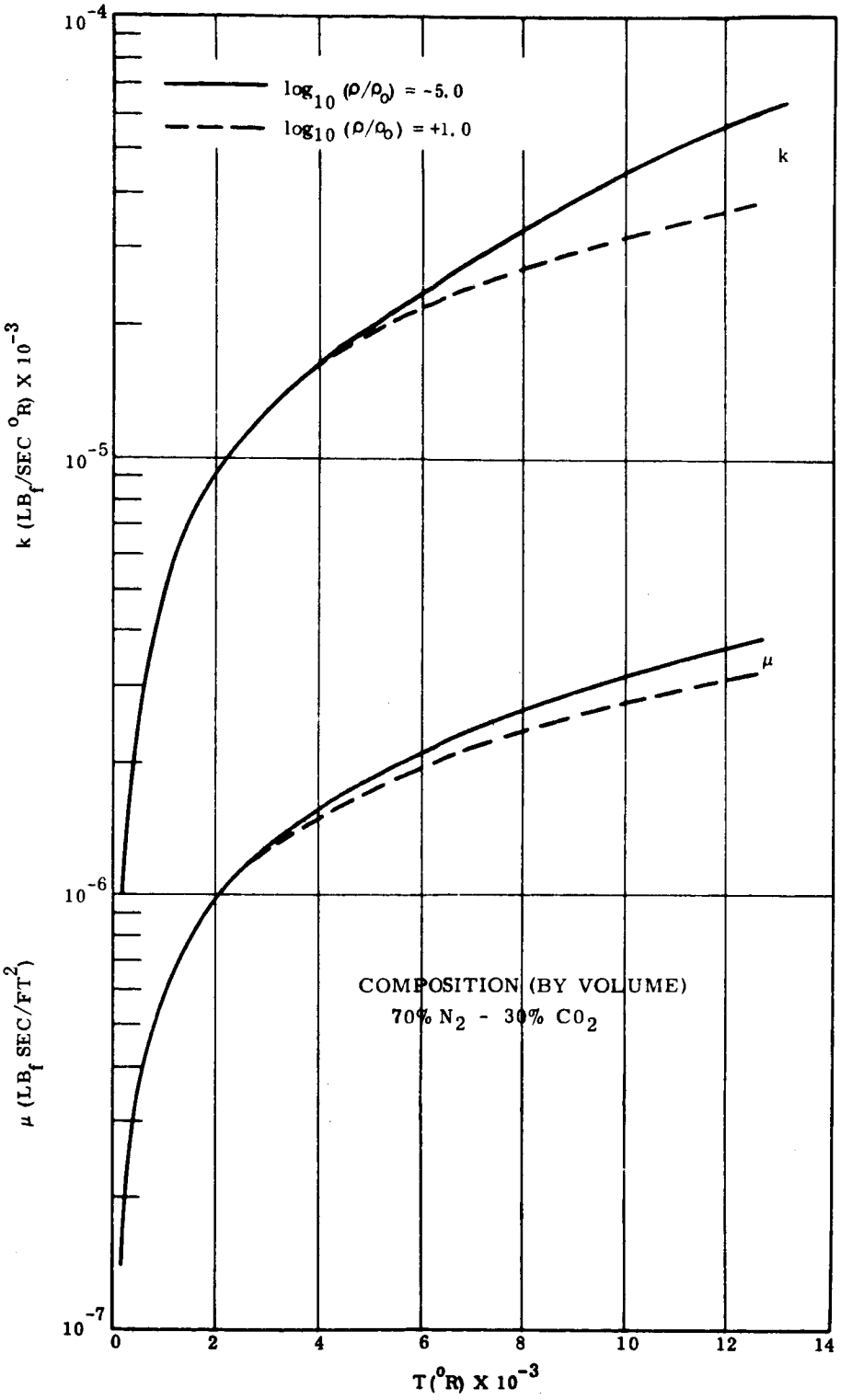

Figure 3-1. Variation of Viscosity and Thermal Conductivity With Temperature and Density

developed by Breene, (Reference 3.41), was utilized. Each band of the system is approximated by its Q-branch having an integrated strength corresponding to all branches of the band. The models also invoke Born-Oppenheimer separation of the electronic and nuclear motions in the molecule. Hence the oscillator strength of a transition is given by

$$f_{nm} = q_{v'v''} \quad \mathrm{Re}\,(\bar{r})\, f_{el}$$

where $q_{v'v''}$ is the Franck-Condon factor of the band, f_{el} is the electronic oscillator strength and Re $(\bar{r})$ is a factor allowing for variation of the electronic transition moment with internuclear separation, $\bar{r}$. This correction was introduced for oxygen and nitrogen bands but for carbon bearing species this factor was assumed to be equal to unity. The individual absorption coefficients were computed at $100 cm^{-1}$ spectral intervals. The molecular systems considered in this study and the required input constants for the calculations are presented in Table 3.3.

In addition to molecular systems, negative ion continua which result from the absorption of a photon by a negative ion and formation of a neutral atom and a free electron according to the reaction

$$O^- (2p^o) + h\nu \rightarrow O + e; \quad \nu > 11800 \text{ cm}^{-1}$$

$$C^- (4s^o) + h\nu \rightarrow O + e; \quad \nu > 9600 \text{ cm}^{-1}$$

were included. The pertinent cross-sections for these processes were taken from Branscomb et al (Reference 3.60) and Seman and Branscomb (Reference 3.61).

Table 3.3

Radiating Systems

Band System	Ref. for Spectroscopic Constants	System Absorption f-number and References	Ref. for Franck-Condon	Range of v' and v''
N_2 (1^+) $B^3\Pi_g - A^3\Sigma_u^+$	(3.43)	.014 (3.44)	(3.45)	v'' 0-13 v' 0-13
N_2 (2^+) $C^3\Pi_u - B^3\Pi_g$	(3.46)	.038 (3.47)	(3.48)	v'' 0-10 v' 0-5
N_2 (1-) $X^2\Sigma_g^+ - B^2\Sigma_u^+$	(3.43)	.040 (3.47)	(3.49)	v'' 0-5 v' 0-4
O_2 (Schuman-Runge) $X^3\Sigma_g^- - B^3\Sigma_u^-$	(3.43)	.170 (3.50)	(3.51)	v'' 0-25 v' 0-25
NO (β) $X^2\Pi_{3/2,\,1/2} - B^2\Pi_{3/2,1/2}$	(3.43)	.0015 (3.50)	(3.52)	v'' 0-19 v' 0-19
NO (γ) $A^2\Sigma^+ - X^2\Pi_{3/2,\,1/2}$	(3.43)	.0024 (3.50)	(3.49)	v'' 0-17 v' 0-6
C_2 Swan $A^3\Pi_g^- - X^3\Pi_u$	(3.43)	.034 (3.53)	(3.54)	v'' 0-5 v' 0-4
C_2 Phillips $b^1\Pi_u - 2^1\Sigma_g^+$	(3.43)	.005 (3.53)	(3.54)	v'' 0-6 v' 0-6

Table 3.3 (cont'd)

Radiating Systems

Band System	Ref. for Spectroscopic Constants	System Absorption f-number and References	Ref. for Franck-Condon	Range of v' and v''
CO Angstrom $B^1\Sigma^+ - A^1\Pi$	(3.43)	.030 (3.55)	(3.56)	v'' 0-6 v' 0-1
CO Assundi $a^1\ ^3\Sigma^+ - a\ ^3\Pi$	(3.43)	.060 (3.55)	(3.56)	v'' 0-2 v' 0-12
CO (4^+) $A^1\Pi - X^1\Sigma^+$	(3.43)	.148 (3.57)	(3.58)	v'' 0-24 v' 0-18
CO (3^+) $b^3\Sigma^+ - a\ ^3\Pi$	(3.43)	.030 (3.55)	(3.56)	v'' 0-7 v' 0-1
CN - violet $B^2\Sigma^+ - X^2\Sigma^+$	(3.43)	.027 (3.59)	(3.54)	v'' 0-3 v' 0-3
CN - red $A^2\Pi_i - X^2\Sigma^+$	(3.43)	.005 Present estimate	(3.51, 3.54)	v'' 0-8 v' 0-9

Using the number densities of individual species given by Browne, (Reference 3.26), the absorption coefficients of the mixture were generated as a function of wave number and density ratio for each temperature. These data were stored on tape for use in the Hot Gas Radiation Program. These results, as well as integrated radiation intensities in the direction normal to and total flux across the surface of an infinite isothermal parallel layer of thickness L= 1, 7, and 50 cm, are documented in Reference 3.42 for the temperature levels of 5000, 6000, and 7000°K. The values for the 4000°K level are presented in an Addendum to that reference.

Section 4

METHODS OF ANALYSES

4.1 INVISCID FLOW FIELDS

Exact numerical methods for the determination of the flow field properties about blunt bodies of revolution at zero angle of attack have been developed at GE-RSD by Dr. F. G. Gravalos. These methods provide exact solutions to the direct problem of the determination of the bow-shock shape and shock-layer properties for a specified body shape and free-stream conditions. The first stage of this work considered the flow of an ideal gas with a constant ratio of specific heats (Reference 4.1). This work was then extended to the consideration of the flow of a real gas in chemical equilibrium by the introduction of the concept of the γ^*gas (where $(\partial p/\partial \rho)_s = \gamma^* p/\rho$) (Reference 4.2).

The GE flow field solution is a numerical solution of the conservation of mass, momentum and energy laws:

$$\text{div}\ (\rho \bar{V}) = 0 \tag{4-1}$$

$$\bar{V} \cdot \text{grad}\ \bar{V} + \frac{1}{\rho}\ \text{grad}\ p = 0 \tag{4-2}$$

$$\bar{V} \cdot \text{grad}\ S = 0 \tag{4-3}$$

and of the state relations:

$$\frac{p}{\rho} = ZRT \tag{4-4}$$

$$S = S(\rho, T) \tag{4-5}$$

$$\bar{\gamma} \equiv \frac{h}{e} = \bar{\gamma}(\rho, T) \tag{4-6}$$

with

$$Z = Z(\rho, T) \text{ or} \tag{4-7}$$

$$Z = Z(\rho, S) \tag{4-8}$$

The last four of these relations are described in tabular form for the applicable composition when treated as a real gas in chemical equilibrium (Reference 4.3). The GE solution utilizes a parameter γ^*, where γ^* is defined as:

$$\gamma^* = \frac{\rho}{p}\left(\frac{\partial p}{\partial \rho}\right)_s \tag{4-9}$$

and is computed as a function of S and p, using the expression:

$$\gamma^* = \frac{a}{p} + b \tag{4-10}$$

The merit of the γ^* parameter lies in the fact that from it, it is possible to deduce the following equation as an integral of the momentum equation for isentropic flow:

$$\frac{1}{2} V^2 + \frac{a + bp}{(b-1)} = c(s) \tag{4-10a}$$

with c being constant along streamlines. Reference 4.2 gives a more detailed discussion of the γ^* parameter. The coefficients a and b are tabulated as functions of entropy and pressure (Reference 4.3).

The boundary conditions imposed on the problem are the freestream

conditions at the shock (through the Rankine-Hugoniot equations), and the condition that no mass flows through the body surface. Since the mathematical character of the governing equations is different on opposite sides of the sonic line, the solution is carried out in a different way in the subsonic, transonic and supersonic regions of the shock layer. The solution in each of these regions is briefly described below.

4.1.1 The Transonic Solution

The computation of a blunt-body flow field is started in the transonic region, which includes the sonic line and a small part of the shock layer on each side of the sonic line. A coordinate grid of streamlines and the lines normal to them is used. The solution is direct and is started by making an initial estimate of the shock shape and of the pressure distribution at the body surface. The location of a streamline a small distance from the body is then computed (as well as the values of the flow-field variables on it) to satisfy the governing equations. This process of stepping to the next streamline is repeated until a new shock wave, which satisfies the conservation of mass, is reached. The shape of this new shock wave, as well as the pressures just downstream, are compared with the shape and corresponding pressures for the initial estimate. New estimates of shock-wave shape and body-pressure distribution are based on this comparison, and on a general inspection of the results obtained in the entire transonic region. This iterative cycle is repeated until the

estimated and computed values agree to within an acceptable tolerance.

For the sphere cone configurations, the sonic line is located as shown in the sketch below. In the shoulder region, where the streamline curvature is large, the transonic solution began to degenerate near the shock where the flow is supersonic.

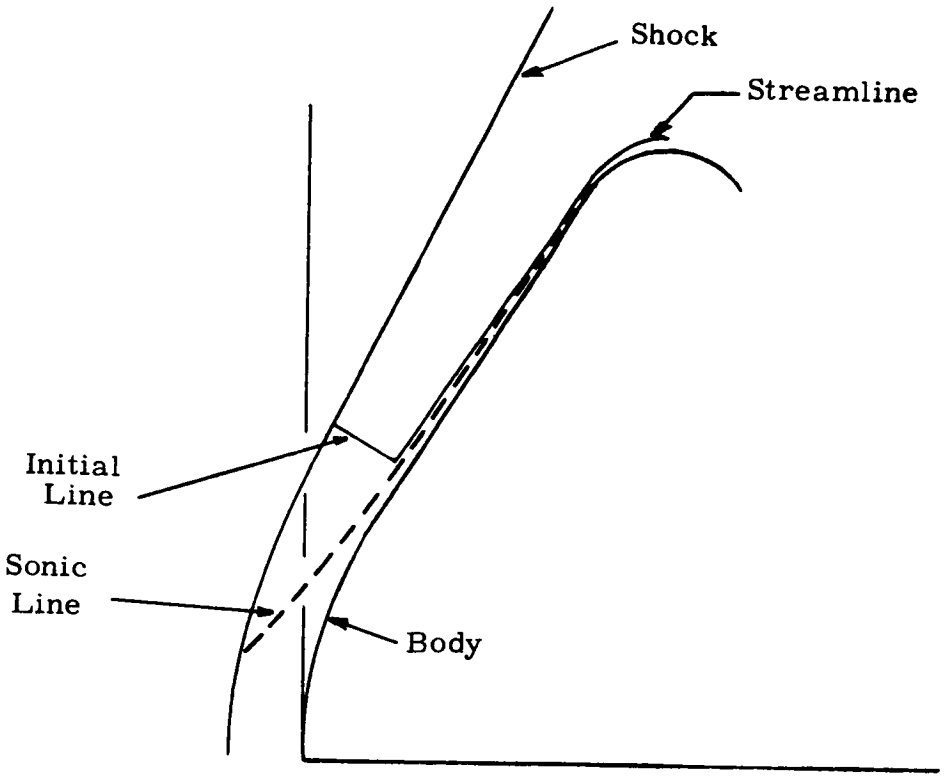

This problem was solved in the following manner:

(1) Outer Supersonic Region

The solution in the outer (supersonic) portion of the shock layer was obtained by the method of characteristics. A normal line downstream of the sphere-cone tangency point and well upstream of the

shoulder, in a region where the transonic solution is valid, was taken from the transonic solution as an initial line for the supersonic solution. A streamline lying just beyond the sonic line in the supersonic portion of the shock layer was taken from the transonic solution as the "body" surface in the supersonic solution. The resulting pressure distribution along this surface was then used as an outer boundary condition on the inner transonic solution.

(2) Inner Transonic Solution

The solution in the inner (transonic) portion of the shock layer was obtained from the transonic program described previously. The pressures along the body surface were chosen such that the resulting pressures along the supersonic streamline matched those computed in the supersonic program. These new body surface pressures then give rise to a new supersonic streamline, and the process beginning with the outer solution must be completed by iteration between the outer and inner solutions.

4.1.2 The Subsonic Solution

The subsonic solution uses a coordinate transformation which transforms the shock layer between the axis and an upper boundary into a square. The transformation between the subsonic region in the physical (x - r) plane and in the transformed (ξ - η) plane is:

$$\xi = \frac{x - f(r)}{g(r) - f(r)} \qquad \eta = \frac{r}{h(x)}$$

where

f(r) is the equation of the bow shock

g(r) is the equation of the body

h(x) is the equation of the upper boundary.

The governing equations are expressed in terms of the stream function, ψ :

$$A\psi_{\xi\xi} + 2B\psi_{\xi\eta} + C\psi_{\eta\eta} + D\psi_{\xi} + E\psi_{\eta} + F = 0 \qquad (4\text{-}11)$$

where

$$A = \xi_x^2 + \xi_r^2$$

$$B = \xi_x \eta_x + \xi_r \eta_r$$

$$C = \eta_x^2 + \eta_r^2$$

$$D = \xi_{xx} + \xi_{rr} - \frac{\xi_r}{r} - \frac{A\rho_\xi}{\rho} - \frac{B\rho_\eta}{\rho}$$

$$E = \eta_{xx} + \eta_{rr} - \frac{\eta_r}{r} - \frac{B\rho_\xi}{\rho} - \frac{C\rho_\eta}{\rho}$$

where the subscripts refer to the partial derivatives and

$$F = r^2 \rho \frac{dS}{d\psi} \frac{p(\rho, S)}{Z(\rho, S)}$$

and the energy integral:

$$h(\rho, S) + \frac{\psi_x^2 + \psi_r^2}{2(r\rho)^2} = H$$

The dimensionless entropy, S, is computed at the shock boundary and tabulated as a function of ψ. The dimensionless entropy is constant

along streamlines. The stagnation enthalpy, H, is constant through the field.

A solution is obtained by relaxation methods, in a uniform rectangular grid in the ξ-η plane. The "input" information, which is obtained from the solution in the transonic region, consists of the shock wave shape and the stream function distribution along the upper boundary of the subsonic region.

4.1.3 The Supersonic Solution

The steady-state solution in the supersonic region is carried out by the method of characteristics. Three basic directions are used: The flow direction and the directions of the Mach lines. The angles between the flow direction and the Mach lines are:

$$\mu = \pm \sin^{-1} \frac{1}{M} \tag{4-13}$$

The Mach lines are the characteristics (in the mathematical sense) of the continuity and momentum equations. Changes along these lines are defined by the equations:

$$\frac{d\theta}{dl} + \frac{\sin\mu \sin\theta}{r} \pm \frac{\cot\mu}{\rho V^2} \frac{dp}{dl} = 0 \tag{4-14}$$

where θ is the flow angle and l is the distance measured along a characteristic line. The + and - signs apply to the left and right running Mach lines respectively. Equation (4-14) is used to "step ahead" along a grid composed of the Mach lines.

4.2 VISCOUS FLOW FIELD AND AERODYNAMIC HEATING

The technical approach used in the determination of viscous flow fields and convective heating in the study involved a detailed calculation of viscous flow along the body surface. This task was accomplished through the numerical solution of the viscous boundary layer equations which provide convective heat flux results, as well as temperature and density profiles across the boundary layer, (Reference 4.12).

4.2.1 Viscous Flow Equations

The viscous equations to be solved are written in a coordinate system fixed in the body. They are: the continuity equation,

$$\text{div } \rho\overline{V} = 0; \tag{4-15}$$

the Navier-Stokes equations,

$$\overline{V} \cdot \text{grad } \overline{V} + \frac{\text{grad p}}{\rho} = \frac{1}{\rho} \text{ div } \overline{\overline{\tau}} \tag{4-16}$$

and the energy equation,

$$\rho\overline{V} \cdot \text{grad h} = \overline{V} \cdot \text{grad p} + \text{div k grad T} + \mu\Phi \tag{4-17}$$

$\overline{\overline{\tau}}$ is the viscous stress tensor, and Φ is the dissipation function. To complete the system of equations it is necessary to specify four state relations giving any four of the variables p, ρ, h, μ, k, T in terms of the remaining two. For this purpose, the tabular relations given in equations 4-6, 4-8 are used, along with the γ^* parameter and the isentropic flow relationship (Equation 4-10a). In addition, viscosity

is tabulated as a function of temperature and density.

The axisymmetric boundary layer equations which result from the application of the classical order of magnitude reduction of the above viscous equations are:

$$\frac{\partial(r\rho u)}{\partial s} + \frac{\partial(r\rho v)}{\partial n} = 0 \tag{4-18}$$

$$u\frac{\partial u}{\partial s} + v\frac{\partial u}{\partial n} + \frac{1}{\rho}\frac{\partial p}{\partial s} = \frac{1}{\rho r}\frac{\partial}{\partial n}\left\{\frac{\partial u}{\partial n}\mu r\right\} \tag{4-19}$$

$$\frac{\partial p}{\partial n} = 0 \tag{4-20}$$

$$\rho\left\{u\frac{\partial h}{\partial s} + v\frac{\partial h}{\partial n}\right\} = u\frac{\partial p}{\partial s} + \frac{\partial}{r\partial n}\left\{\frac{\mu r\partial h}{(Pr)\partial n}\right\} + \left(\frac{\partial u}{\partial n}\right)^2 \tag{4-21}$$

where the coordinate direction s is along the body surface; n is normal to the body surface.

Equation (4-20) shows that there is no pressure gradient across the boundary layer. Therefore, p is known from the inviscid flow solution. At the wall, the boundary conditions on the velocity components, in the absence of any mass transfer, are:

$$u = 0 \tag{4-22}$$

$$v = 0 \tag{4-23}$$

while the boundary condition on heat transfer is that wall temperature be a specified (tabular) function of wetted length, s:

$$T = T_w\ (s) \tag{4-24}$$

Use of the "enthalpy form" of the energy equation requires that enthalpy, rather than temperature be the boundary condition at the wall. The availability of thermodynamic state relationships (which permit calculation of enthalpy, given temperature and pressure) make it possible to specify temperature rather than enthalpy.

At the outer edge of the boundary layer, the velocity component, u, and the enthalpy, h, must approach the values obtained from the solution of the inviscid flow. The shock shape and boundary layer edge pressure distribution (in tabular form) are input to the boundary layer program. Enthalpy and velocity are obtained from them by means of a mass balance and isentropic streamline calculation. In using the mass balance technique, the point at which a particle entering the boundary layer outer edge passed through the bow shock wave is determined by calculating the radius of a stream tube (upstream of the bow shock wave) which carries a mass flow equal to the mass flow in the boundary layer at the point of interest.

4. 2. 2 Transformed Equations

The computer program used to solve equations (4-18) through (4-21) employs a method based on the work of Flügge-Lotz and Blottner (Reference 4. 5) and Blottner (Reference 4. 6). In the following description of the method, the equations are written as they apply to bodies of revolution in general. In these equations the pressure gradient terms

have been retained.

The equations are transformed with the Levy-Lees transformation in order to obtain a form amenable to numerical solution. The transformed independent variables are

$$\xi = \int_0^s \rho_w \mu_w u_e r_B^2 ds \tag{4-25}$$

$$\eta = \frac{u_e}{\sqrt{2\xi}} \int_0^\delta \rho r dn \tag{4-26}$$

and the transformed dependent variables are

$$V = \frac{2\xi}{\rho_w \mu_w u_e r^2} \left\{ f' \frac{\partial \eta}{\partial s} + \frac{r\rho v}{\sqrt{2\xi}} \right\} \tag{4-27}$$

$$f' = \frac{u}{u_e} \tag{4-28}$$

$$g = \frac{h}{h_e} \tag{4-29}$$

The prime denotes differentiation with respect to η. The subscript e is used to denote a quantity from the steady, axisymmetric, inviscid flow field. Under the transformation the equations become

$$2\xi \frac{\partial f'}{\partial \xi} + \frac{\partial V}{\partial \eta} + f' = 0 \tag{4-30}$$

$$2\xi f' \frac{\partial f'}{\partial \xi} + V \frac{\partial f'}{\partial \eta} = \beta \left\{ \frac{(du_e/ds)_c}{(du_e/ds)} \frac{\rho_e}{\rho} - f'^2 \right\} + R \frac{\partial}{\partial \eta} \left(l \frac{\partial f'}{\partial \eta} \right) + l \frac{\partial f'}{\partial \eta} \frac{\partial R}{\partial \eta} \tag{4-31}$$

$$2\xi f' \frac{\partial g}{\partial \xi} + V \frac{\partial g}{\partial \eta} = \frac{u_e^2}{h_e} \left[R\, l \left(\frac{\partial f'}{\partial \eta} \right)^2 + \beta f' \left\{ g - \frac{(du_e/ds)_c}{(du_e/ds)} \frac{\rho_e}{\rho} \right\} \right]$$

$$+ R \frac{\partial}{\partial \eta} \left(\frac{l}{(Pr)} \frac{\partial g}{\partial \eta} \right) + \frac{l}{(Pr)} \frac{\partial g}{\partial \eta} \frac{\partial R}{\partial \eta} \tag{4-32}$$

where $\ell = \frac{\rho\mu}{\rho_w \mu_w}$ and $\beta = \frac{2\xi}{u_e}\frac{du_e}{d\xi}$, $R = \left(\frac{r}{r_{body}}\right)^2$, $\left(\frac{du_e}{ds}\right)_c = -\frac{1}{\rho_e \mu_e}\frac{dp_e}{ds}$

The boundary conditions for equations (4-30), (4-31), and (4-32) are:

at the body,

$$f'(\xi, 0) = 0 \qquad (4\text{-}33a)$$

$$V(\xi, 0) = 0 \qquad (4\text{-}33b)$$

$$g(\xi, 0) = g_w(\xi) \quad \text{computed from specified wall temperature.} \qquad (4\text{-}33c)$$

at the outer edge,

$$f'(\xi, \eta_e) = 1 \qquad (4\text{-}34a)$$

$$g(\xi, \eta_e) = 1 \qquad (4\text{-}34b)$$

This set of equations is solved using an implicit finite difference scheme of the Crank-Nicolson type. The flow field is divided into a mesh as shown in the following sketch.

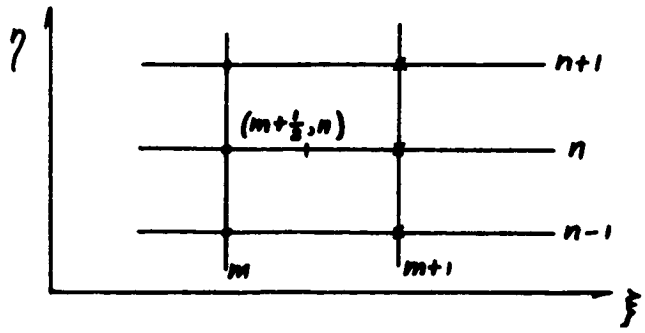

Finite Difference Grid

The dependent variables (V, f', g) are known at grid points (m) and unknown at grid points (m + 1) a small distance $\Delta\xi$ downstream. In Crank-Nicolson type finite difference schemes, the unknowns at (m + 1) are found by replacing the partial derivatives with linear difference

quotients and evaluating the partial differential equations at $(m+1/2,\ n)$. The details of replacing the derivatives with difference quotients may be found in Reference 4.6. Due to a linearization of the finite difference equations, the continuity equation is not coupled to the momentum and energy equations, and thus it may be integrated after the others have been solved. The remaining difference equations can be written in the following matrix form.

$$A_n W_{n+1} + B_n W_n + C_n W_{n-1} = D_n; n = 1,\ 2,\ \ldots\ n_\delta$$

where A_n, B_n, C_n are 2 x 2 matrices consisting of known coefficients; the W_n's are column vectors containing the unknowns (f', g); D_n is a column vector containing the non-homogeneous terms in the difference equations; and n_δ is the number of mesh points taken across the boundary layer. Since an implicit finite difference scheme has been employed, the whole set of $2n_\delta$ difference equations is coupled and must be solved simultaneously. The set of equations is, however, of a special form (tridiagonal) for which a very efficient method of solution is available (Reference 4.6).

In order to complete the specification of the problem, the following quantities are required: step sizes and initial profiles.

For equations of boundary layer type the Crank-Nicolson finite difference scheme has been shown to be inherently stable; thus in theory,

there are no known stability restrictions on the step sizes $\Delta\xi$, $\Delta\eta$. The optimum step size can therefore be selected purely on the basis of an accuracy-solution time tradeoff.*

As a result of the parabolic nature of the boundary layer equations, initial profiles for V, f', and g are required at $\xi = 0$ ($s = 0$). At $\xi = 0$ the continuity equation becomes

$$\frac{\partial V}{\partial \eta} + f' = 0 \tag{4-35}$$

or, upon solving

$$V = -f = -\int_0^{\eta} f' d\eta \tag{4-36}$$

Calculations were started with the initial velocity and temperature profiles given below

$$f' = \frac{u}{u_e} = 2\frac{\eta}{\eta_e} - 2\left(\frac{\eta}{\eta_e}\right)^3 + \left(\frac{\eta}{\eta_e}\right)^4 \tag{4-37}$$

and

$$T/T_e = 1 + \left(\frac{T_w}{T_e} - 1\right)\left[1 - 2\frac{\eta}{\eta_e} + 2\left(\frac{\eta}{\eta_e}\right)^3 - \left(\frac{\eta}{\eta_e}\right)^4\right] \tag{4-38}$$

The transformed normal velocity (V) starting profile was computed from equations (4-37) and (4-36). Equations (4-37) and (4-38) were obtained from Reference 4.7, and were originally derived for use in the Karman - Pohlhausen technique. In applying them, it was assumed that

* In practice, step size does have an effect on stability, so that care and experience must be used in making the selection.

at the stagnation point the thickness of the thermal boundary layer is equal to the thickness of the velocity boundary layer.

4. 2. 3 Real Gas Properties

The boundary layer program requires thermodynamic and transport properties of the dissociated and ionized gases for the specified Mars atmospheric model (30% CO_2 - 70% N_2 by volume). The thermodynamic properties were tabulated as indicated in Equations (4-6), (4-8) and (4-10), and supplied as input to the boundary layer computer program. Viscosity was tabulated as a function of temperature and density.

An investigation was carried out to determine what values of Prandtl number could be expected in the boundary layer. Nowhere does it vary significantly from a value of 0. 72. A constant value of Prandtl number ($P_r = 0.72$) was therefore used in the boundary layer calculations.

4. 2. 4 Convective Heating

The local convective heating is readily available from the viscous boundary layer solution as

$$q_c = -\frac{\mu}{Pr}\left(\frac{\partial h}{\partial y}\right)_w = -\frac{\rho_w \mu_w u_e h_e r_b}{Pr_w \sqrt{2\xi}}\left(\frac{\partial g}{\partial \eta}\right)_w \qquad (4\text{-}39)$$

4.3 RADIATION HEATING

The basic techniques used in calculating the hot gas radiative heating to a vehicle have been incorporated into a computer program known as the Hot Gas Radiation (HGR) Computer Program. This program was used in calculating the equilibrium gas radiative heating from the flow fields to the sphere cap and sphere cone configurations.

4.3.1 Description of Hot Gas Radiation Program

The Hot Gas Radiation (HGR) Computer Program is an improved version of the program which was used in making the radiative heating calculations for the Project Fire flights (Reference 2.24). This program calculates the radiative fluxes:

1. incident upon the vehicle surface ($\dot{q}_{HG_{incident}}$)

and 2. absorbed by the vehicle surface ($\dot{q}_{HG_{absorbed}}$)

The equation for radiant intensity (I) is of the form (References 4.8 and 4.9):

$$I_\nu(s) = e^{-\int_{s_o}^{s} \mathcal{K}_\nu \, ds} \int_{s_o}^{s} \mathcal{K}_\nu B_\nu \, e^{\int_{s_o}^{s} K_\nu \, ds} \, ds + I_o \, e^{-\int_{s_o}^{s} \mathcal{K}_\nu ds} \qquad (4\text{-}40)$$

where I = radiant intensity

s = path length

$\mathcal{K}$ = absorption coefficient of gas

B = Planck's black-body function

Subscripts:

ν = wave number = reciprocal of wavelength

o = initial value

Use of this equation in the determination of radiative heating to the vehicle surface results in the following solution for finite increments as shown in References 4.10 and 4.11:

$$\dot{q}_{HG_\nu}{}_{incident} = \sum_{\theta}\sum_{\phi} \epsilon_\nu B_\nu \frac{\sin^2\theta}{2}\Bigg|_{\theta}^{\theta+\Delta\theta} \Delta\phi \prod_i \tau_{\nu_i} \tag{4-41}$$

$$\epsilon_\nu = 1 - e^{-K_\nu \Delta r} \tag{4-42}$$

$$B_\nu = \frac{2hc^2}{\lambda^5}\left[e^{\frac{hc}{kT\lambda}} - 1\right]^{-1} \tag{4-43}$$

$$\tau_{\nu_i} = e^{-K_{\nu_i} \Delta r} \tag{4-44}$$

$$\dot{q}_{HG_\nu}{}_{absorbed} = \alpha_\nu \dot{q}_{HG_\nu}{}_{incident} \tag{4-45}$$

$$\dot{q}_{HG}{}_{incident} = \sum_\nu \dot{q}_{HG_\nu}{}_{incident} \Delta\nu \tag{4-46}$$

$$\dot{q}_{HG}{}_{absorbed} = \sum_\nu \dot{q}_{HG_\nu}{}_{absorbed} \tag{4-47}$$

where c = velocity of light

h = Planck's constant

k = Boltzmann constant

α = absorptance of surface

ϵ = emissivity of gas volume increment

T = temperature of gas

θ = angle from body normal (spherical coordinates)

ϕ = angle around body normal (spherical coordination)

λ = wave length

$\prod$ = product operator

i = i^{th} increment

τ = transmittance of gas for radiant energy

$\sum$ = summation operator

r = increment of radial distance (spherical coordinates)

$\dot{q}_{HG}$ = heat flux due to hot gas radiation

A hemispherical geometry is used as follows:

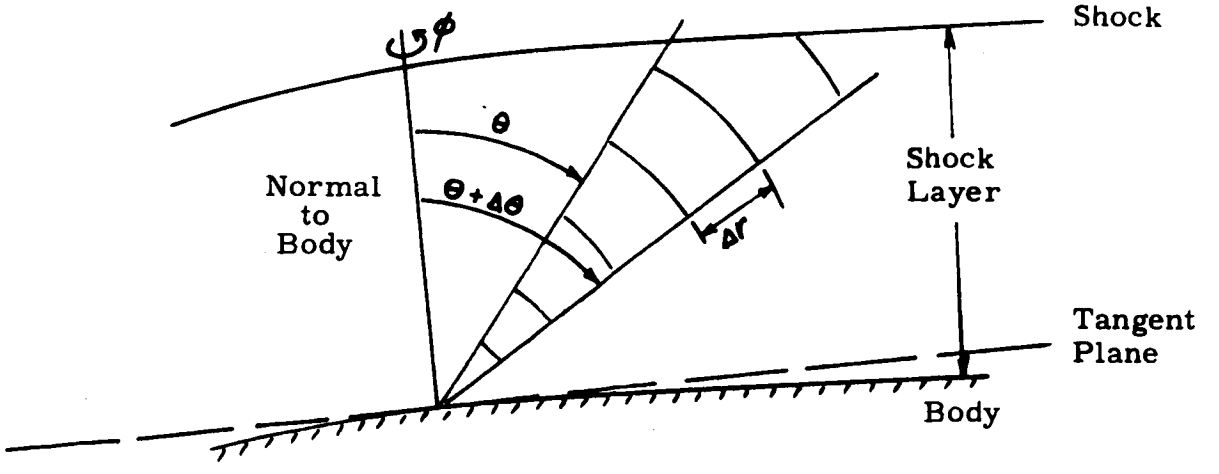

For calculating equilibrium radiation, the inputs to the HGR Program include gas temperature (T) and density (ρ) as a function of position in the flow-field. The radiation absorption coefficients (K_ν) for a particular atmosphere (e.g., 30% CO_2 - 70% N_2) are stored on tape as part of the program input. These are functions of wave number (ν), temperature (T), and density (ρ) for the particular equilibrium atmosphere. Several features of the HGR Program which help to make it both versatile and accurate are:*

1. Self-absorption is included. The absorption of part of the radiative flux by intervening gas volumes (i.e., volumes between the emitting volume and the vehicle surface) is included. This approach is applicable to non-optically thin gases.

2. Emissivity of an incremental volume of the hot gas is calculated according to the equation $\epsilon_\nu = 1 - e^{-K_\nu \Delta r}$ and consequently is applicable for non-optically thin gases. (Note: Many methods of calculating gas radiation use a relationship for emissivity of the form $\epsilon_\nu = K_\nu \Delta r$ which is a portion of the series expansion

$$\epsilon_\nu = 1 - e^{-K_\nu \Delta r} = 1 - \left[1 - K_\nu \Delta r + \frac{(-K_\nu \Delta r)^2}{2!} \quad \ldots.\right] \approx K_\nu \Delta r$$

* The features described in Items 1, 2 and 4 were used in the present study.

and is good only for optically thin gases, where $\frac{(-K_\nu \Delta r)^2}{2!}$ may be neglected with respect to $(K_\nu \Delta r)$.)

3. Absorptance (α) of the vehicle surface may be specified as a function of wavelength (λ), (i.e., $\alpha = \alpha(\lambda)$ is input to the program). This is necessary for obtaining an accurate value for absorbed radiative flux, since the contributions to the radiative flux from different regions of the spectrum vary markedly in magnitude and must, therefore, be "weighted" with their appropriate values of surface absorptance.

4. Radiative fluxes from any incremental gas volume or any pencil of rays may be calculated and printed out. In this way it may be determined which portions of the gas layer contribute most significantly to the total incident (or absorbed) radiation.

5. Absorption and emission of radiation from the ablation gases in the boundary layer of the vehicle can be included in the calculations. This effect is taken into account by considering the boundary layer as a separate flow field

which is surrounded by the hot gas shock layer consisting of the planetary gases. (See previous sketch showing the geometry involved.) Separate absorption coefficients for the species in the ablation gases are input for this boundary layer flow field.

4.3.2 Description of Calculations

Calculations for the equilibrium radiation from each of the flow fields were made with the use of the Hot Gas Radiation Program as outlined in the previous paragraphs.

The equilibrium absorption coefficients for the 30% CO_2 - 70% N_2 atmosphere as given in Reference 3.42 were input to the program on magnetic tape. These absorption coefficients were for temperatures of $4000^{o}K \leq T \leq 7000^{o}K$, density ratios of $10^{-3} \leq \rho/\rho_o \leq 10^{1}$, and wave numbers of 1000 cm.$^{-1} \leq \nu \leq$ 75000 cm.$^{-1}$. The absorption coefficients were averaged over bands of wave numbers in order to arrive at absorption coefficients corresponding to 41 wave numbers which then were treated on a spectral basis in the program. These wave numbers were every 2000 cm.$^{-1}$ up to 69000 cm.$^{-1}$ and every 1000 cm.$^{-1}$ thereafter up to and including 75000 cm.$^{-1}$.

The vehicle (body) absorptance was taken as unity since its

value as a function of wavelength was not specified. This, then, gives the same value for absorbed radiative heat flux as for incident radiative heat flux.

Due to symmetry at the stagnation point it was necessary to consider only one fan (ϕ angle) of radiating gas. At body points other than stagnation, it was necessary to consider the fans between $\phi = 0^{o}$ and $\phi = 180^{o}$ due to symmetry between the $0^{o} \leq \phi \leq 180^{o}$ volume and the $180^{o} \leq \phi \leq 360^{o}$ volume (i. e., the $0^{o} \leq \phi \leq 90^{o}$ volume is not symmetrical with the $90^{o} \leq \phi \leq 180^{o}$ volume). Therefore, at body points other than stagnation, 7 fans were considered. Each fan (including the stagnation fan) was subdivided into 6 pencils (θ angle) of rays, where $0^{o} \leq \theta \leq 90^{o}$. Each pencil of rays was further subdivided into a number of volume elements depending upon the angle θ (i. e., the volume element size was selected by dividing the shock standoff distance into a number of equal parts - this number ranged from 6 to 10 for the cases considered). Thus, in some instances ($75^{o} \leq \theta \leq 90^{o}$) the number of volume increments considered in a single pencil was 100. For a typical case, the total number of volume increments considered was 720. This method of treating the radiant energy allows temperature and density variations to occur within the flow field and also is an accurate way of including self-absorption for a flow field which is of non-uniform temperature and

density.

As an estimate of an upper bound for the radiant flux at the stagnation point, calculations were made for a thin layer of the flow field at the stagnation point. A path length (shock stand-off distance) of 10^{-7} cm. was used for the ballistic range flow fields and a path length of 10^{-2} cm. was used for the hyperbolic entry flow fields. In this way, the effect of self-absorption was ignored and the optically-thin radiative heating was approximated as:

$$\dot{q}_R(\Delta_s)_{O.T.} = 2\pi\Delta_s \sum_\nu K_\nu B_\nu \Delta\nu$$

$$\approx 2\pi \frac{\Delta_s}{L} \sum_\nu (1-e^{-K_\nu L}) B_\nu \Delta\nu = \frac{\Delta_s}{L} \times \dot{q}_R(L)$$

since $(1-e^{-K_\nu L}) \approx K_\nu L$ for $K_\nu L$ sufficiently small.

where $\dot{q}_R(\Delta_s)_{O.T.}$ = optically-thin radiative heating based on Δ_s path length

$\dot{q}_R(L)$ = radiative heating based on L path length

Δ_s = shock stand-off distance at stagnation point

It should be pointed out that some accuracy is sacrificed in this approximation. In the future, a modification to the HGR Program will be made to allow calculation of the optically-thin radiative heating (upper limit to true radiative heating) in the exact manner.

As an additional comparison, hand calculations were performed

at the stagnation point for the radiative heating based on several path lengths (shock stand-off distances). These were based upon the heat flux curves as determined in Reference 3.42 for a uniform plane of gas. These were compared with computer calculations from the HGR Program as determined for various path lengths. Stagnation conditions considered were those for the ballistic range and hyperbolic entry cases.

Section 5

DISCUSSION OF RESULTS

This section presents the results of the computations for all the cases of the present study described in Section 1. The computational methods used were discussed in Section 4. The inviscid flow results are discussed first, followed by the convective and radiative heating results. Since one objective of the ballistic range study was to simulate the hyperbolic entry flight condition, the results for each configuration are presented such that comparisons between the two free stream conditions can easily be made.

5.1 INVISCID FLOW FIELD PROPERTIES

The temperature, density and Mach number distributions in the shock layer for the sphere cone configurations are shown in Figure 5-1 through 5-3, respectively. The results of these figures, and the following three figures for the sphere cap, are to be interpreted in the following manner. Consider for example Figure 5-1, depicting sphere cone shock layer temperature distributions. In this figure the body and shock geometry for each flight condition are shown along with temperatures at several selected points through the shock layer. The temperatures written to the left of the shock wave in each case refer to the point

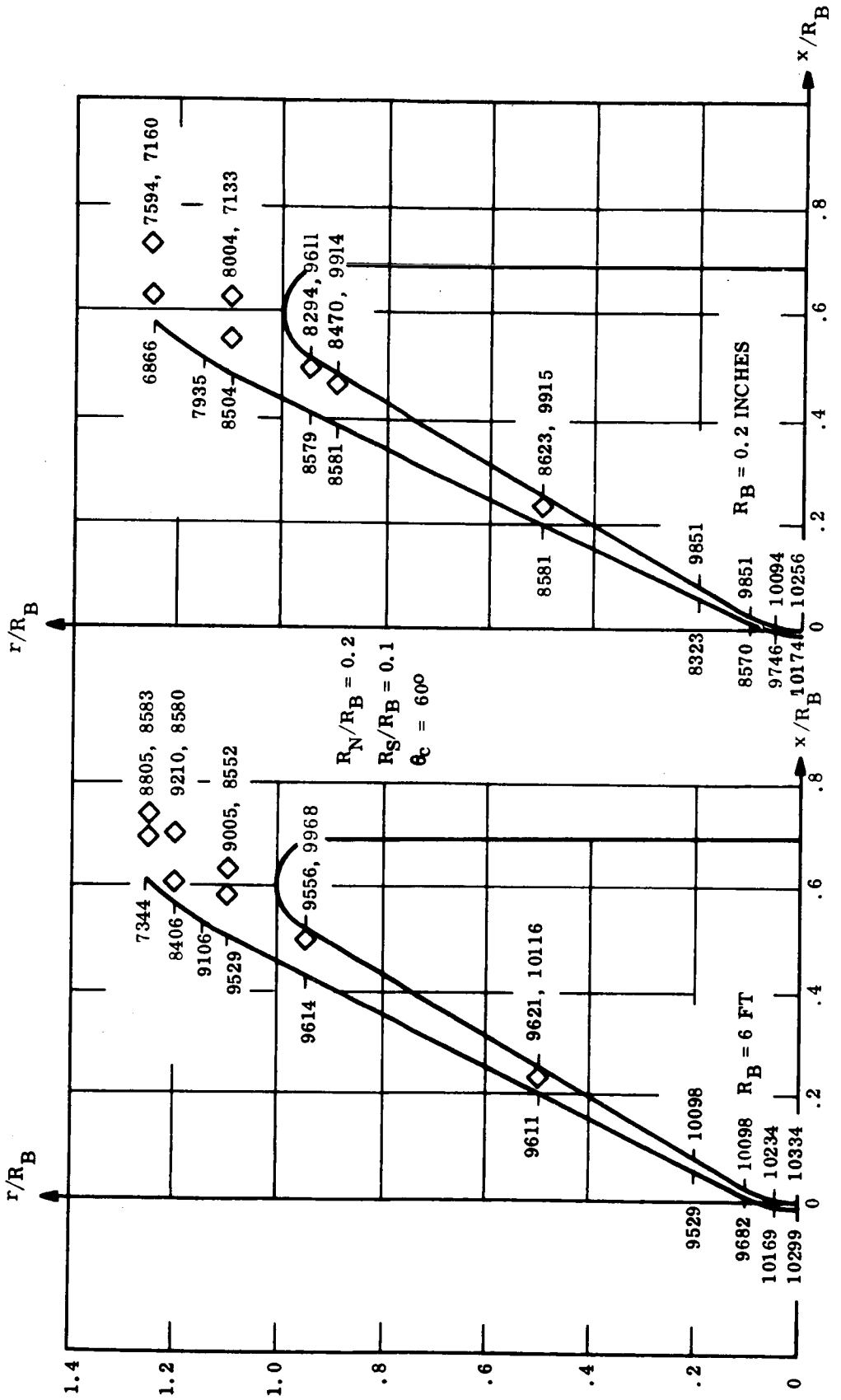

Figure 5-1. Sphere-Cone Inviscid Shock Layer Temperature Distributions

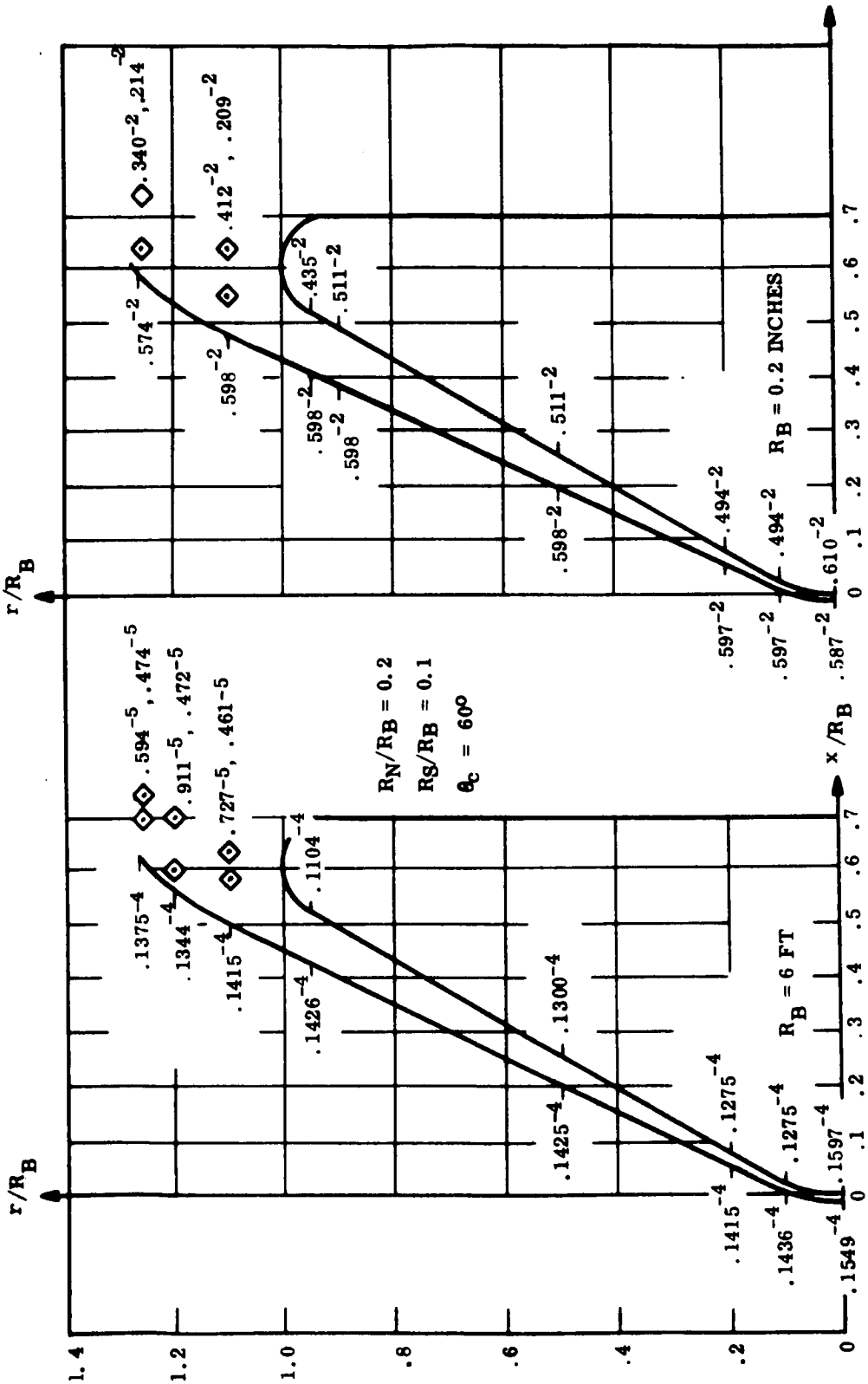

Figure 5-2. Sphere-Cone Inviscid Shock Layer Density Distributions

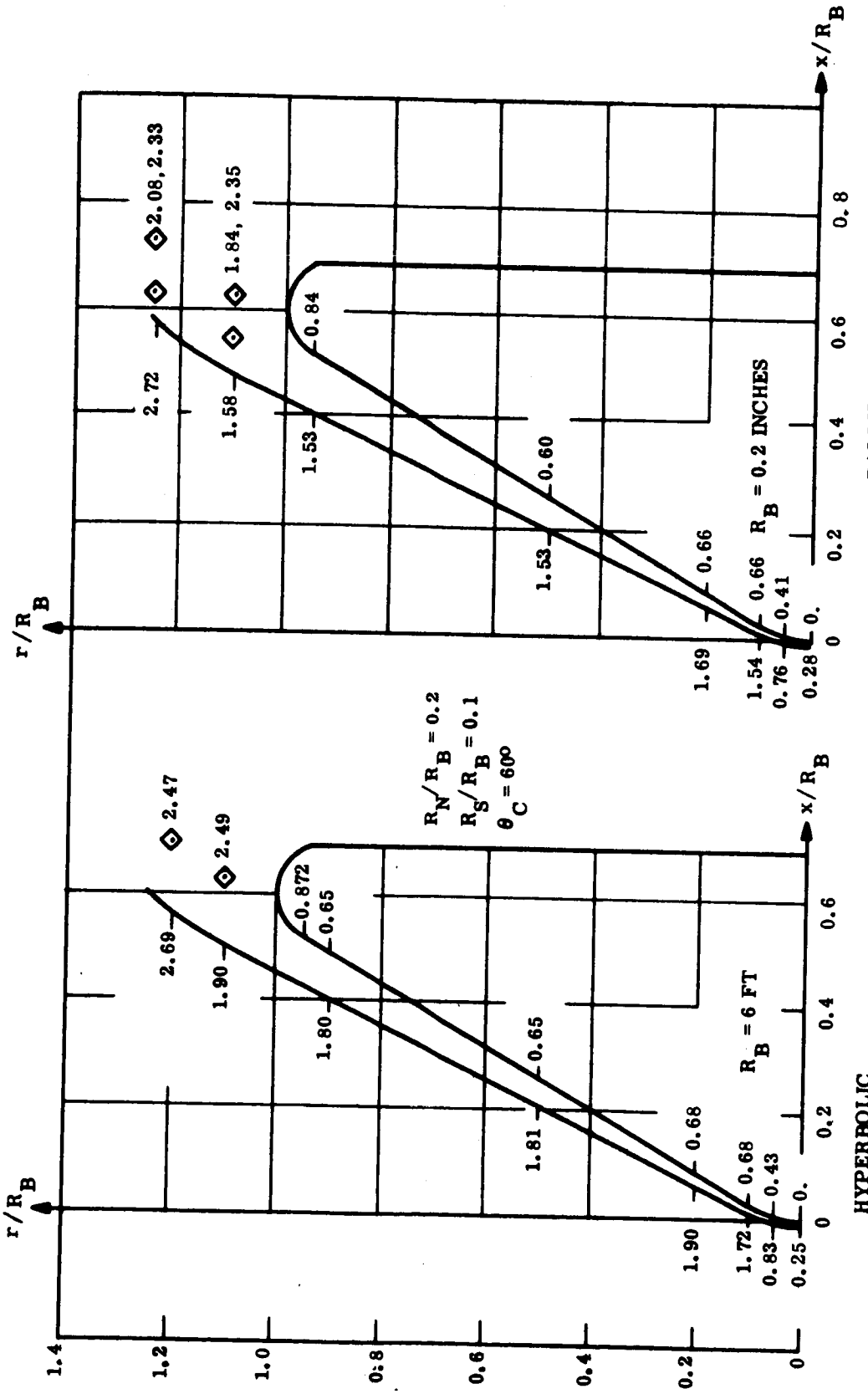

Figure 5-3. Sphere-Cone Inviscid Shock Layer Mach Number Distributions

immediately downstream of the shock wave at the radius ratio at which the temperature is written.

Thus, for example, the temperature downstream of the bow shock in the hyperbolic case at $r/R_B = 0.5$ (where $x/R_B = .21$) is $9611^{\circ}R$. Points not on the boundary of the shock layer (field points) are designated by the symbol ◇. The temperatures associated with these field points, as designated from left to right at a given radius ratio, are to be read from left to right from the numbers located to the right of the shock layer. Finally, the last temperature given to the right at any radius ratio is the inviscid temperature at the body surface; if the body surface exists at that radius ratio, and otherwise is the last field point to the right. From Figure 5-1 it is seen that the temperatures in the stagnation region of the sphere-cones for the two flight conditions are comparable, as was intended. However, in the conical region of the shock layer, the temperatures in the hyperbolic case are approximately $1000^{\circ}R$ greater than those in the ballistic range case, except very near the body surface where an inviscid entropy layer exists. The general shapes of the shock waves are nearly identical, with the shock angle in the conical region of the ballistic range case (65°) being slightly greater than that of the hyperbolic entry (64°).

The density downstream of the shock wave initially decreases with increasing radius in the hyperbolic case, whereas the opposite trend exists for the ballistic range case (Figure 5-2).

As seen from Figure 5-3, the Mach numbers for the hyperbolic entry condition are slightly greater than those for the ballistic range condition. The sonic line in both cases lies very near the body surface, along the conical portion of the body, giving rise to a subsonic inner layer and a supersonic outer layer in the conical shock layer region. The flow subsequently goes entirely supersonic immediately downstream of the cone-shoulder tangency point.

In Figure 5-4, for the sphere cap shock layer temperature distributions, it is seen that the temperature downstream of the shock wave in the ballistic case decreases with increasing radius more rapidly than that in the hyperbolic case, until finally at $r/D_B = 0.5$, they differ by approximately $1000^{\circ}R$. The maximum difference occurs at $r/D_B = .55$, where the temperature downstream of the bow shock in the hyperbolic case is greater than that in the ballistic by about $1300^{\circ}R$. The density downstream of the shock decreases with increasing radius in the hyperbolic case until $r/D_B = .6$, and then begins to increase (Figure 5-5). In the ballistic case, however, the density downstream of the shock increases until $r/R_B = .5$, and then decreases with increasing radius.

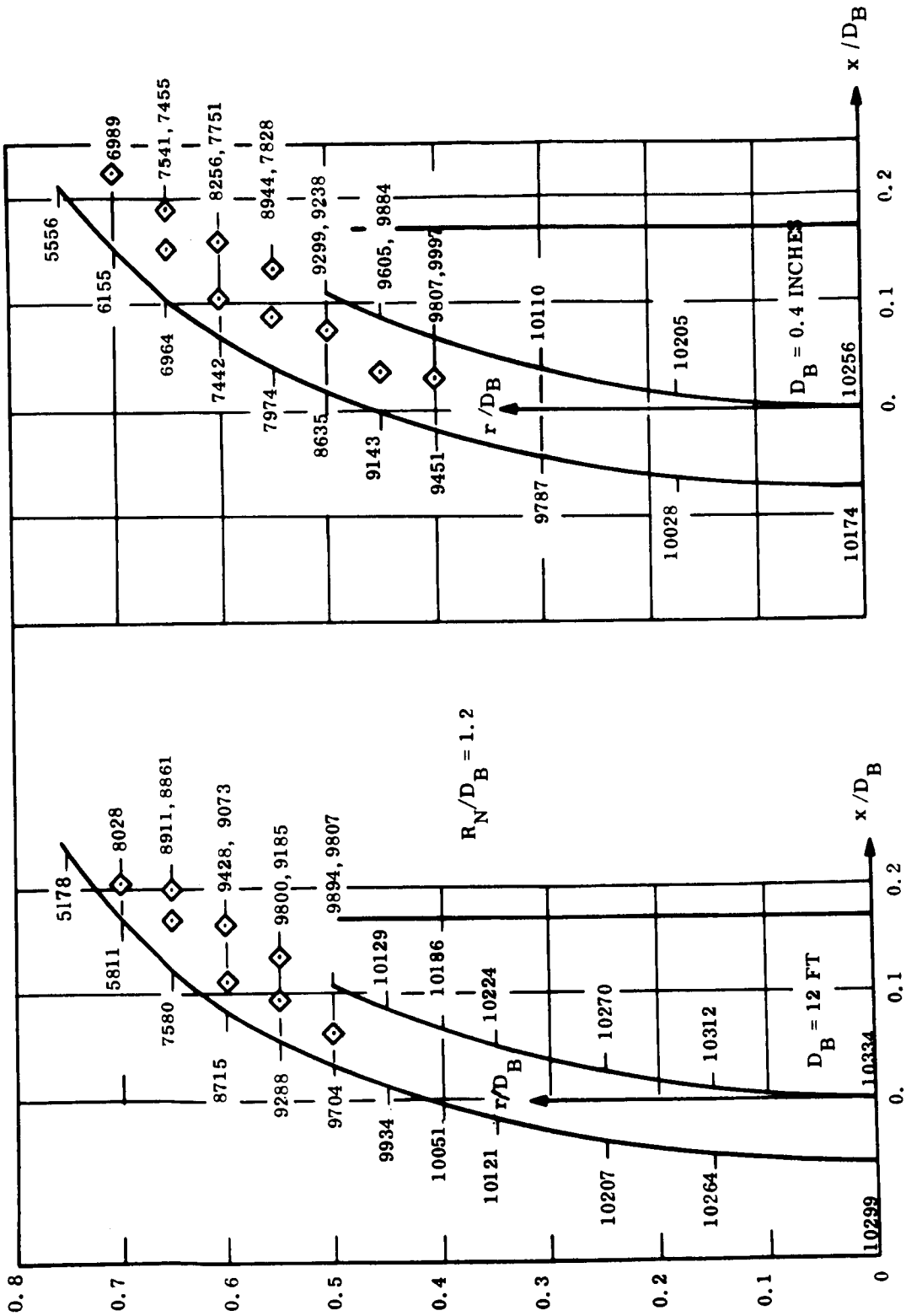

Figure 5-4. Sphere-Cap Inviscid Shock Layer Temperature Distributions

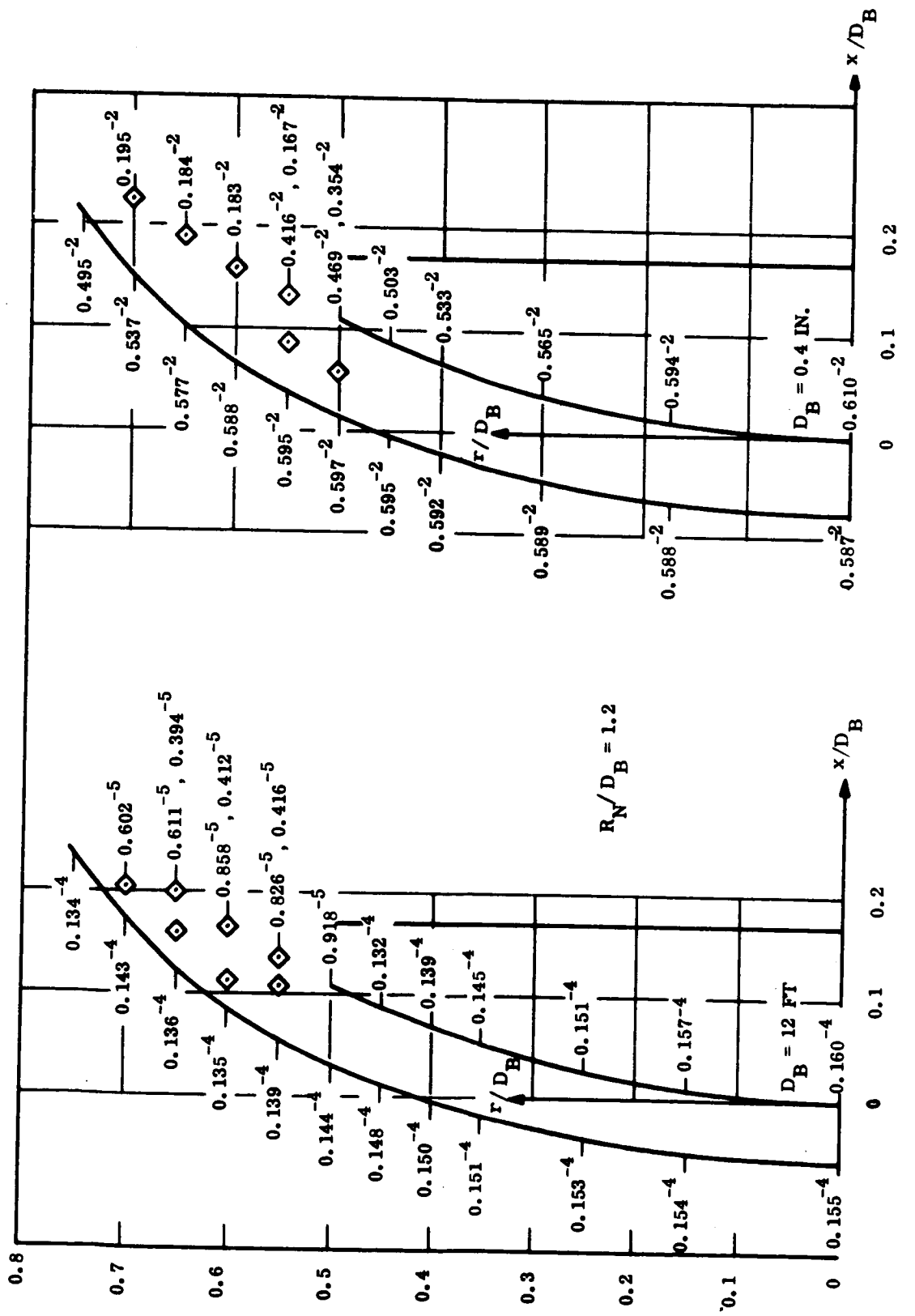

Figure 5-5. Sphere-Cap Inviscid Shock Layer Density Distributions

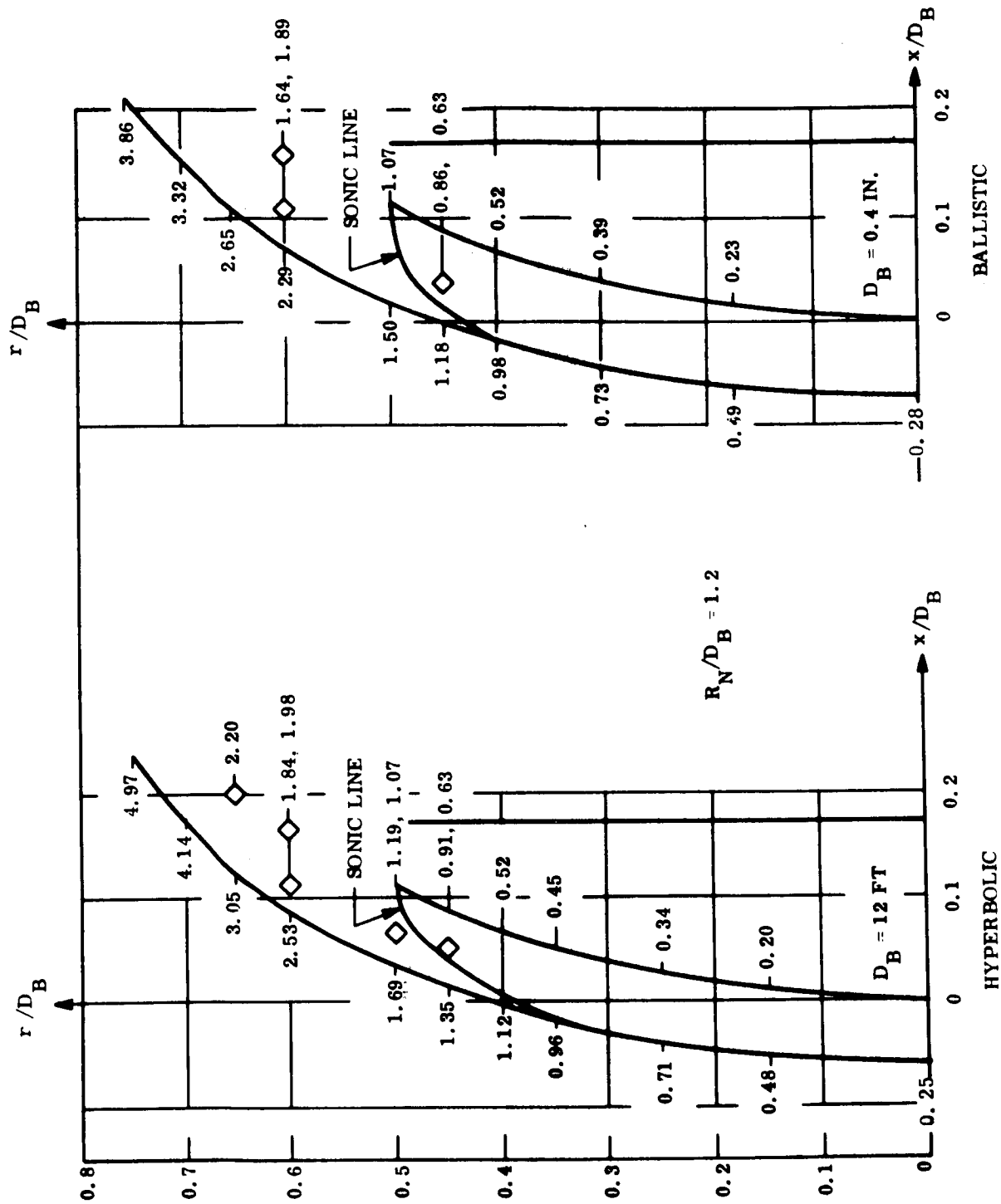

Figure 5-6. Sphere-Cap Inviscid Shock Layer Mach Number Distributions

The Mach number distributions are shown in Figure 5-6 where it is seen that the Mach numbers are generally higher in the hyperbolic case than in the ballistic case.

The sphere cone and sphere cap surface pressure distributions are shown in Figures 5-7 and 5-8. For the sphere cone, the pressure along the cone surface is asymptotic to the pointed cone pressure. An over-expansion and subsequent recompression of the flow after it has turned past the sphere cone tangency point is evident in Figure 5-7. This result is consistent with the general trends exhibited in Figure 5-9 for sphere cones in air, computed by the methods of Reference 4.2. A direct correlation can not be drawn since the flow is everywhere supersonic downstream of the sphere cone tangency point for the air results; however, the general trends should still exist, as the cone angle is increased, since the majority of the shock layer is supersonic at and downstream of the sphere cone tangency point.

The inviscid forebody drag for the sphere cone configurations was found to be 1.45 and 1.46, respectively, for the hyperbolic entry and ballistic range cases. For the sphere cap the inviscid drags are 1.67 and 1.64 for the hyperbolic and ballistic cases. These results are seen to compare favorably with the experimental data of Reference 5.1, shown in Figure 5-10. The theoretical drag data shown in Figure 5-10 for the sharp shouldered sphere-cone was obtained from the pressure distributions shown in Figure 5-7, under the assumption that no pressure drop would occur on the cone forebody near the base.

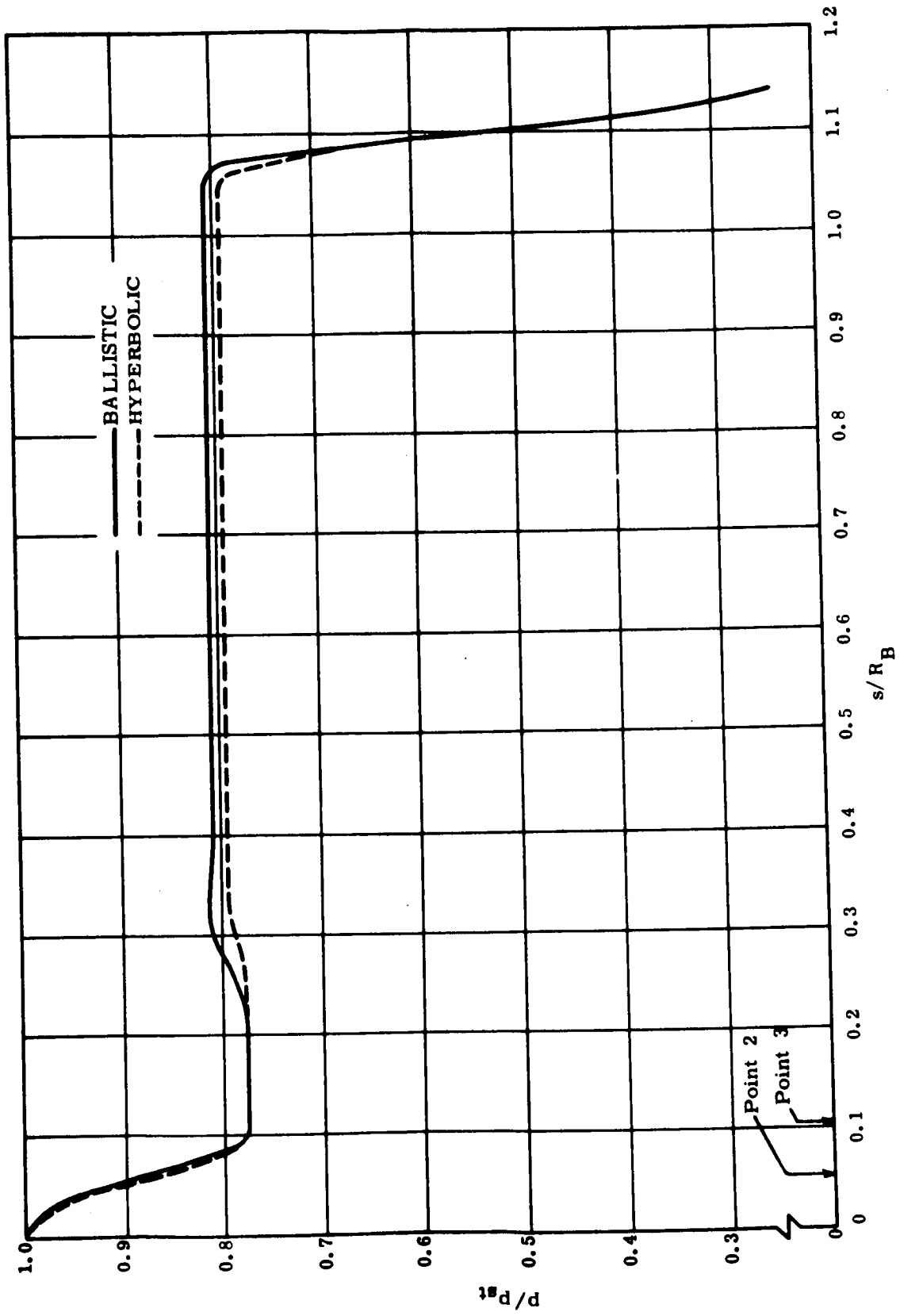

Figure 5-7. Sphere-Cone Surface Pressure Distribution

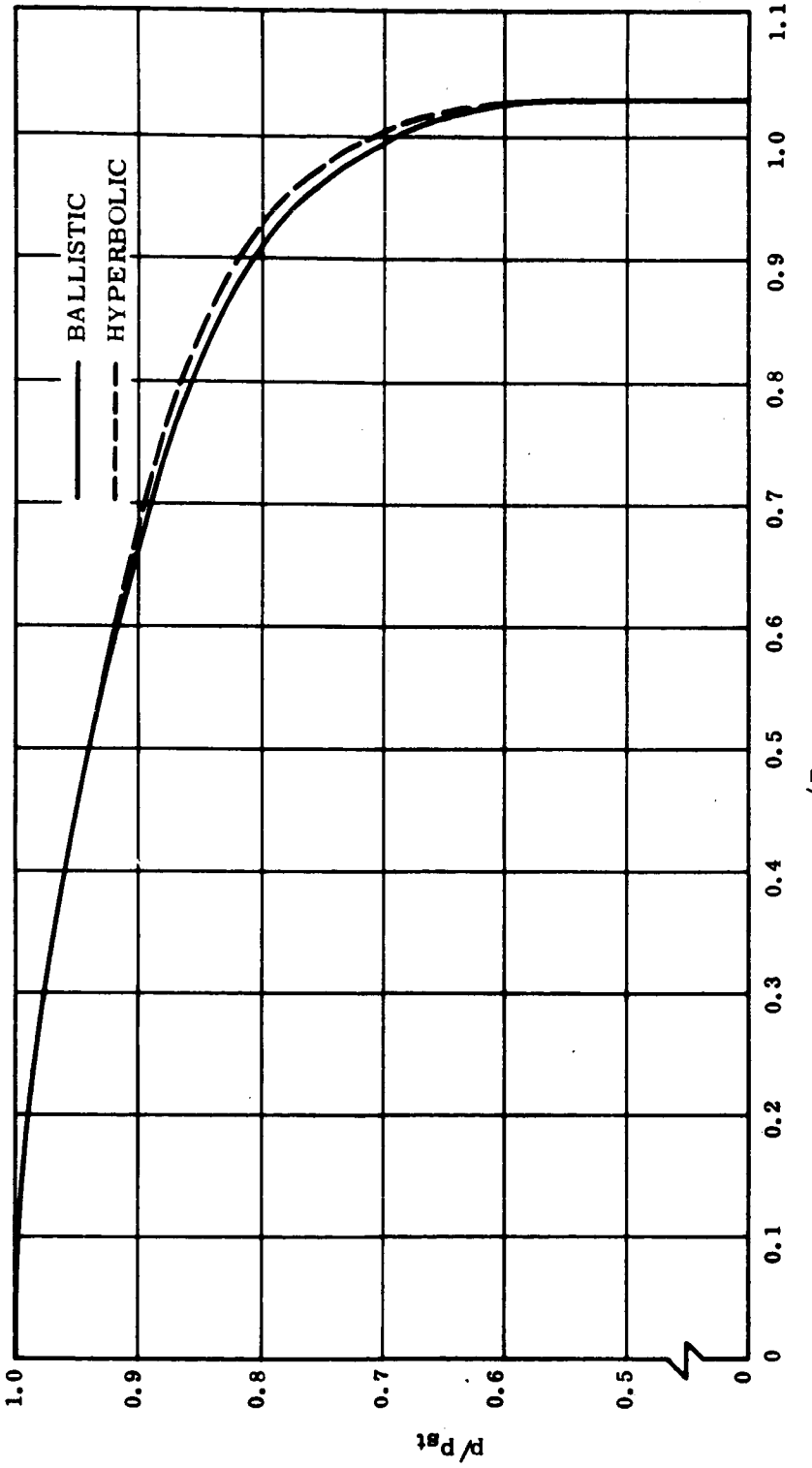

Figure 5-8. Sphere-Cap Surface Pressure Distribution

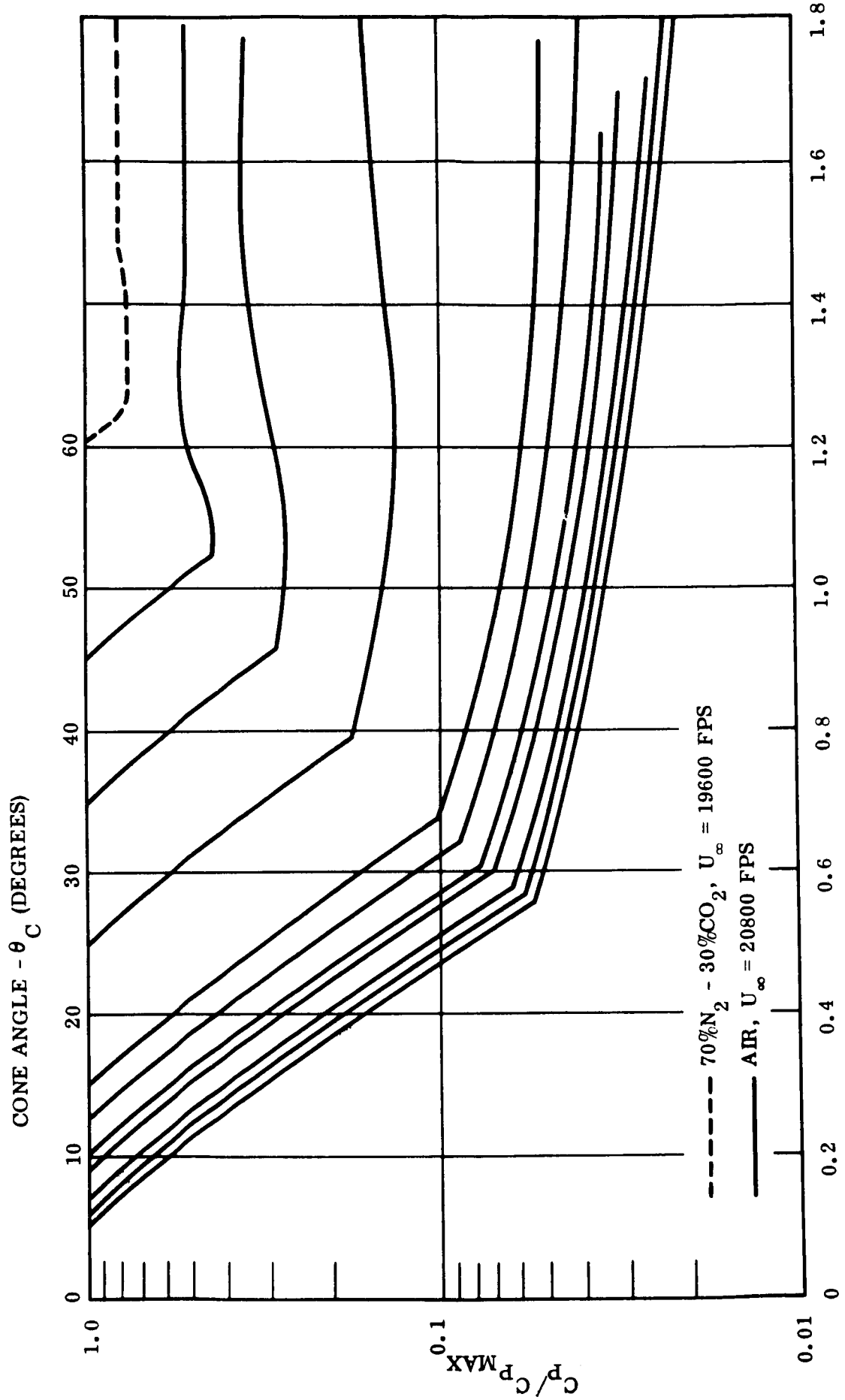

Figure 5-9. Sphere-Cone Surface Pressure Distributions

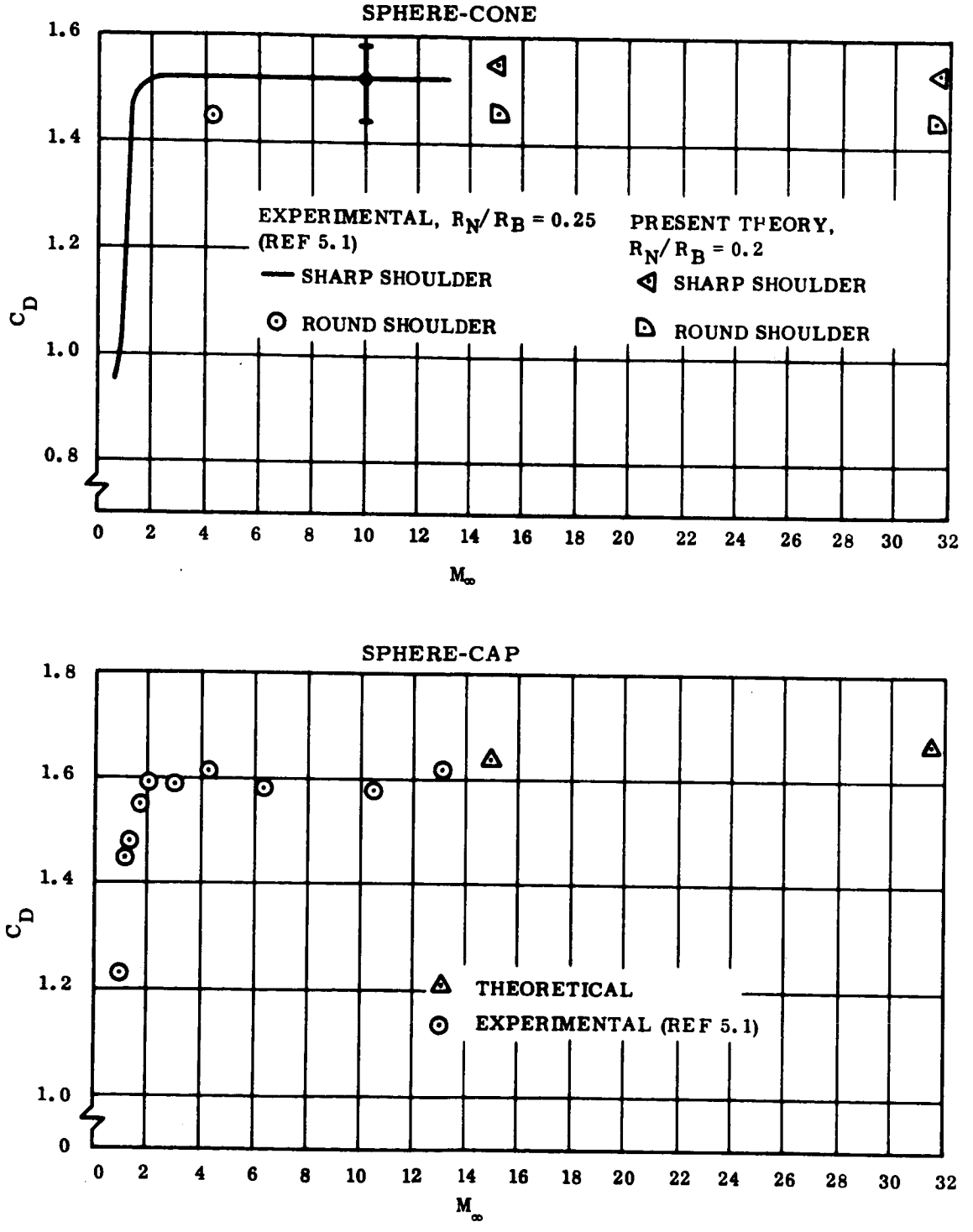

Figure 5-10. Drag Coefficient

The normalized stagnation point shock detachment distances are compared in Table 5-1 with estimates obtained from several theoretical results and correlations available in the literature. The results of the present study are

Table 5-1

Normalized Shock Detachment Distance Δ/R_N.

		Sphere Cone		Sphere Cap	
Method	Reference	Hyperbolic	Ballistic	Hyperbolic	Ballistic
Present Study		.0500	.0675	.0500	.0638
Ridyard and Storer	5.2	.0488	.0656	.0488	.0656
Li and Geiger	5.3	.0542	.0607	.0542	.0607
Hayes and Probstein	5.4	.0478	.0607	.0478	.0607
Serbin	5.5	.0460	.0621	.0460	.0621
Linnell	5.6	.0508	.0656	.0508	.0656

within three percent of the results of Ridyard and Storer. During the study, the question arose as to whether the shock detachment distance for such large angle cones is still dominated by the nose bluntness rather than the base diameter. The results of a separate GE-RSD study of the shock detachment distances of pointed cones with detached shocks led to the curve of Figure 5.11. This curve indicates, as a function of free stream Mach number, the cone angle above which the base dominates the determination of the shock detachment distance for sphere - cones with $R_N/R_B = .20$. Thus, for the free stream Mach numbers of

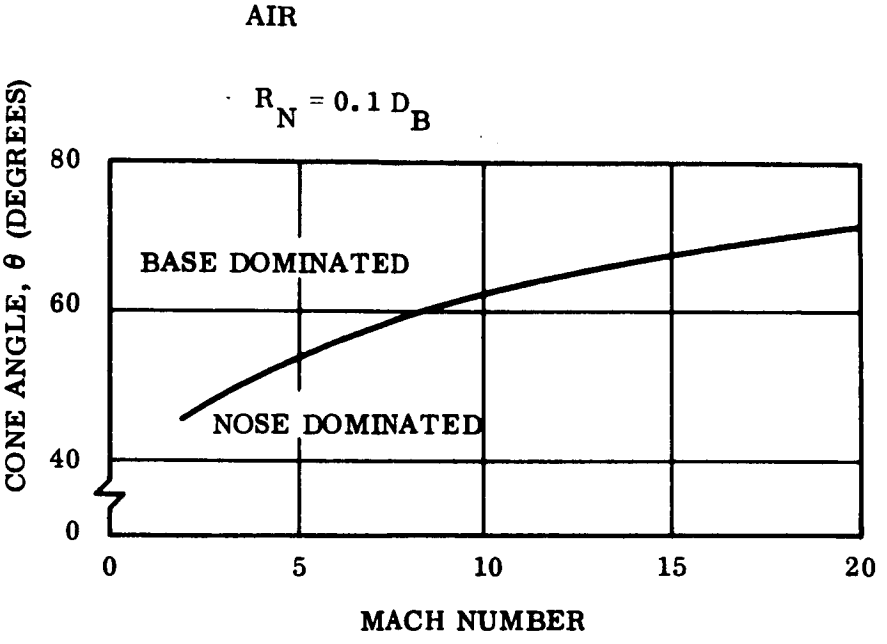

Figure 5-11. Shock Standoff Characteristics

this study, the agreement shown in Table 5-1 would be expected.

The stagnation point velocity gradients, which are much more sensitive to the details of the flow than is the shock detachment distance, are compared with several estimates in Table 5-2.

Table 5-2

Normalized Stagnation Point Velocity Gradient, $R_N(du_e/ds)/u_\infty$

		Sphere Cone		Sphere Cap	
Method	Reference	Hyperbolic	Ballistic	Hyperbolic	Ballistic
Present Study		.419	.414	.381	.453
Li and Geiger	5.3	.353	.403	.353	.403
Linnell	5.6	.348	.401	.348	.401
Hearne, Chin, Lefferdo	5.8	.378	.430	.378	.430
Newtonian		.348	.398	.348	.398

The results of the present study are within approximately fourteen percent of the commonly-used Newtonian estimates.

5.2 VISCOUS FLOW AND CONVECTIVE HEATING

Results of the non-similar boundary layer calculations appear in Figures 5-12 through 5-28, and in Tables 5-3 and 5-4. Convective heat transfer distributions are plotted in Figures 5-12 and 5-13. An initial decrease in heat transfer with distance from the stagnation point occurs on the sphere cones, followed by a relatively constant $\dot{q}$ over the conic section and finally another decrease at the shoulder. The inflection in the curves does not coincide exactly with the sphere cone juncture, because of the relatively complicated variation of the various flow properties at the edge of the boundary layer. These variations are present because of the combination of pressure gradient and entropy gradient present in the flow field. They are brought into the boundary layer calculation through the mass balance method of tracing back along the streamlines from the boundary layer edge to the bow shock wave. In the case of the sphere cap models, heat transfer remains relatively constant from stagnation point to the shoulder. Boundary layer calculations were not continued beyond the sharp corner at the shoulder.

Values of the stagnation point convective heat transfer computed in the present study are compared in Table 5-3 with corresponding values obtained from correlations of numerical solutions for stagnation point

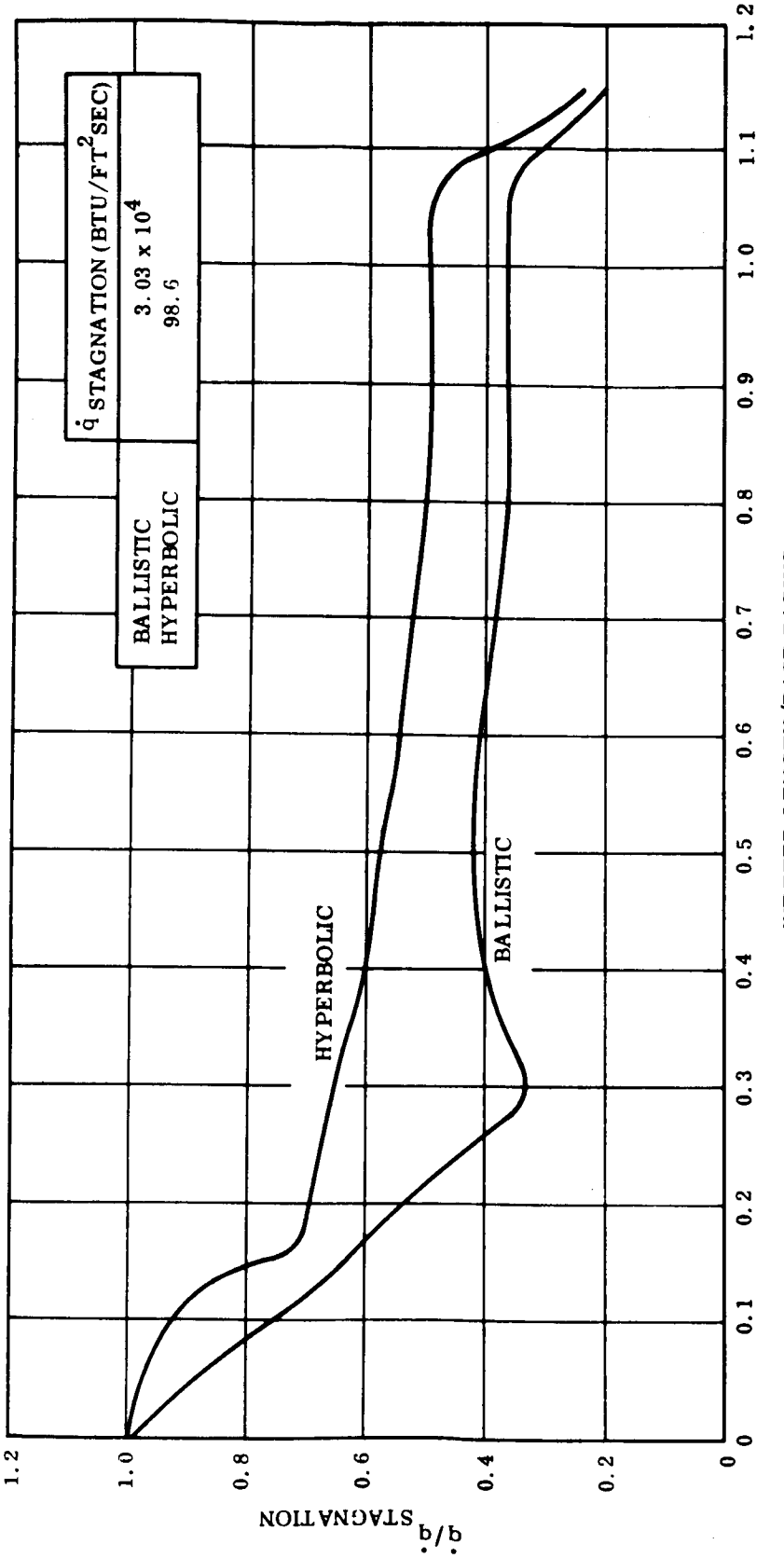

Figure 5-12. Sphere-Cone Convective Heat Transfer Distribution

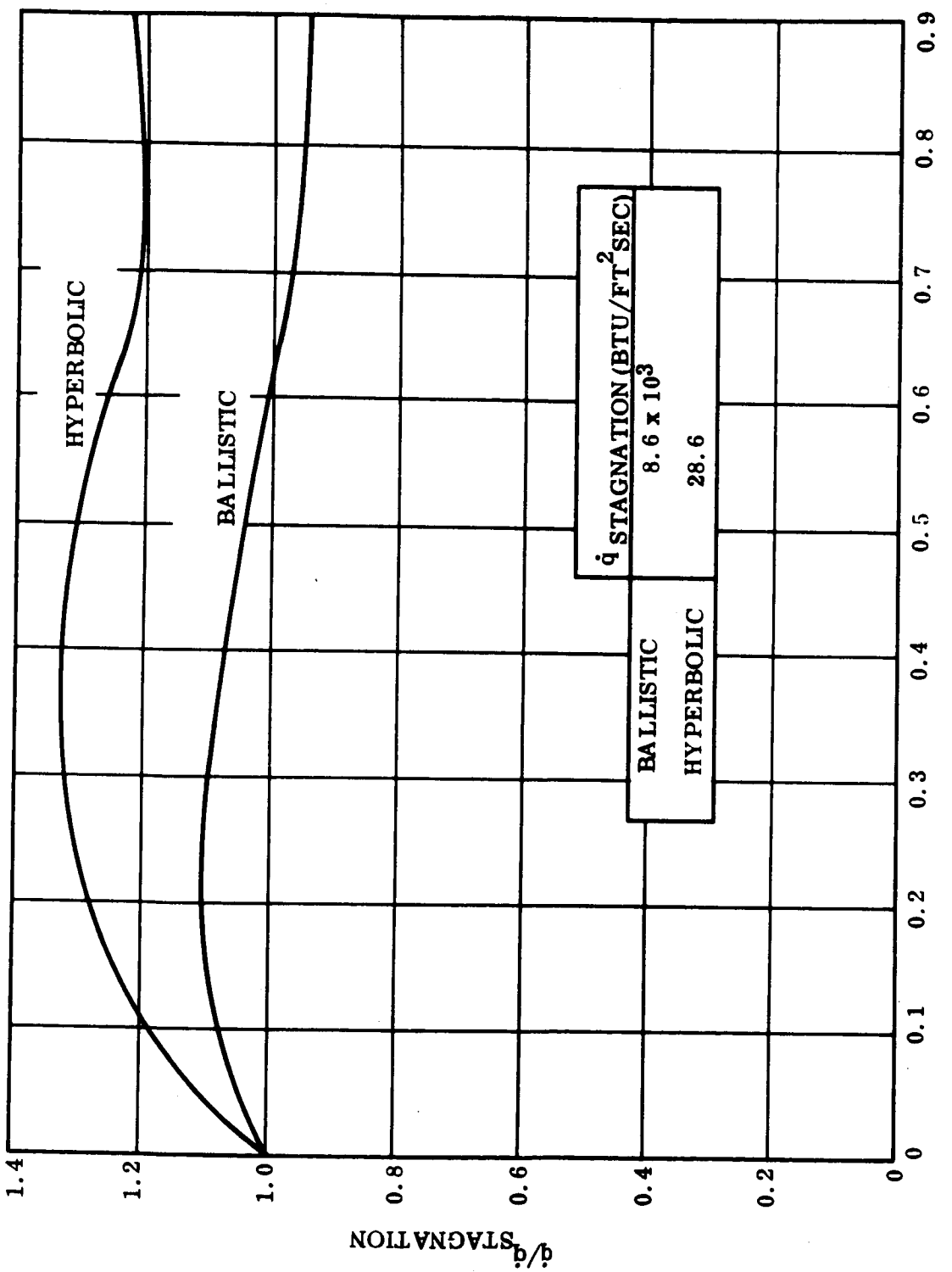

Figure 5-13. Sphere-Cap Convective Heat Transfer Distribution

Table 5-3

STAGNATION POINT CONVECTIVE HEAT TRANSFER

Btu/ft.^{2} sec.

		Sphere-Cone		Sphere-Cap	
Method	Reference	Hyperbolic	Ballistic	Hyperbolic	Ballistic
Present Study		0.99×10^2	3.03×10^4	2.86×10^1	8.60×10^3
Fay and Riddell	5.9	1.38×10^2	2.96×10^4	3.99×10^1	8.51×10^3
Hoshizaki	5.10	1.20×10^2	2.68×10^4	3.47×10^1	7.72×10^3
Scala and Gilbert	5.11	1.21×10^2	2.66×10^4	3.47×10^1	7.69×10^3

The correlation expressions are given below:

Fay and Riddell: (assuming unity Lewis number)

$$\dot{q}_{st} = \frac{.76}{(Pr)^{.6}} \left[\frac{\rho_w \mu_w}{\rho_{st} \mu_{st}}\right]^{0.1} \left[\rho_{st} \mu_{st} \frac{du_e}{ds}\right]^{1/2} (h_{st} - h_w)$$

Hoshizaki:

$$\dot{q}_{st} = 2.6(10^4) \left[\frac{R_N}{u_\infty} \left(\frac{du_e}{ds}\right)\right]^{1/2} \sqrt{\frac{\rho_\infty}{R_N}} \left(\frac{u_\infty}{10^4}\right)^{3.19} \left(1 - \frac{h_w}{h_{st}}\right)$$

ρ_∞ = slugs/ft^3 $\qquad$ u_∞ = ft/sec

Scala and Gilbert:

$$\dot{q}_{st} = \frac{\left[12. + .866 (\bar{M}_\infty)\right] (10^{-3}) (h_{st} - h_w)}{\sqrt{R_N / p_{st}}}$$

p_{st} = atmospheres

h = Btu/lb.

$\bar{M}_\infty$ = mean molecular weight

heat transfer in equilibrium air.* In the ballistic case agreement is within 13% (sphere-cone as well as sphere-cap model). The effect of chemical composition appears to be greater in the hyperbolic case, where the correlations give values from 21% to 40% higher than the non-similar boundary layer solution.

Boundary layer thickness, displacement thickness and momentum thickness are plotted against wetted length in Figures 5-14 through 5-19. All values have been non-dimensionalized by the base radius in order to facilitate comparison between the hyperbolic and ballistic cases. All the thicknesses show some undulations caused by the variations in edge properties.

The ratios of stagnation point boundary layer thickness to shock detachment distance are shown in Table 5-4.

Table 5-4

Stagnation Point Boundary Layer Thickness/Shock Detachment Thickness

Body	Flight Condition	Δ/R_N	δ/R_N	δ/Δ
Sphere-Cone	Hyp. Entry	.0500	.00925	.185
Sphere-Cap	Hyp. Entry	.0500	.00296	.059
Sphere-Cone	Ball. Range	.0675	.01000	.148
Sphere-Cap	Ball. Range	.0638	.00050	.008

The ratios for the sphere-cap configurations are much less than unity; those for the sphere-cone cases are somewhat larger than those for the sphere-caps, but still much less than unity. For those cases,

* Except the Scala and Gilbert correlation which accounts for heat transfer in other atmospheres (through M_∞).

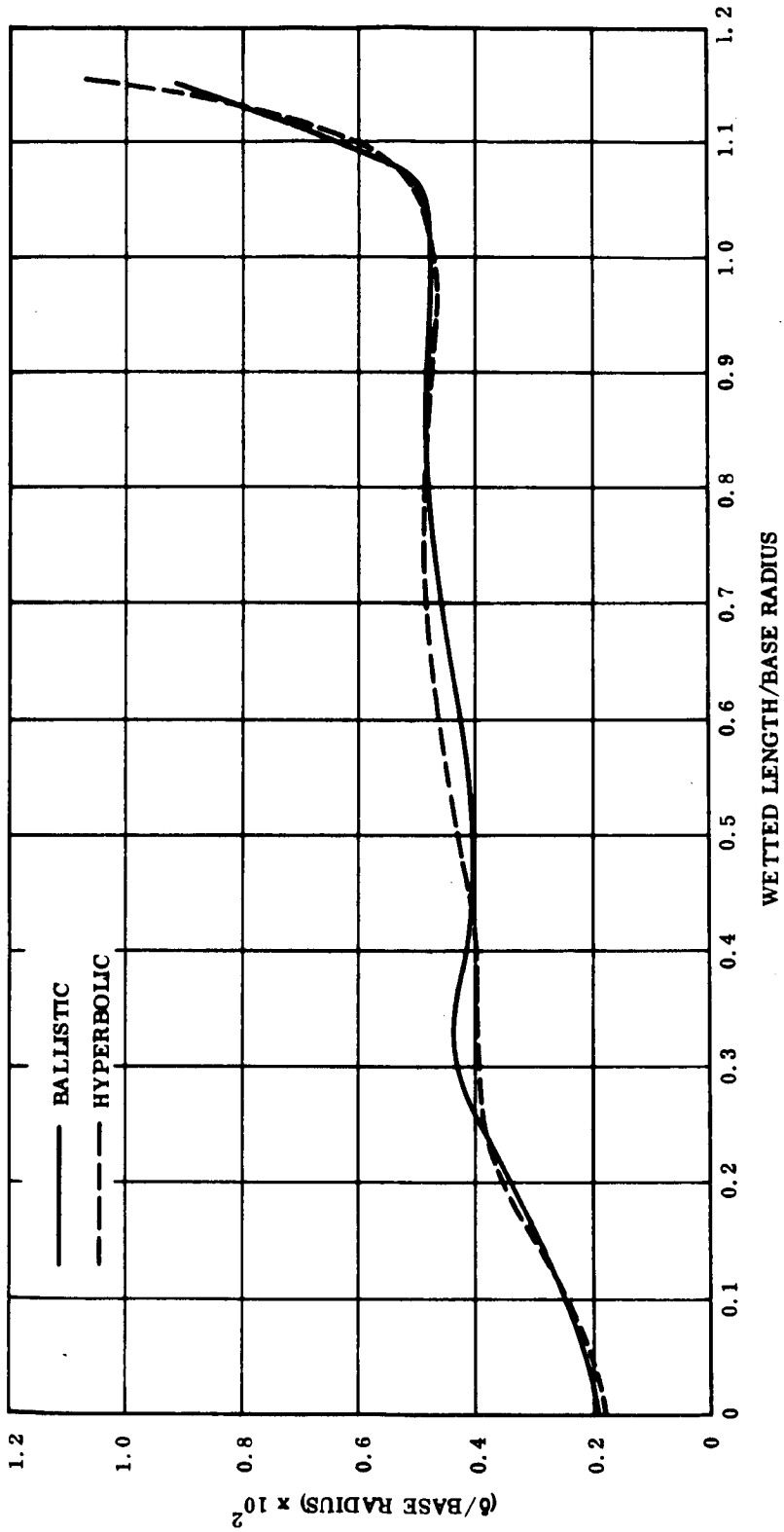

Figure 5-14. Sphere-Cone Boundary Layer Thickness

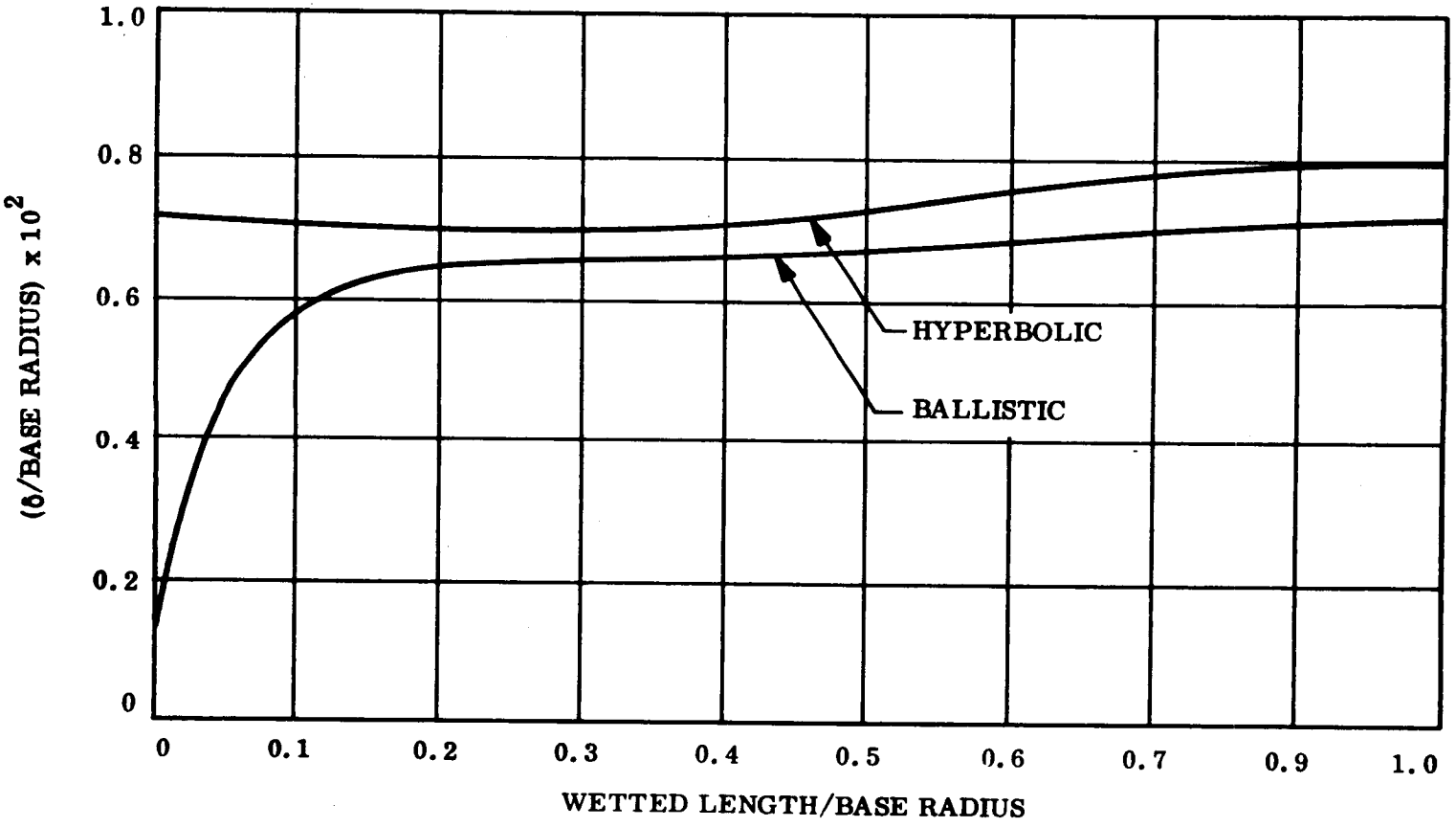

Figure 5-15. Sphere-Cap Boundary Layer Thickness

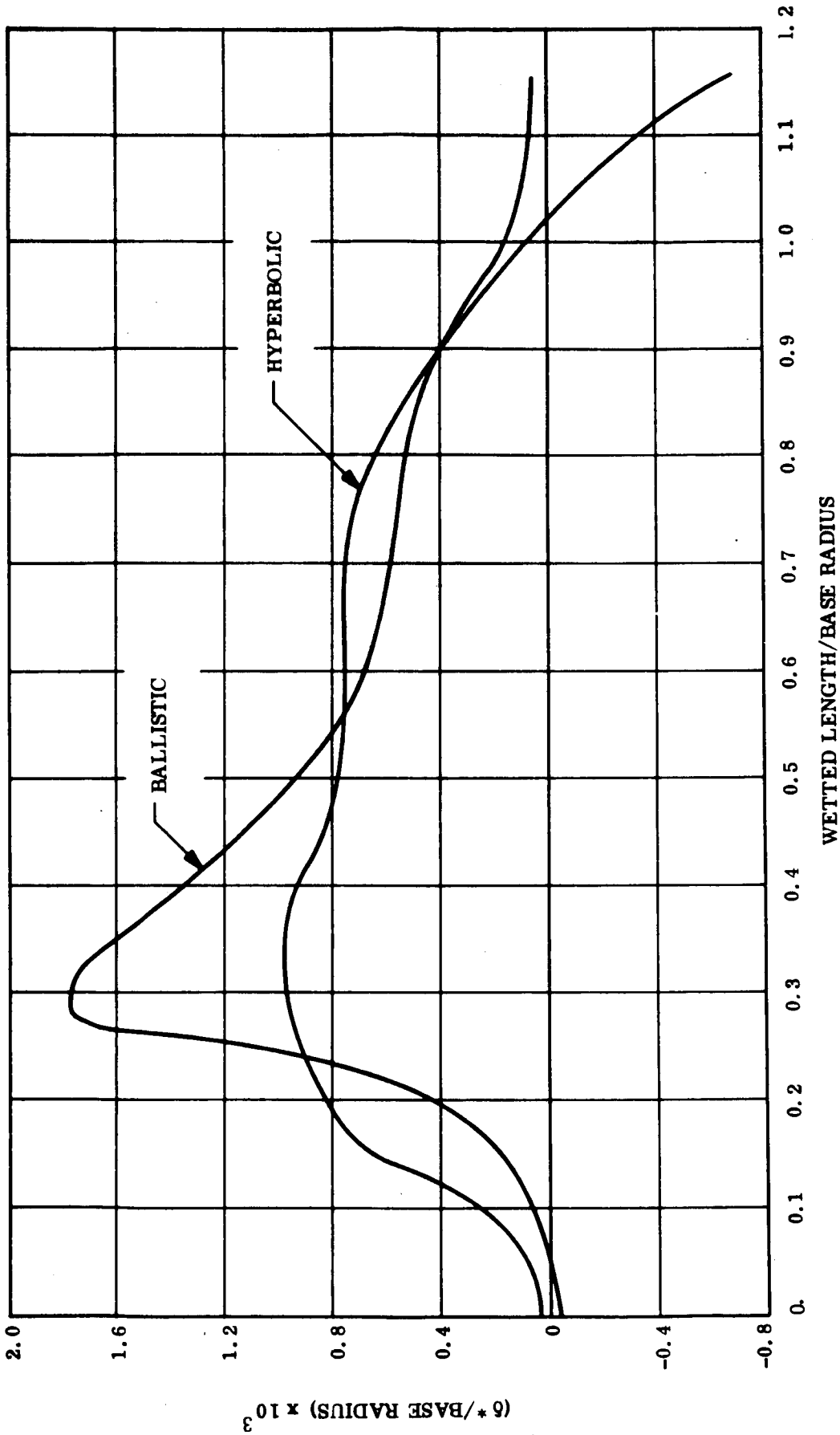

Figure 5-16. Sphere–Cone Displacement Thickness

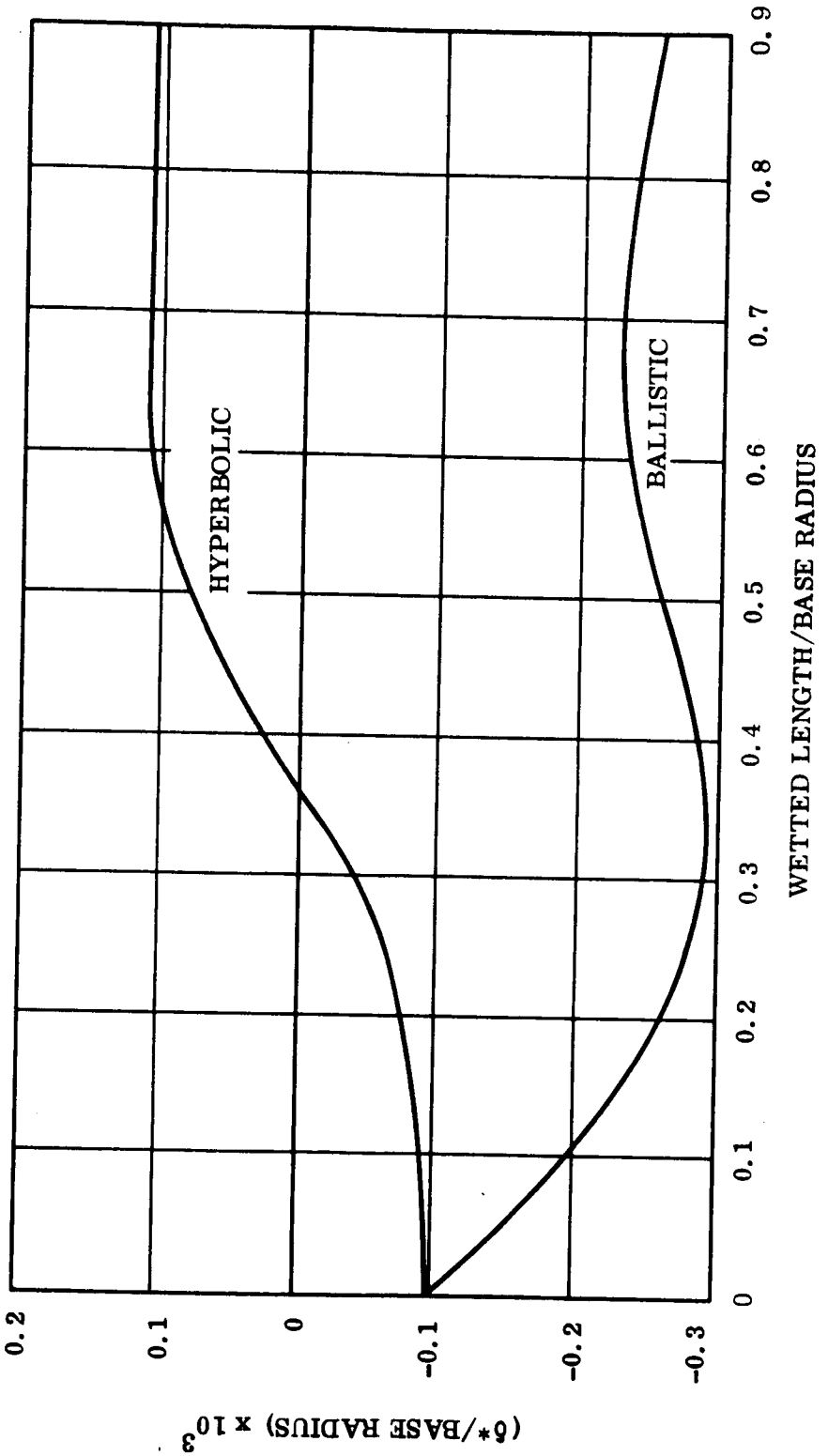

Figure 5-17. Sphere-Cap Displacement Thickness

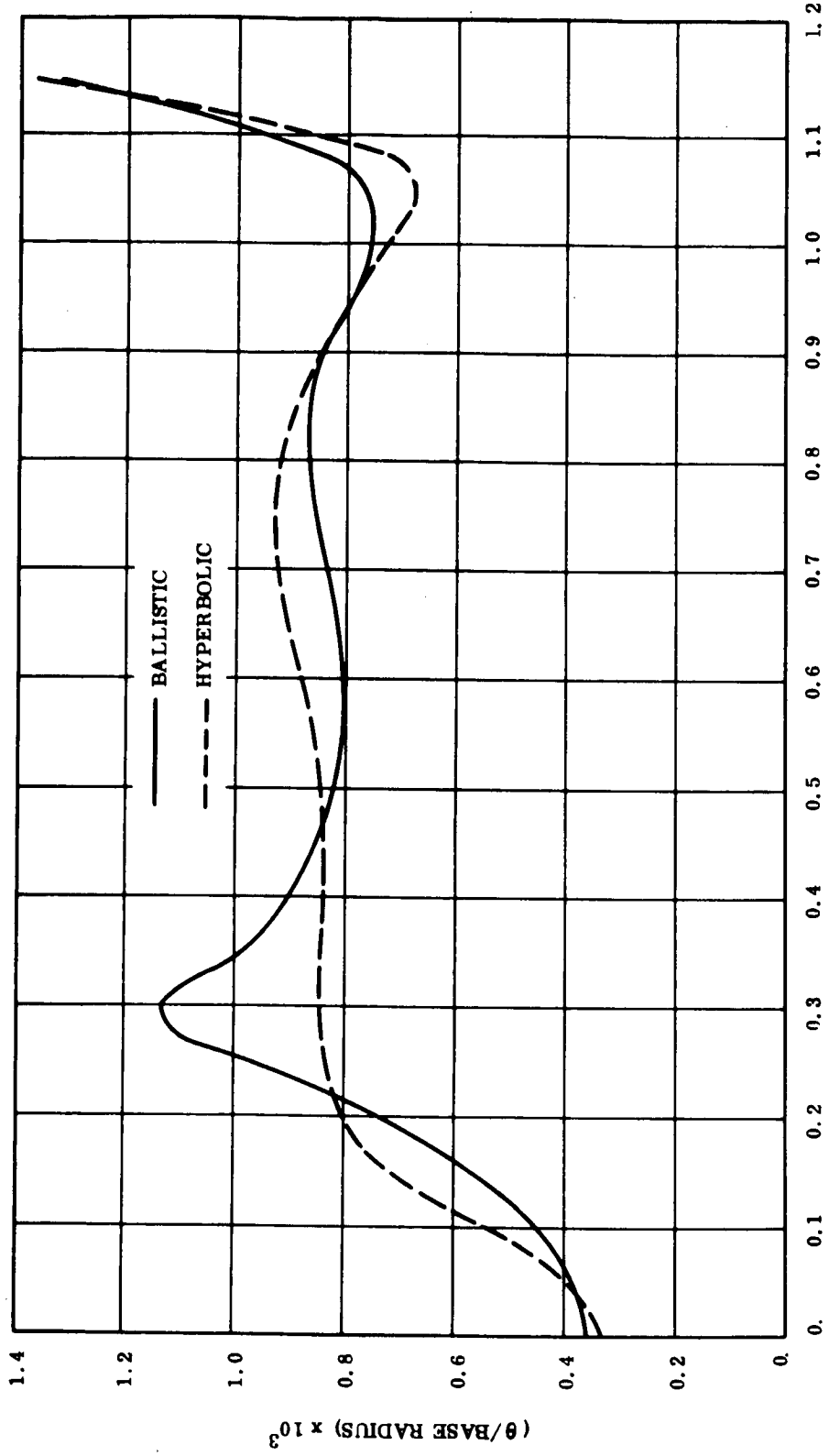

Figure 5-18. Sphere-Cone Momentum Thickness

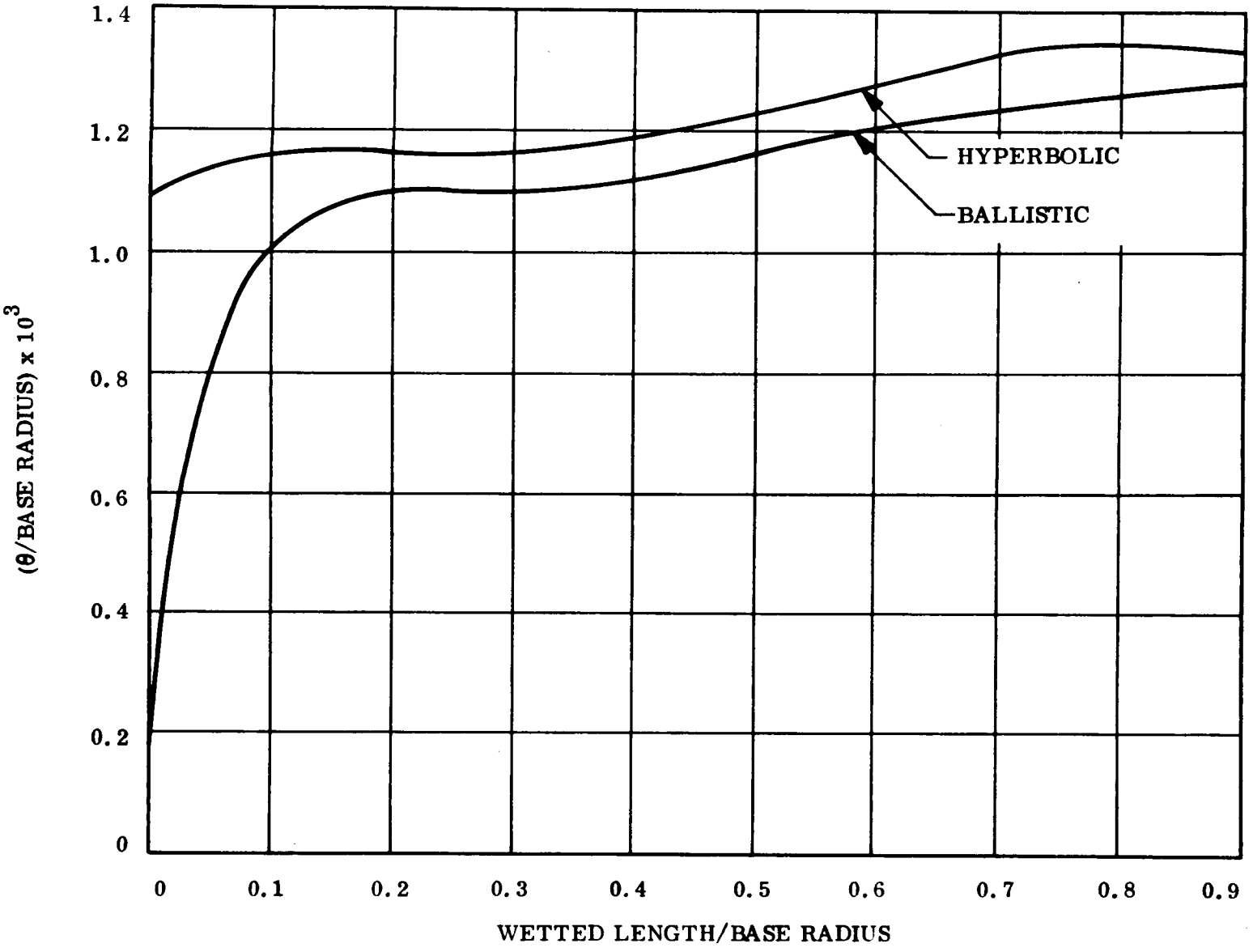

Figure 5-19. Sphere-Cap Momentum Thickness

one of the requirements for the use of the boundary layer equations, as discussed in Section 2, has not rigorously been met. However, as pointed out in that Section, the use of the more applicable low Reynolds number equations would produce an effective viscous flow thickness less than those above, so that the disturbance to the inviscid flow would be less than that indicated above. The overall effect on the heat transfer, as shown in Figure 2-1, would be an increase of only 10 to 12 percent for the sphere-cone cases, and approximately 4 percent for the sphere-cap configurations.

Density and temperature boundary layer profiles at the stagnation point (Station 1 in Figure 5-20) appear in Figures 5-21 through 5-24. Similar profiles at Station 3 are plotted in Figures 5-25 through 5-28. All parameters have been normalized by their values at the boundary layer edge in order to facilitate comparison between the hyperbolic and ballistic cases.

The viscous contributions to the drag force are negligible.

5.3 RADIATIVE HEATING

Results obtained from the radiative heating computations include: (1) the radiative heat flux at four body points for the sphere cap configuration and seven body points for the sphere cone configuration, (2) the spectral distribution of the radiative heating at each body point for each

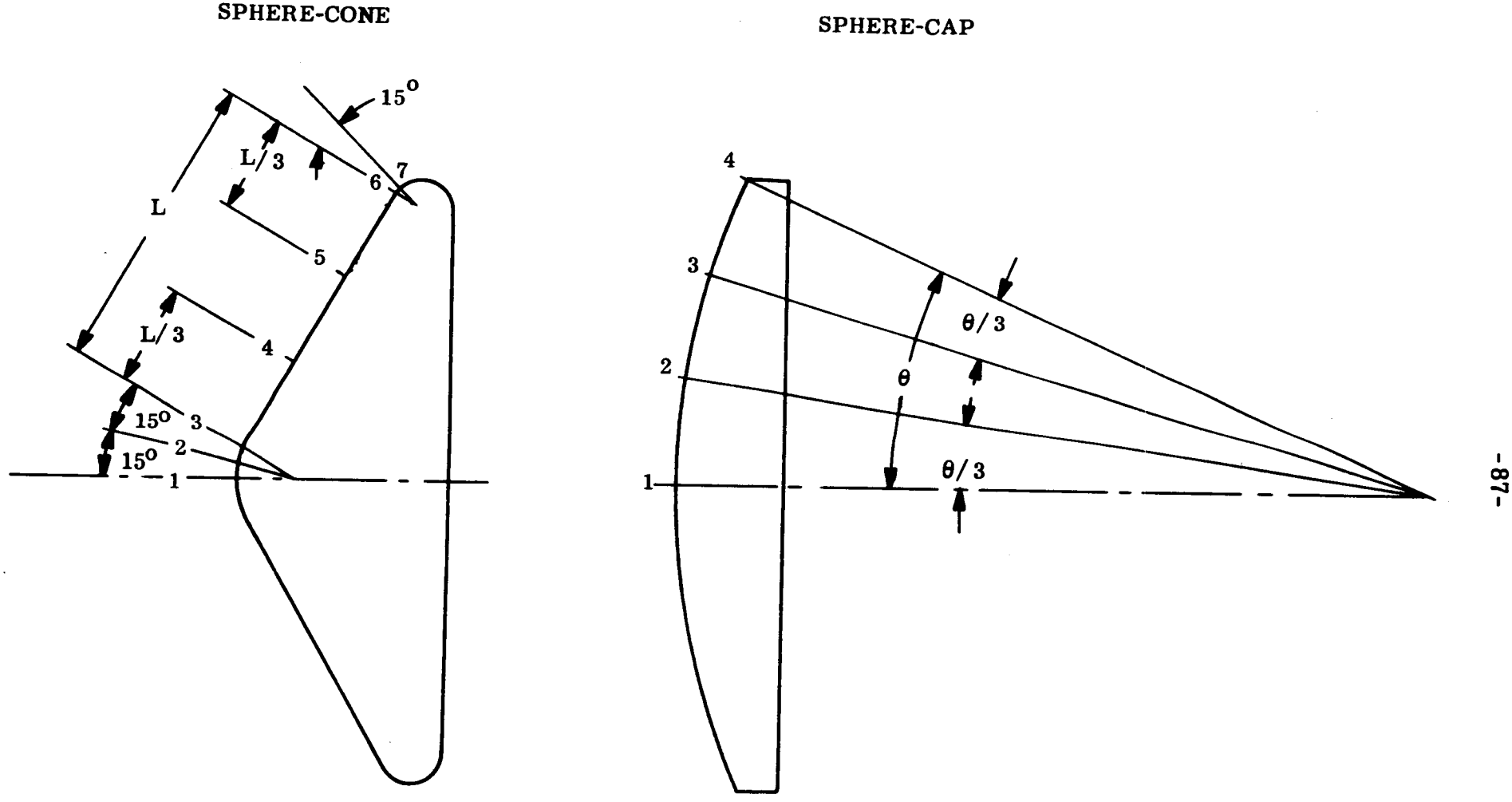

Figure 5-20. Location of Stations

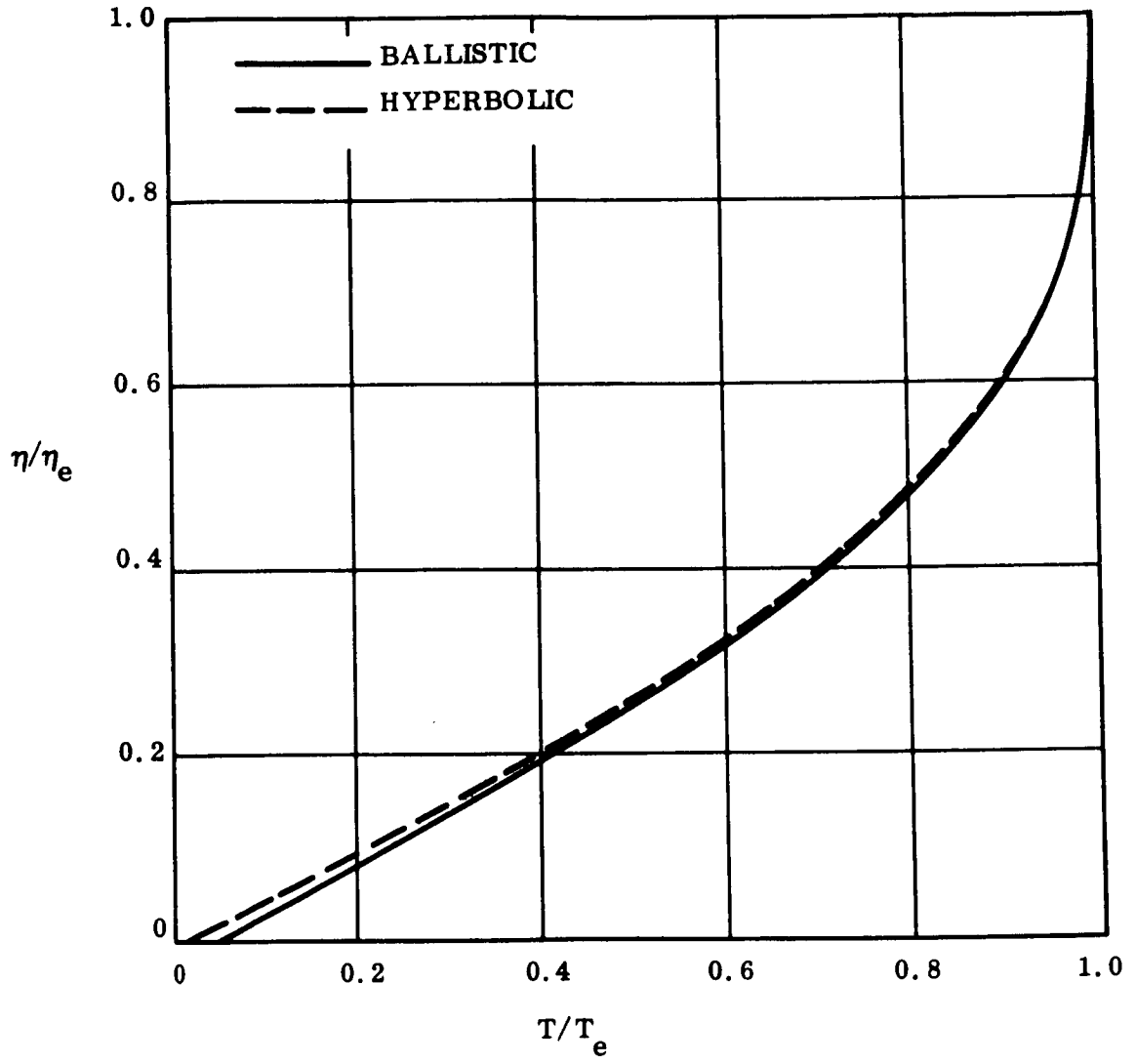

Figure 5-21. Sphere-Cone Boundary Layer Temperature Profiles (Station 1)

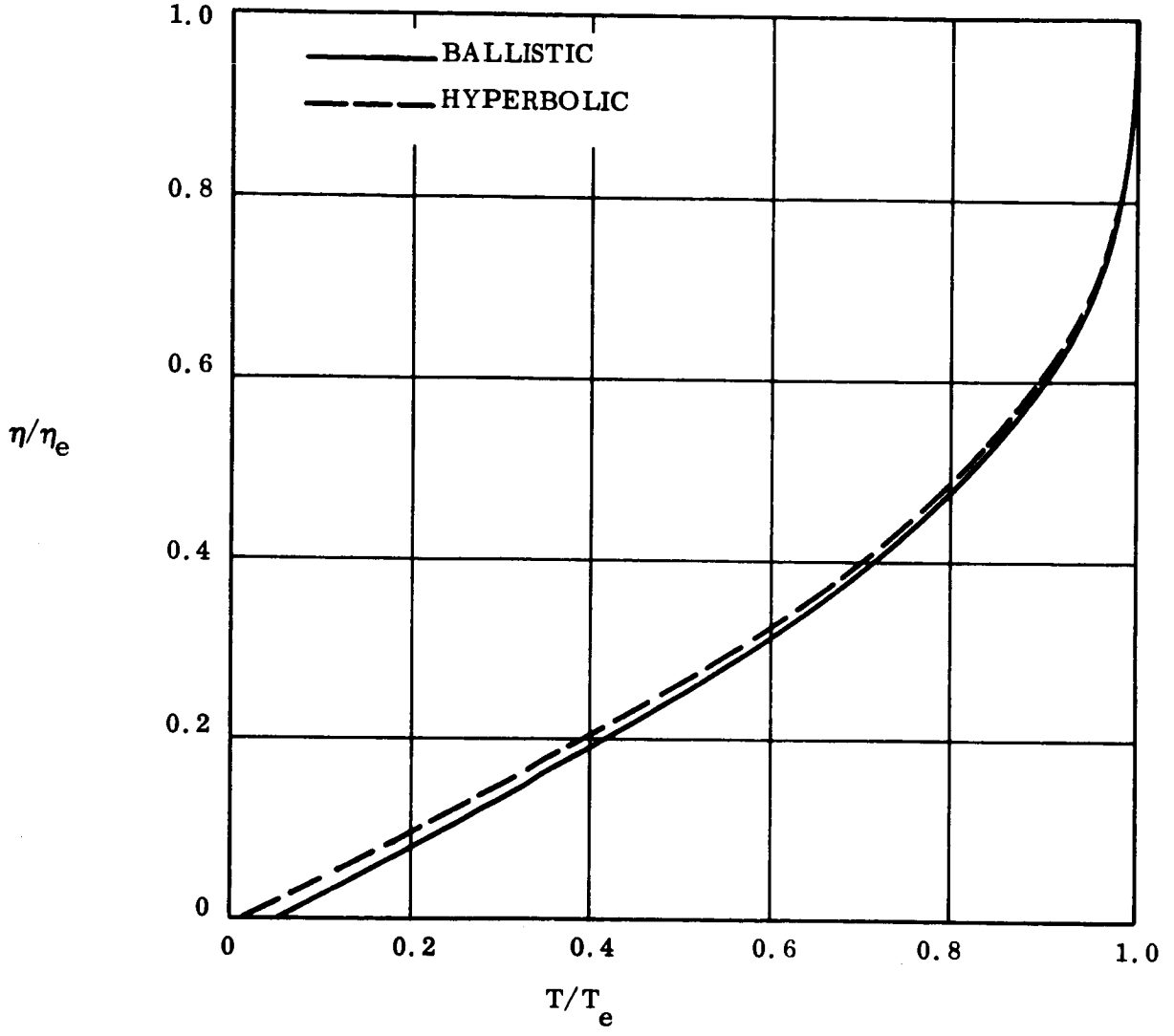

Figure 5-22. Sphere-Cap Boundary Layer Temperature Profiles (Station 1)

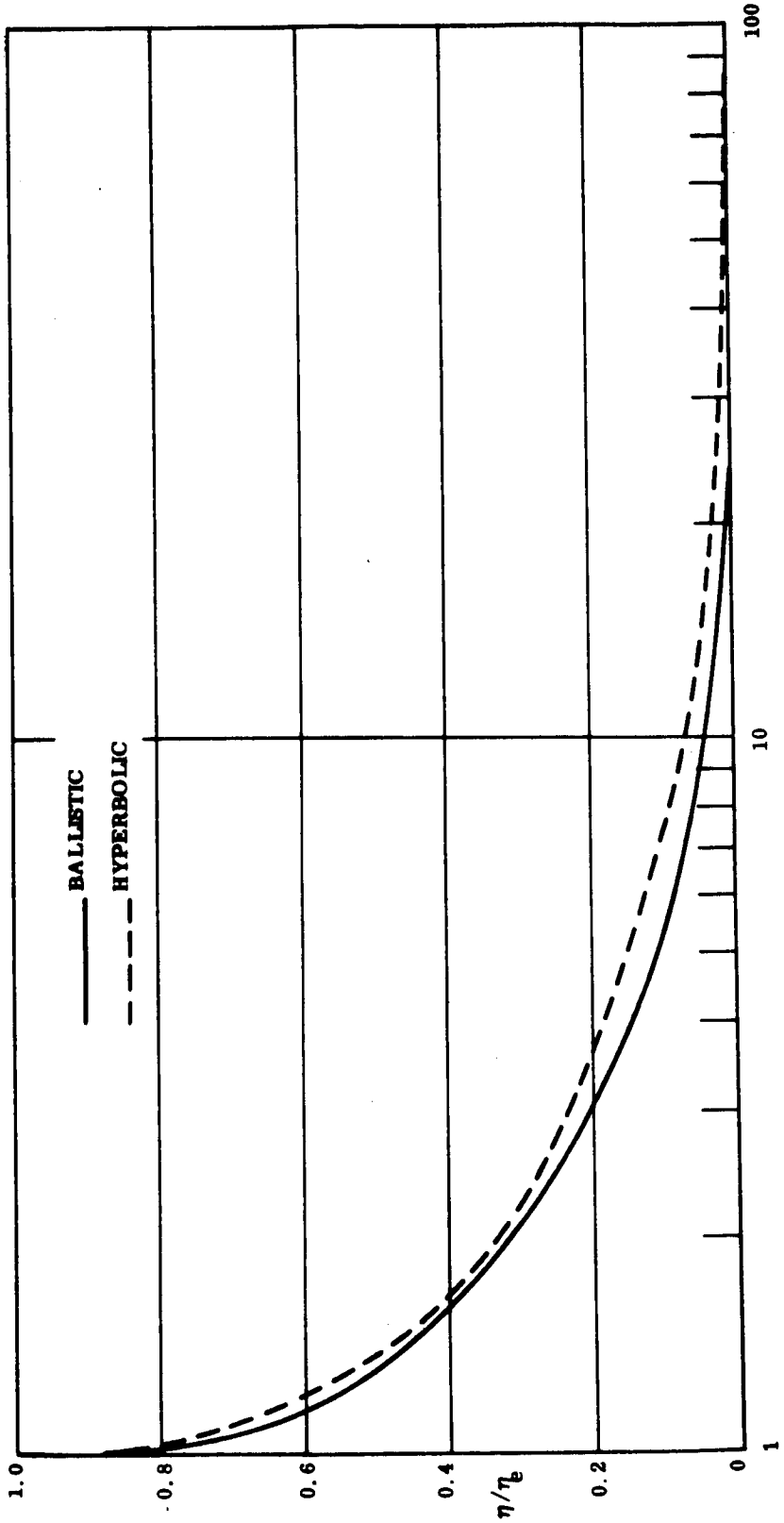

Figure 5-23. Sphere-Cone Boundary Layer Density Profiles (Station 1)

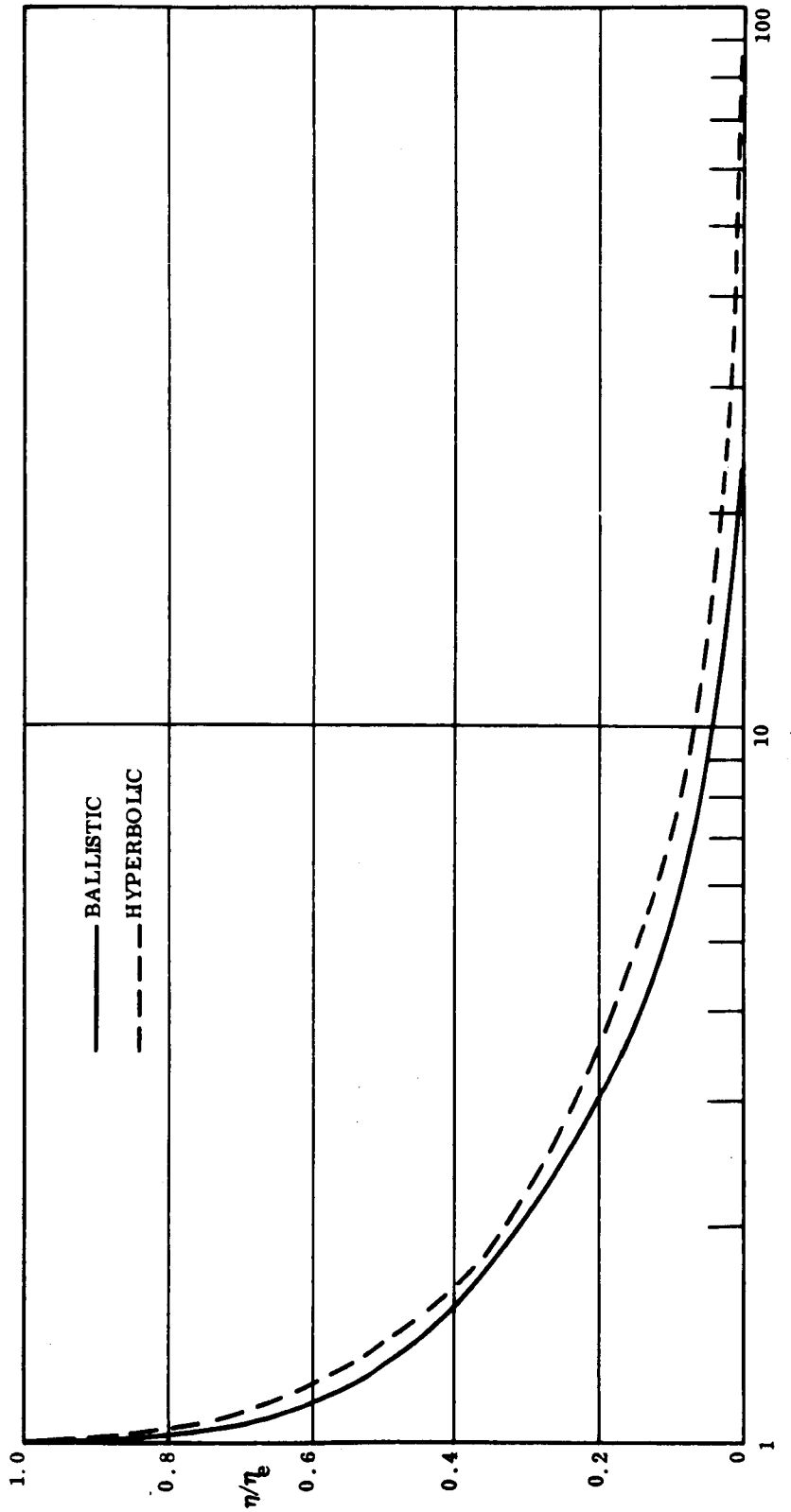

Figure 5-24. Sphere-Cap Boundary Layer Density Profiles (Station 1)

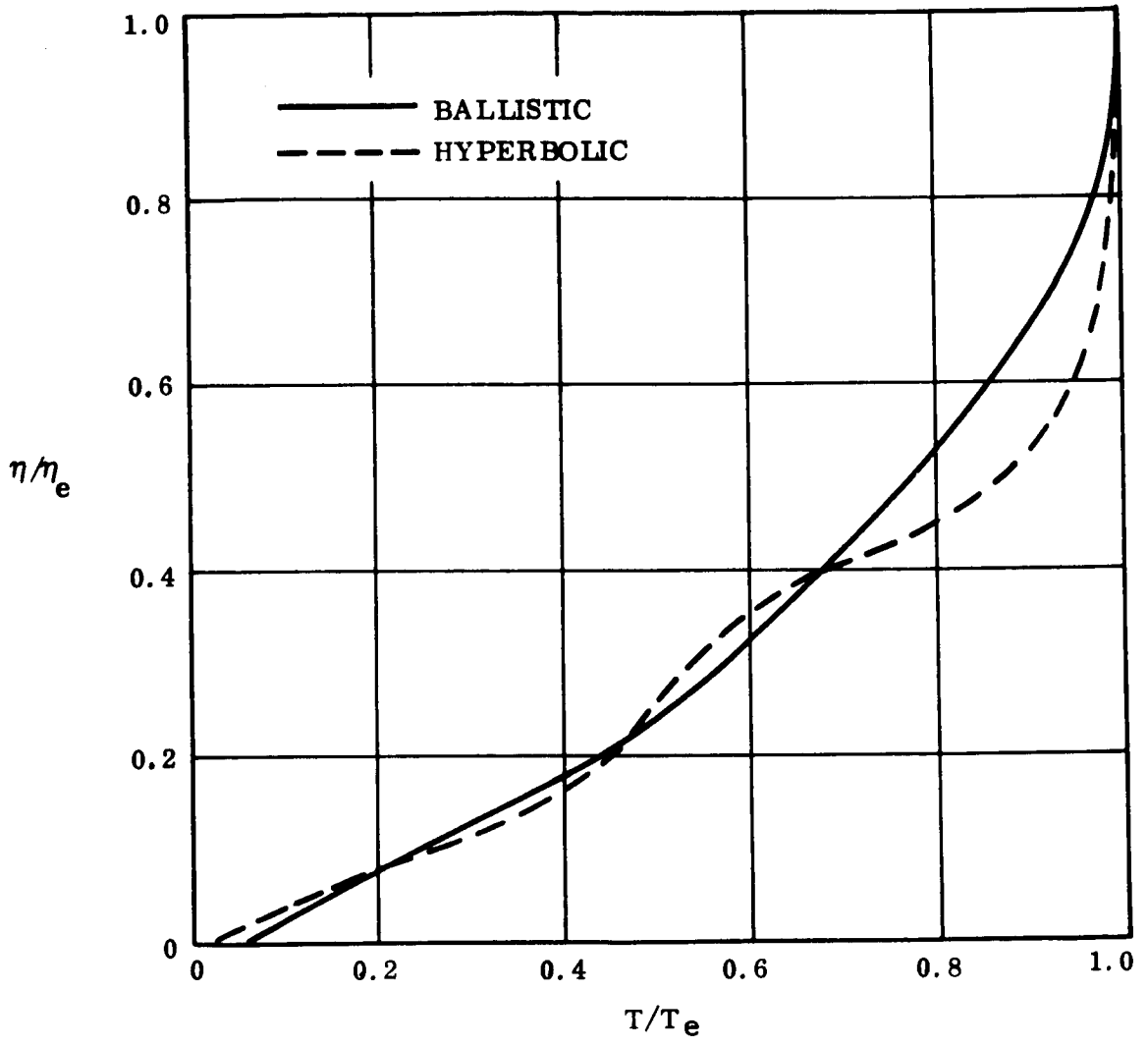

Figure 5-25. Sphere-Cone Boundary Layer Temperature Profiles (Station 3)

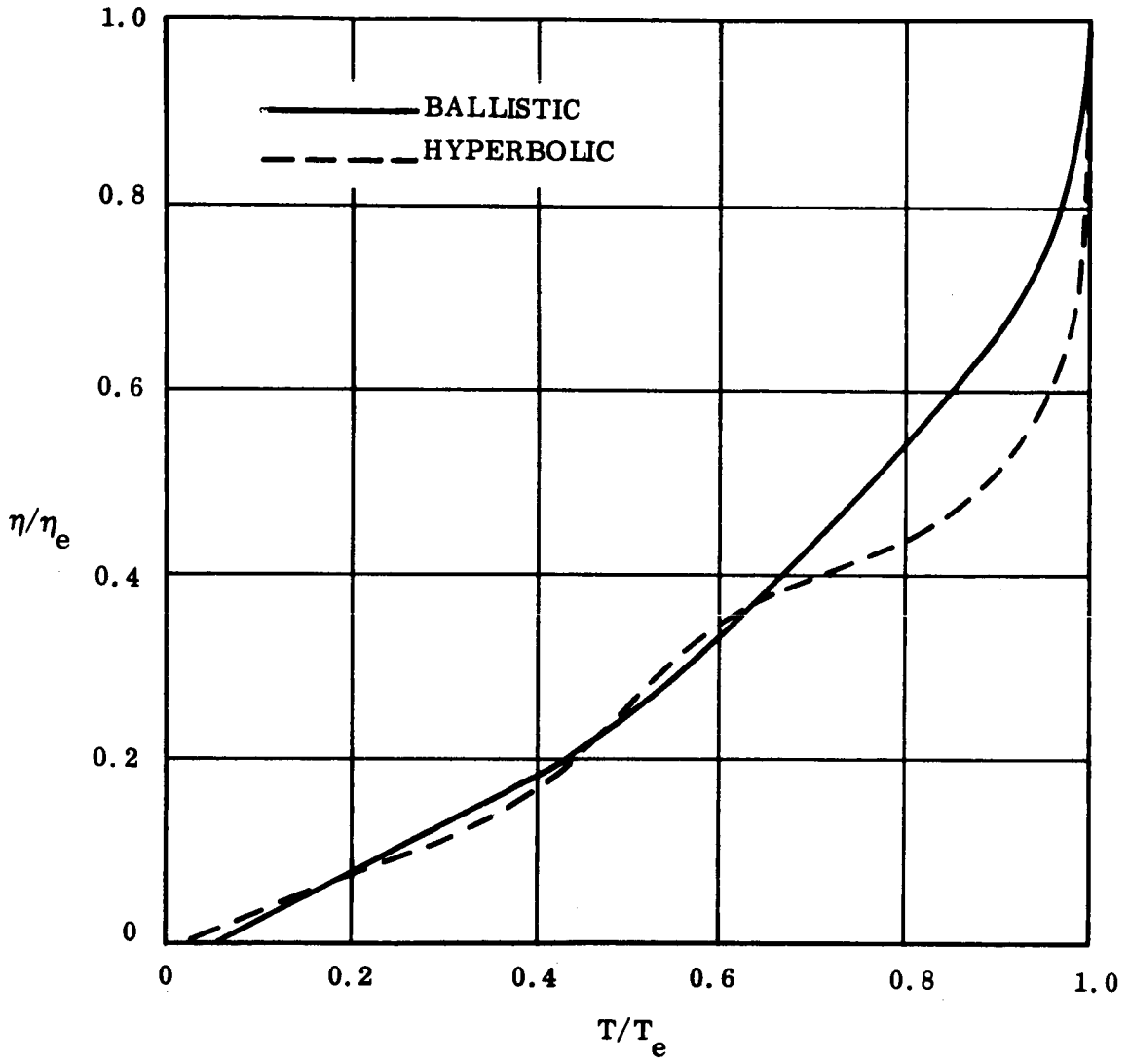

Figure 5-26. Sphere-Cap Boundary Layer Temperature Profiles (Station 3)

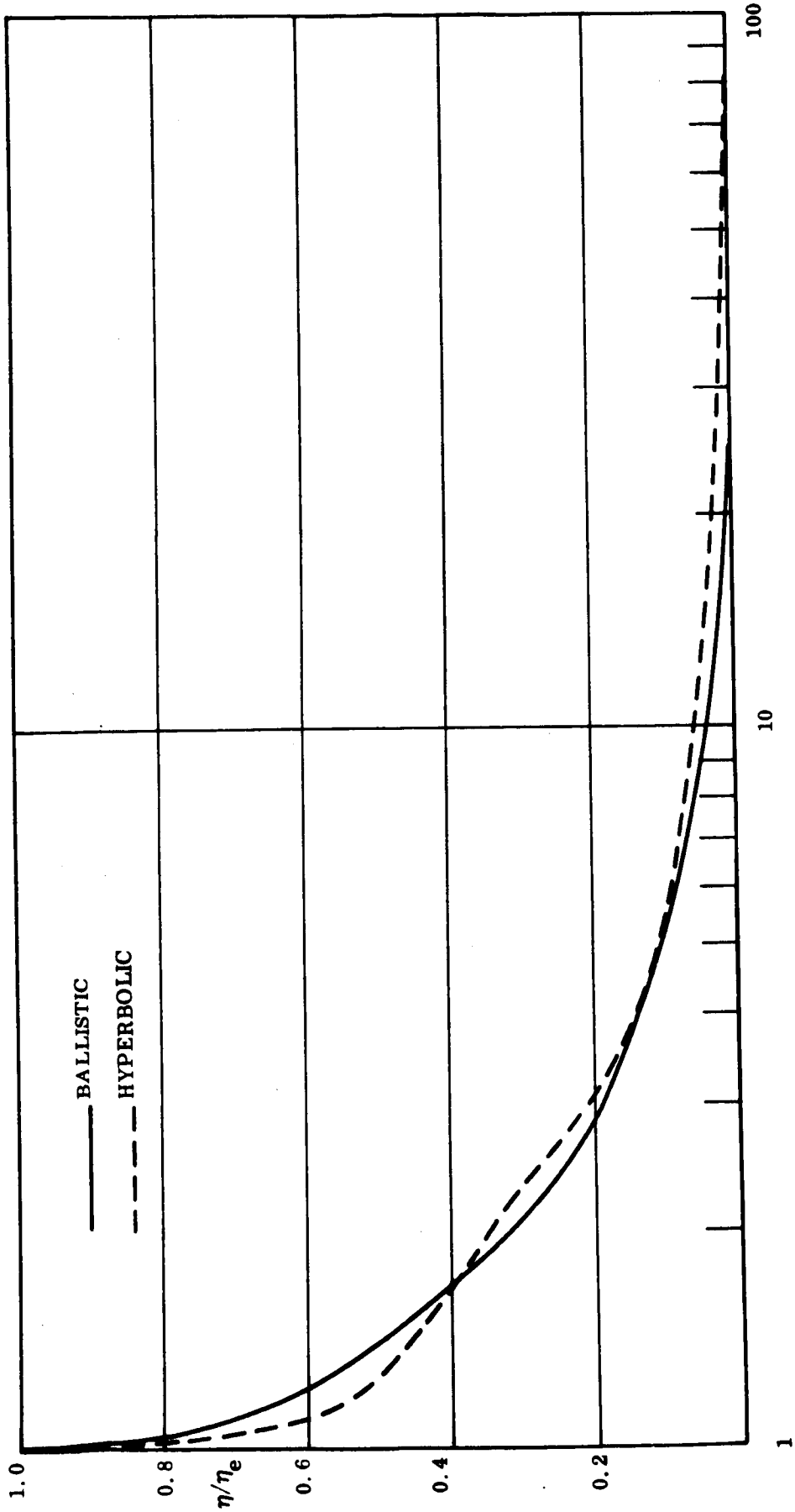

Figure 5-27. Sphere-Cone Boundary Layer Density Profiles (Station 3)

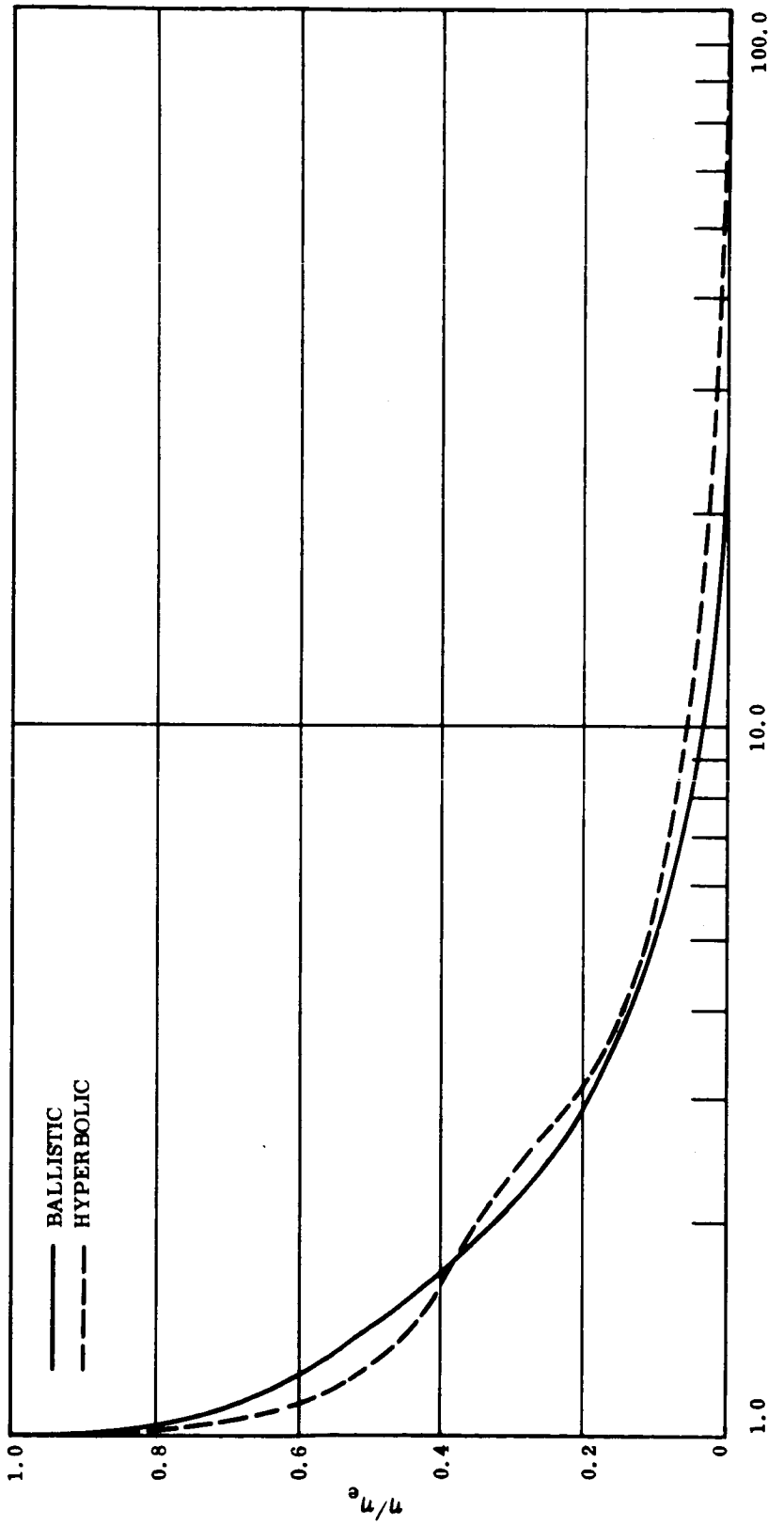

Figure 5-28. Sphere-Cap Boundary Layer Density Profiles (Station 3)

flow field and body configuration, and (3) a comparison of the stagnation point radiative heat fluxes with other methods including an estimate of the optically-thin heating value.

5.3.1 Sphere Cap

Figure 5.29 shows the distribution of the radiative heating for the sphere cap. Both flow field cases are shown on this figure in order to compare the similarities and differences in the trends. It may be seen from the figure that both flow fields give rise to distributions which are similar in the respect of being at a maximum value at the stagnation point and then decreasing in magnitude as s/R_B increases. This is consistent with expected behavior due to the decrease in flow field temperature and density as the flow expands about the body.

The main difference between the shape of the curves is the rate of decrease of the radiative heating with increasing s/R_B. In fact, although the stagnation point radiative heating is higher for the ballistic flow field than for the hyperbolic flow field, the curves cross and show the hyperbolic case to give a higher radiative heating at the corner point. The reason for this is evident when an examination of the flow field properties is made. In the case of the ballistic flow field, the temperature and density are decreasing more quickly as the flow moves away from the stagnation point than it does in the hyperbolic case. Thus, the radiation

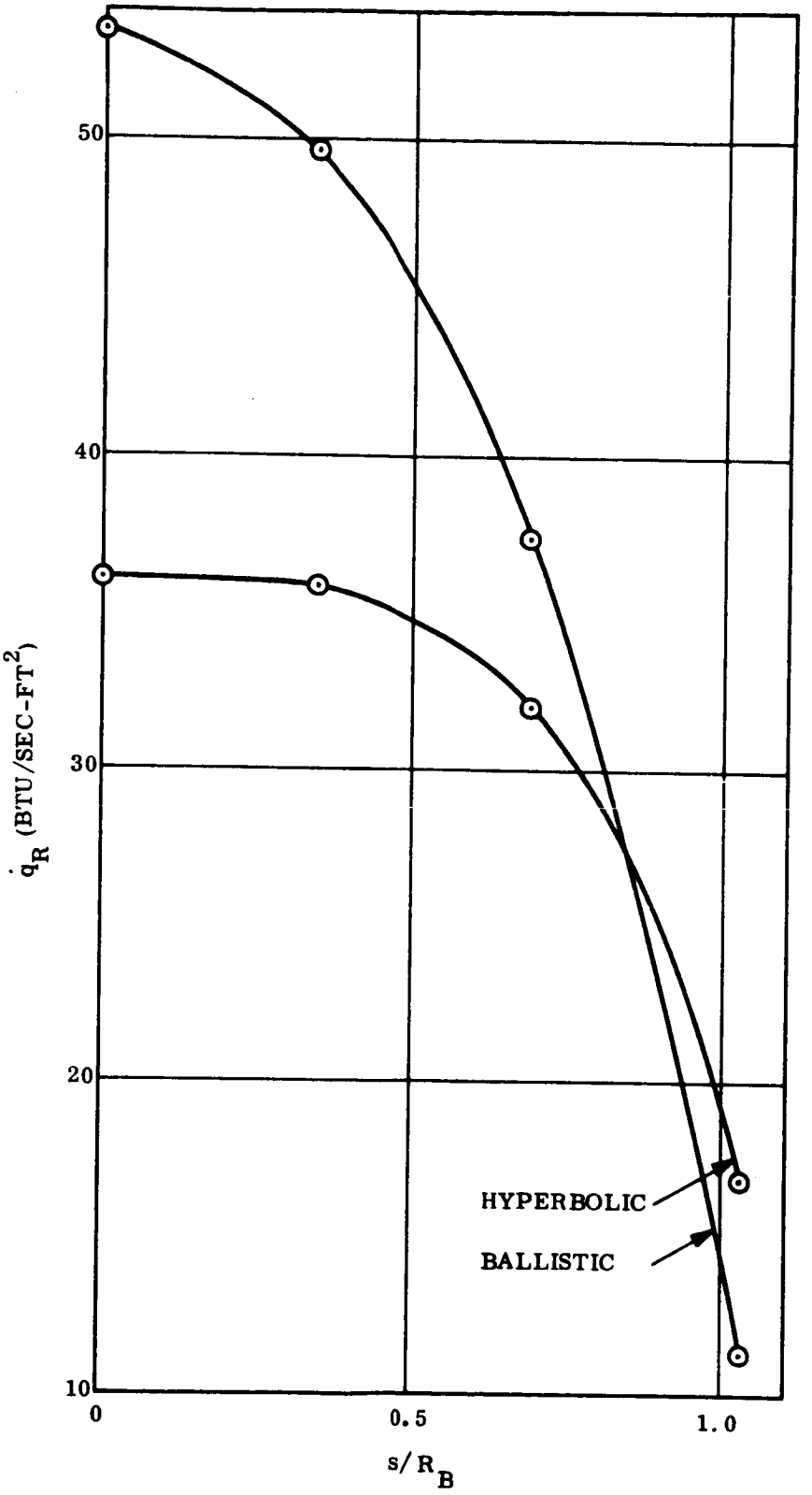

Figure 5-29. Radiative Heating Distribution for Sphere-Cap

also decreases more quickly.

Figure 5-30 shows the spectral distributions of radiation at each of the four body points for the two flow fields. It may be seen that the effect of the difference in flow fields is to change the spectrum at which the radiation is dominant. This difference is caused primarily by the difference in density of the two flow fields. For the hyperbolic case, the radiation is strongest at .4μ, whereas it is strongest at around .3μ for the ballistic case. The radiation is stronger at 1.0μ for the hyperbolic case than for the ballistic case.

5.3.2 Sphere Cone

The radiative heating distribution is shown in Figure 5-31 for the two sphere cone flow fields. Here the radiative heating may be seen to first decrease as the flow rounds the spherical nose and then increase along the cone until it decreases again as the corner or shoulder is reached. Examination of the flow fields shows this trend to occur as follows. The flow first expands around the nose and decreases in temperature and density while retaining an almost constant shock stand-off distance. Along the conical portion of the body, however, the temperature and density remain essentially constant with increasing s/R_B whereas the shock stand-off distance (gas thickness) continually increase. This causes an increase in heating, which if the gas were optically-thin

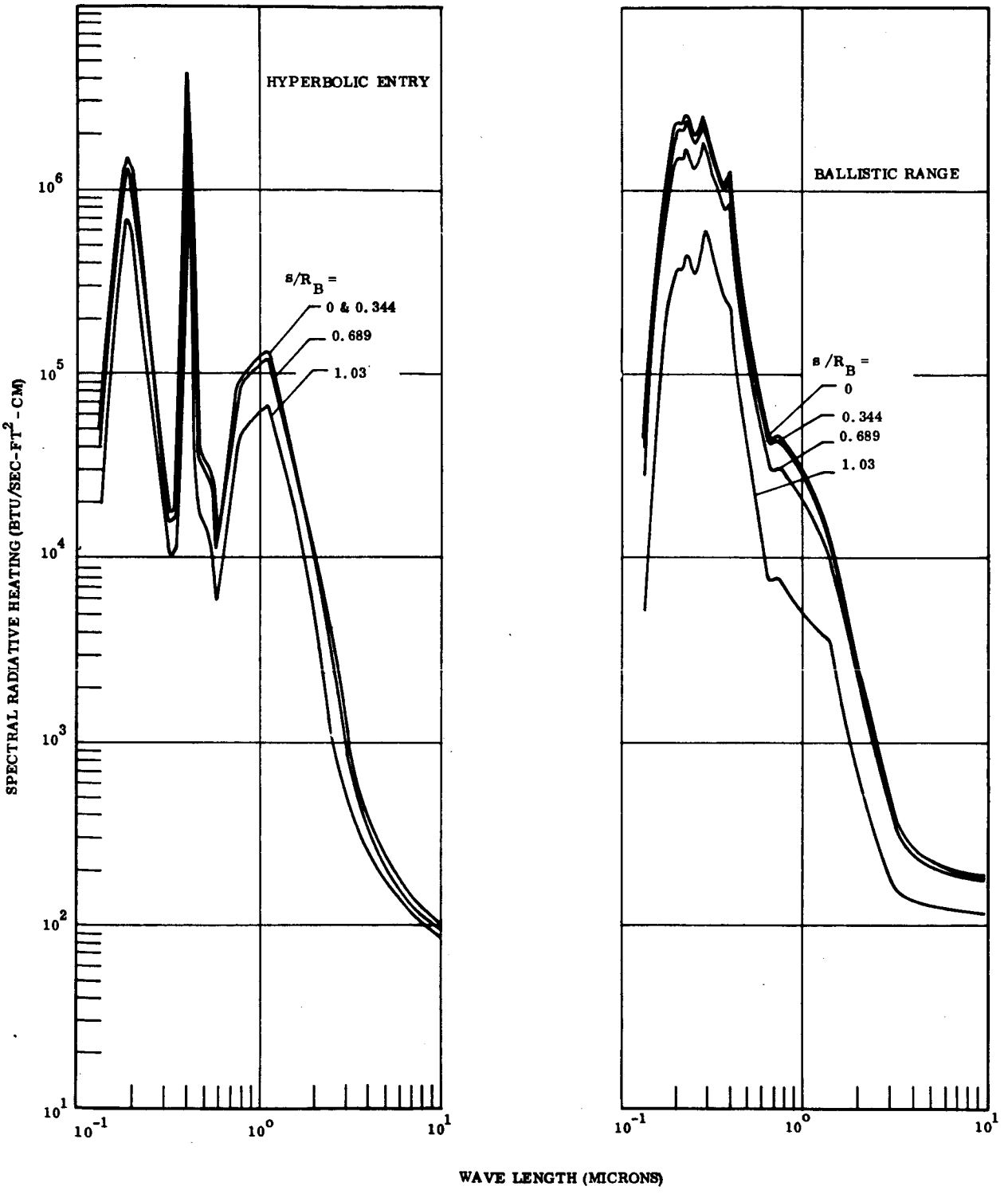

Figure 5-30. Spectral Radiative Heating for Sphere-Cap

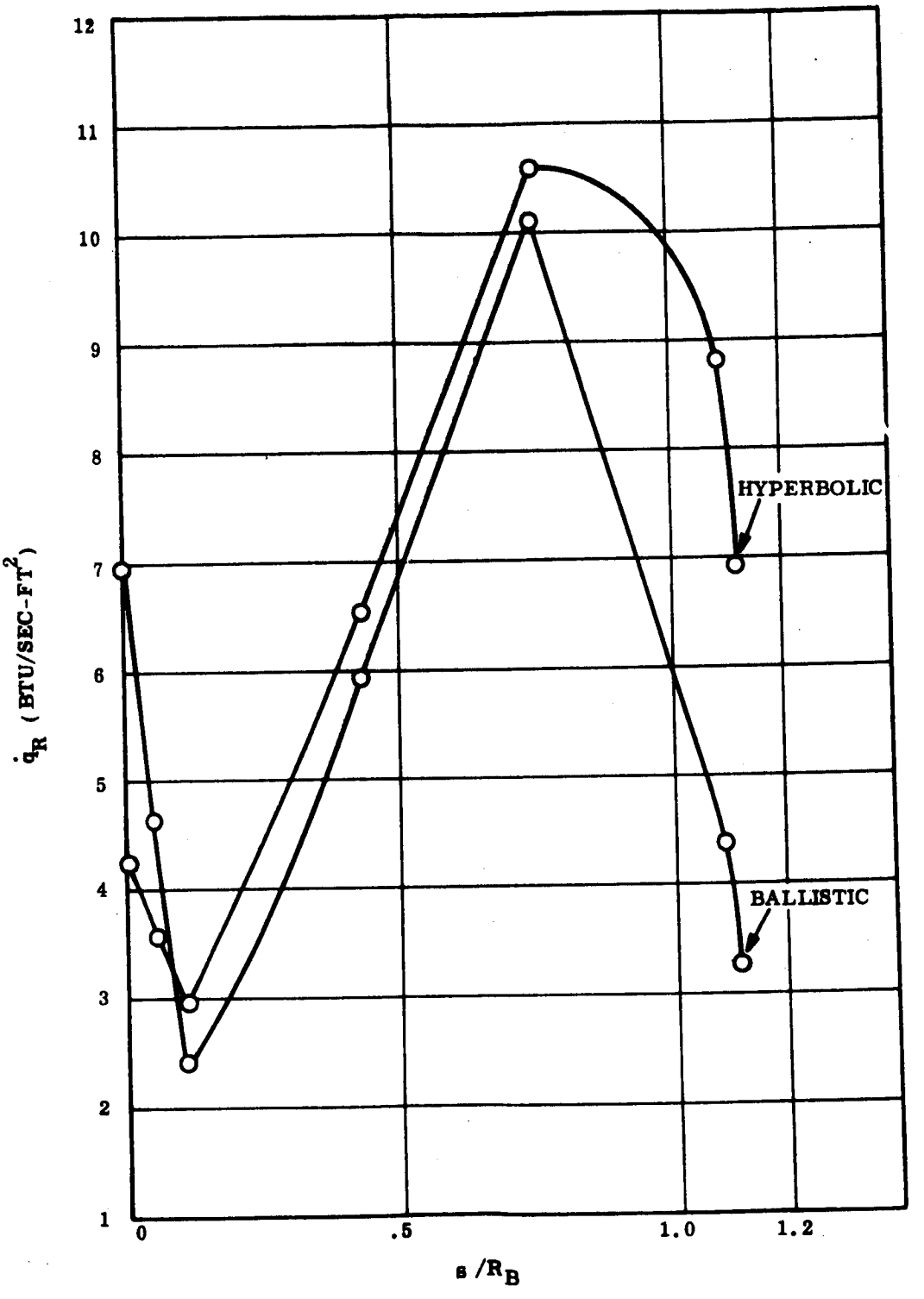

Figure 5-31. Radiative Heating Distribution for Sphere-Cone

would be proportional to the stand-off distance (Δ).

A check on this may be seen by comparing the calculated radiative heating values at body points 4 and 5 of Figure 5-20 (essentially the same temperature and density) with the shock stand-off distances at each point as follows:

HYPERBOLIC:

$$\frac{\dot{q}_{R_5}}{\dot{q}_{R_4}} = \frac{10.61}{6.52} = 1.625$$

$$\frac{\Delta_5}{\Delta_4} = \frac{.057}{.034} = 1.675$$

BALLISTIC:

$$\frac{\dot{q}_{R_5}}{\dot{q}_{R_4}} = \frac{10.11}{5.92} = 1.705$$

$$\frac{\Delta_5}{\Delta_4} = \frac{.0695}{.0385} = 1.805$$

Thus $\frac{\dot{q}_{R_5}}{\dot{q}_{R_4}} \approx \frac{\Delta_5}{\Delta_4}$ and $\frac{\dot{q}_{R_5}}{\dot{q}_{R_4}} < \frac{\Delta_5}{\Delta_4}$ for either case, which indicates the validity of the method, since for an optically-thin gas $\dot{q}_R \sim \Delta$.

As the shoulder or corner of the vehicle is reached, the gas expands and decreases in temperature and density, thus emitting less radiation.

It should be noted that a crossing of the curves for the hyperbolic

and ballistic radiative heating distributions is seen to occur for the sphere cone as it did for the sphere cap and for the same reason.

The distributions as graphed in Figure 5-31 assumed maximum and minimum points of radiative heat flux at body points 5 and 3 respectively. This may not be the case. In order to determine the extreme points (maximum and minimum) for the two curves it would be necessary to calculate the radiative heating at additional body points.

The spectral distribution of radiation at each of the seven body points for the two flow fields is shown in Figure 5-32. These curves show results similar to the spectral distributions obtained for the sphere cap cases. For the hyperbolic case, the radiation is strongest at around .4μ, whereas it is strongest at around .3μ for the ballistic case.

5.3.3 Comparison of Radiative Heating Distributions

In order to compare the radiative heating distributions obtained for the four cases, plots of the normalized radiative flux ($\dot{q}_R/\dot{q}_{R_{st}}$) are shown in Figures 5-33 and 5-34. Figure 5-33 shows the radiative heat flux ratio versus s/R_B whereas Figure 5-34 shows the ratio versus the angle θ ($\theta = 0^o$ at stagnation point) for the sphere cap and the nose region of the sphere cone.

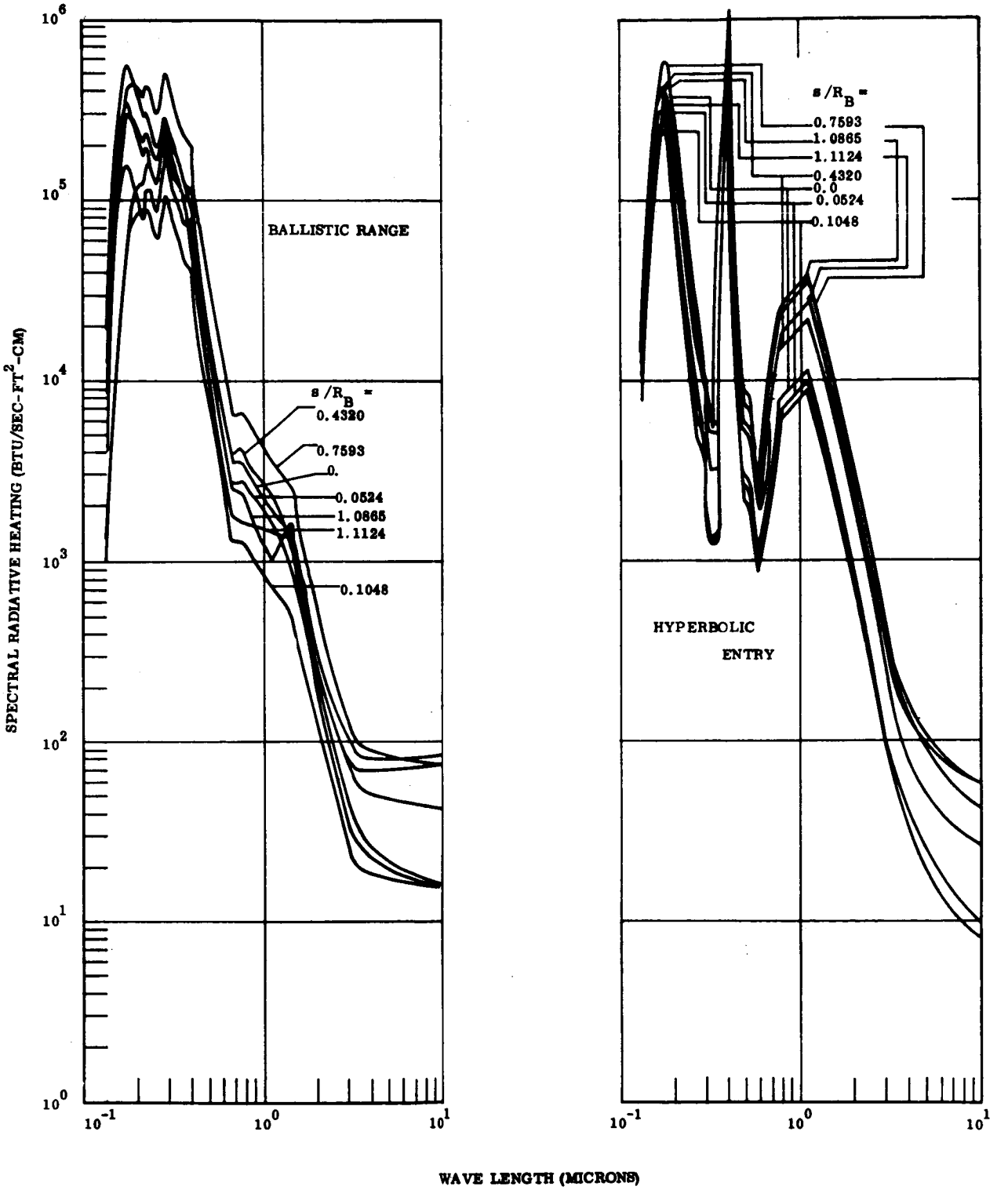

Figure 5-32. Spectral Radiative Heating for Sphere-Cone

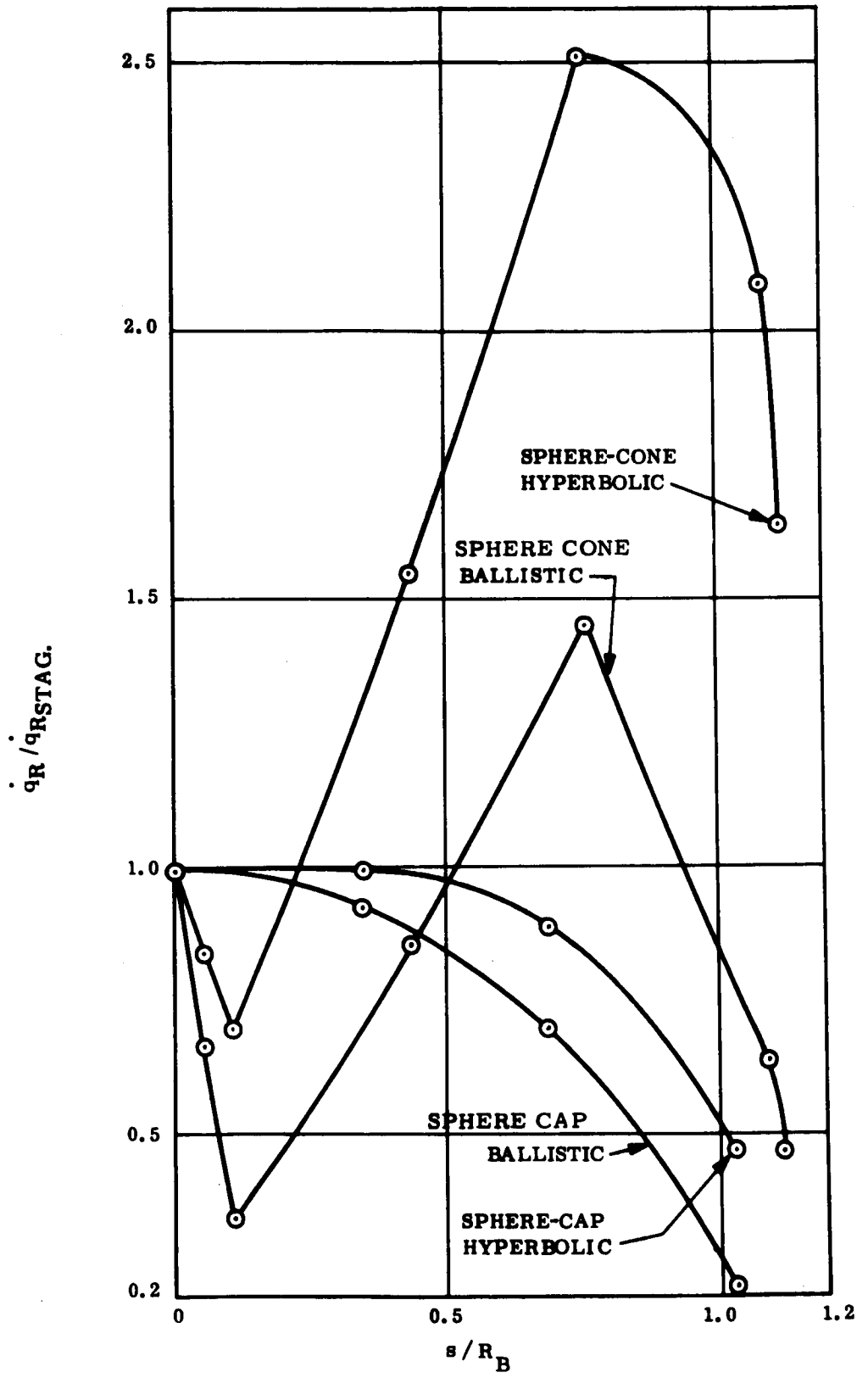

Figure 5-33. Radiative Heating Distribution

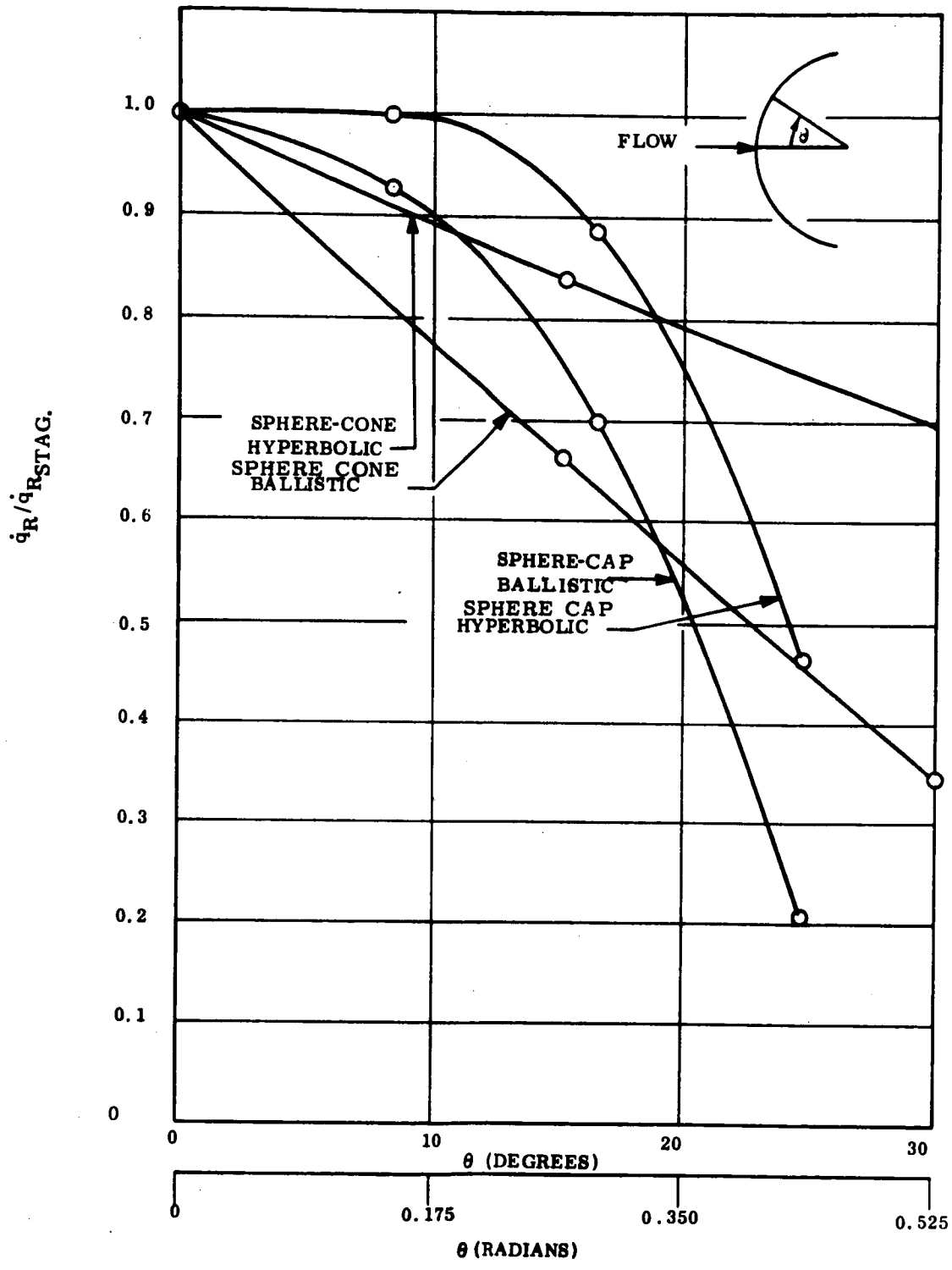

Figure 5-34. Radiative Heating Distribution Around Nose

Again it can be seen that the radiative heating falls off more quickly for the ballistic cases than for the corresponding hyperbolic cases. The radiative heating also may be seen to initially decrease more for the sphere cone cases than for the corresponding sphere cap cases.

It is interesting to note the linear distribution on the nose of the sphere cone as compared with the cosine-type distribution over the sphere cap.

5.3.4 Comparison of Stagnation Point Radiative Heating With Other Methods

Hand calculations of the radiative heating at the stagnation point were performed utilizing the curves presented by Gruszczynski (Reference 3.42). Interpolation of these curves resulted in the radiative heating ($\dot{q}_R$) in watts/cm^2 as a function of path length (L) in cm. for the given stagnation conditions:

1. Hyperbolic $T_{st} = 5,750^{\circ}K$, $\rho_s/\rho_o = 6.36 \times 10^{-3}$
2. Ballistic $T_{st} = 5,700^{\circ}K$, $\rho_s/\rho_o = 2.3 \times 10^{0}$

Additional cases were run using the Hot Gas Radiation (HGR) Program at path lengths other than the four stagnation point shock detachment distances. These points were then plotted as shown in Figure 5-35 (hyperbolic) and Figure 5-36 (ballistic).

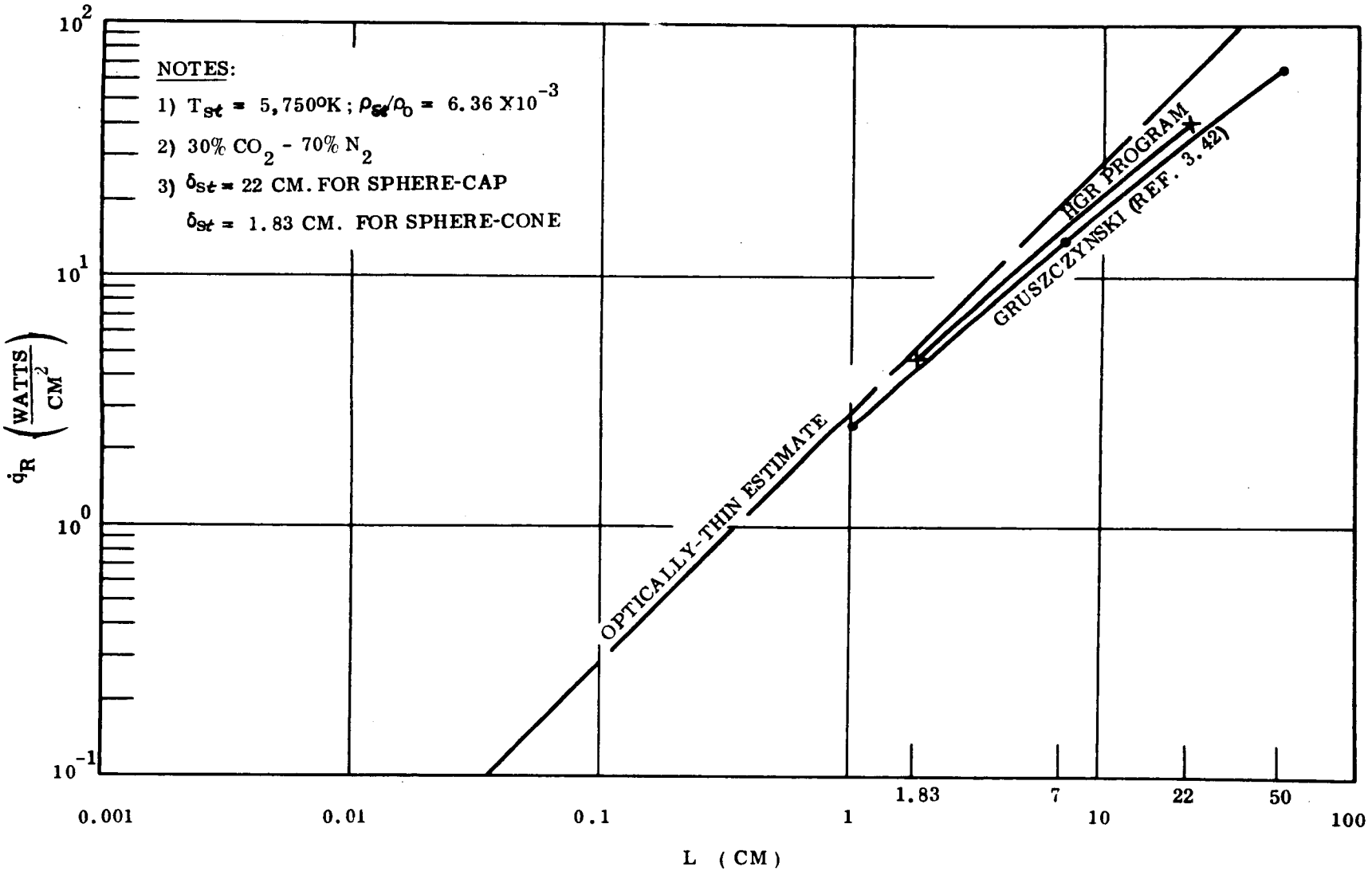

Figure 5-35. Radiative Heating Versus Path Length for Stagnation Point of Hyperbolic Entry Flow Fields

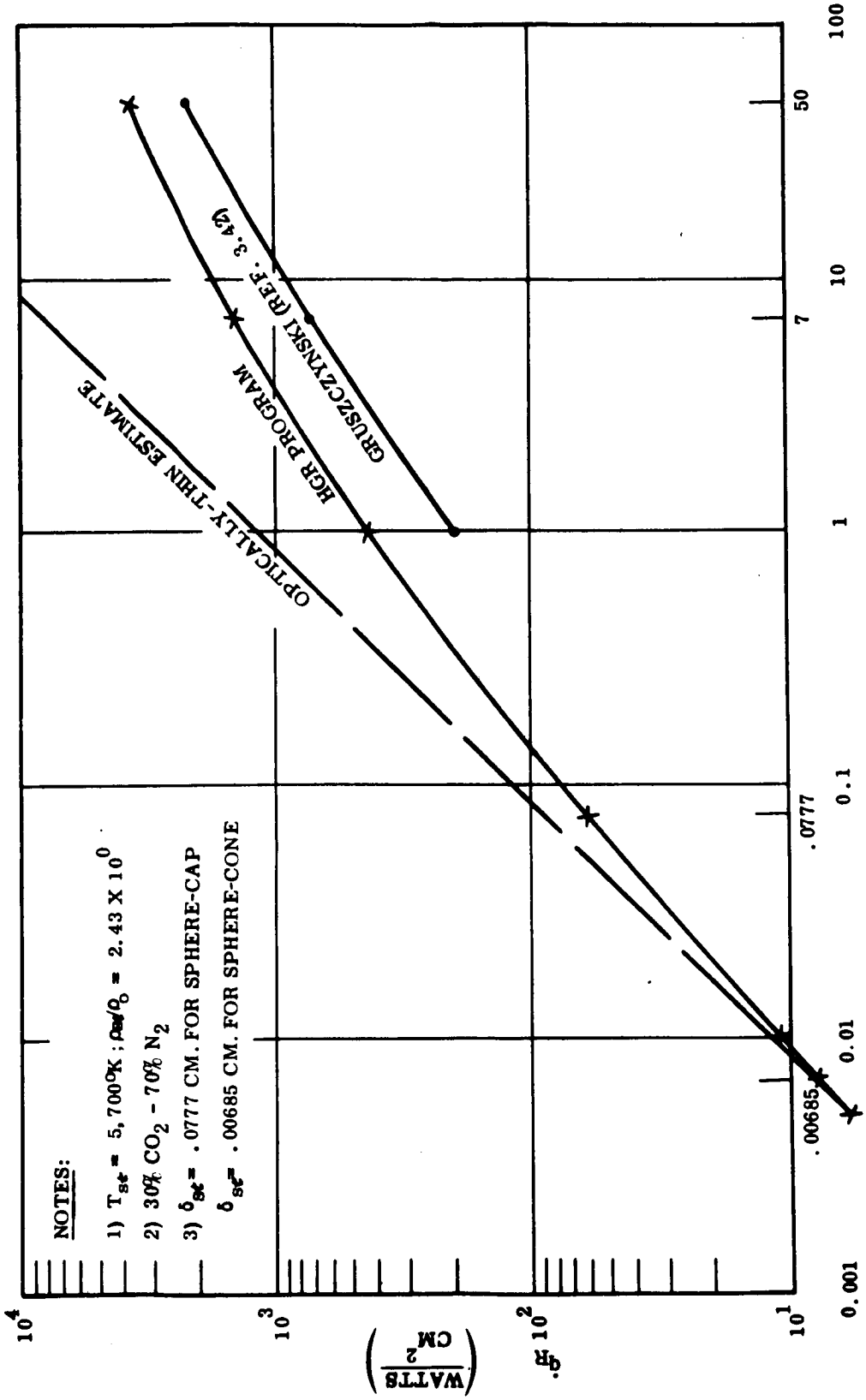

Figure 5-36. Radiative Heating Versus Path Length for Stagnation Point of Ballistic Range Flow Fields

Excellent agreement was obtained between the two sets of results for the hyperbolic cases as shown in Figure 5-35. The HGR Program calculations were approximately 10% higher than the hand calculations. For the ballistic case, however, there is a difference of a factor of approximately 2 at the path lengths greater than 1 cm. (Reference 3.42 does not consider path lengths less than 1 cm.).

As a further check of the radiation calculations, an estimate was made of the amount of radiation from an optically-thin gas at the same temperature and density. This should be an upper limit to the amount of permissible radiation and appears to agree with the calculations performed. (See Figures 5-35 and 5-36.)

5.4 RADIATIVE COUPLING

As discussed previously in Section 2, when radiation from the hot gas layer surrounding a body is an appreciable magnitude, the local flow field properties (especially the temperature) can be affected significantly since the temperature will be reduced due to the radiation of energy away from the flow field.

In order to evaluate the magnitude of this coupling effect, the region near the stagnation point is usually examined, since the radiative heating at that point is usually the maximum. In Section 5.3 of the present study, it was seen that the radiative heating for the sphere-cone configurations reaches a maximum up near the shoulder region. However, in the hyperbolic entry flight condition, the stagnation point of the sphere-cap configuration has a radiative heating value which is still 3.5 times the maximum value of that for the sphere-cone. Therefore, the stagnation point heating of the sphere-cap hyperbolic entry case will be examined for the magnitude of the coupling present. Because of their higher levels of free stream energy, the ballistic range cases have less coupling even with their higher heating rates than do the hyperbolic entry cases.

The maximum level of coupling in the present study can now be evaluated in terms of the coupling parameter utilized in Section 2.2; i.e.,

the ratio of energy radiated from the stagnation region to the energy available to the flow.

$$\Gamma = \frac{2\dot{q}_r}{\frac{1}{2}\rho_\infty u_\infty^3} = .0149$$

where $\dot{q}_r = 36.03$ Btu/ft^{2}sec. The coupling is thus still of the order of 1.5 percent, approximately 50 percent greater than that estimated in Section 2.2. Since the maximum value of the coupling ratio is so small, the effect on the inviscid flow properties, and consequent reduction of shock layer temperatures is insignificant in all the cases considered.

The enthalpy change implied by this magnitude of radiative heating is

$$h_{rad} = \frac{2\dot{q}_r}{\rho_s u_s} = \frac{2\dot{q}_r}{\rho_\infty u_\infty} = 118. \text{ Btu/lb.}$$

The total enthalpy available is 7670. Btu/lb. Since the convective heating is primarily dependent on the enthalpy levels in the shock layer near the body, such small changes in enthalpy level should produce an insignificant change in the convective heating results.

Section 6

CONCLUSIONS DRAWN FROM STUDY

The following conclusions can be drawn as a result of the computations performed in this study:

1. Good simulation of hyperbolic entry radiative heating is achieved on some portions of the ballistic range models. For the sphere-cap configuration, good simulation of the radiative heating is achieved near the shoulder while poor simulation is evidenced toward the stagnation point (Figure 5.29). For the sphere-cone configuration, good simulation occurs on the conical portion of the body, while poor simulation is achieved at the spherical nose and at the spherically rounded shoulder (Figure 5.31).

2. Non-optically thin radiative calculations are necessary in the case of the sphere-cap configurations, whereas the small optical path lengths which pertain to the sphere-cone configurations give rise to radiation which is nearly optically-thin (Figures 5.35 and 5.36).

3. Treatment of the radiation in a spectral manner is necessary for determination of the total radiative heating at a point. Figures 5.30 and 5.32 indicate the large variation of spectral radiative heating with wave length for the sphere-cap and sphere-cone configurations, respectively.

4. The inviscid-radiative coupling and convective-radiative coupling effects are negligible. The coupling, in terms of the ratio of the energy

radiated from the stagnation region to the energy available to the flow, was found to be 1.5 percent for the worst case of the sphere-cap hyperbolic entry.

5. Whereas the peak radiative heating for the sphere-cap configurations occurs at the stagnation point, the peak value for the sphere-cone configurations occurs on the conical afterbody near the rounded shoulder. In the latter cases the body point near the shoulder, Point 5, is exposed to a much larger segment of the shock layer than the stagnation point. And since the temperatures within the shock layer along the conical afterbody have decreased only slightly from the stagnation value, the radiative heating to Point 5 is large.

6. For the sphere-cap configuration at the hyperbolic entry flight condition, the peak local radiative heating value (36 Btu/ft^2 sec at the stagnation point, Figure 5.29) is of the same order as the peak local convective heating value (29 Btu/ft^2 sec at the stagnation point, Figure 5.13). For the sphere-cone configuration at the hyperbolic entry flight condition, the peak local radiative heating value (10 Btu/ft^2 sec at Point 5, Figure 5.31) is an order of magnitude less than the peak local convective heating value (98 Btu/ft^2 sec at the stagnation point, Figure 5.12), and is still only 20% of the corresponding local convective heating value at Point 5 (50 Btu/ft^2 sec, Figure 5.12).

Section 7

SUGGESTIONS FOR ADDITIONAL WORK

The following sections present discussions of several areas of additional studies which will expand the usefulness of the results of the present study.

7.1 EXTENSION OF RADIATION AND OPTICALLY THIN CALCULATIONS

As indicated in Section 5.3, the points of maximum and minimum radiative heat transfer for the sphere-cone shapes are not definitely established from the calculations performed in this study. Calculations at several additional points would serve to better define the variation in radiative heating over those bodies.

For the present study, the radiative calculations at all body stations included the effects of self-absorption; i.e., the gas was considered to be non-optically thin. It is of interest to determine the differences in magnitude of the radiative heat transfer when the gas is treated as optically thin. Within the range of this study, it was only possible to determine this for the stagnation point values, using the method discussed in Section 4.3. However, similar optically thin calculations can be made for the radiation to the body points away from the stagnation region. This would provide an evaluation of the use of this simplifying assumption in estimates of total radiative heating to the body.

7.2 IDENTIFICATION OF MAJOR RADIATION CONTRIBUTORS

Within the present study, the spectral distribution of the total energy radiated to a point on the body is provided. It would also be of

interest to identify in a quantitative way the relative contributions of the various radiating systems given in Table 3. 3 to the total radiation as a function of wavelength for the various body locations considered. This would provide a more definite indication of the dependence of the accuracy of the present radiation calculations on the thermodynamic and radiative property data utilized.

7. 3 EFFECTS OF THERMODYNAMIC AND RADIATION PROPERTIES ON EQUILIBRIUM RADIATIVE HEAT TRANSFER*

In calculating radiative heat transfer to a vehicle entering a planetary atmosphere, use is made of the equilibrium composition and thermodynamic functions of the high temperature gas in the shock layer, together with the absorption coefficients describing the radiative processes of the molecular and atomic species in the gas. Assuming that these specific radiative properties are known, the total transfer of radiative energy depends on the accurate knowledge of the particle density of the elements which contribute to the total emissivity. The equilibrium composition is normally calculated on the assumption of an ideal gas mixture in chemical equilibrium with the dissociation energy of the molecules present in the mixture being one of the input constants.

In flight through an atmosphere composed of CO_2 and N_2 in the 13,000-20,000 ft/sec velocity regime, CN molecules are one of the major

*Material provided by J. S. Gruszczunski.

sources of radiative energy. The dissociation energy of the CN radical has been studied by a number of investigators with a great deal of controversy in recent years. Gaydon (Reference 3.14) selected a value of D (CN) = 7.6 ev. as the most probable. Subsequently, a series of different type experiments (Reference 3.15, 3.16 and 3.17) was reported which agreed with each other among themselves but pointed to a value D (CN) = 8.35 ev. This was further confirmed (Reference 3.20) in an electron impact experiment. More recent spectroscopic studies (Reference 3.18 and 3.19) of the CN molecule tend to support a value of D (CN) = 8.2 ev. Following this, Knight and Rink (Reference 3.22), using a shock tube and X-ray densitometer, and Berkowitz (Reference 3.23) employing a Knudsen cell and mass spectrometer arrived at a value close to D (CN) = 7.5 ev. This uncertainty in the dissociation energy between 7.52 and 8.4 ev., although having negligible effect on thermodynamic properties of the gas, affects very strongly the particle density of CN. This is illustrated in Figure 7-1. The present study utilized a dissociation value of 7.52. However, since the stagnation region temperatures were approximately 5700°K, the particle density of CN can vary within a factor of 5 depending on the dissociation energy value used.

Experimental studies of CN band system radiation (Reference 7.1, 7.2 and 7.3) depended on the assumption of particle concentration of CN molecules in the evaluation of the radiative constants. In order for these

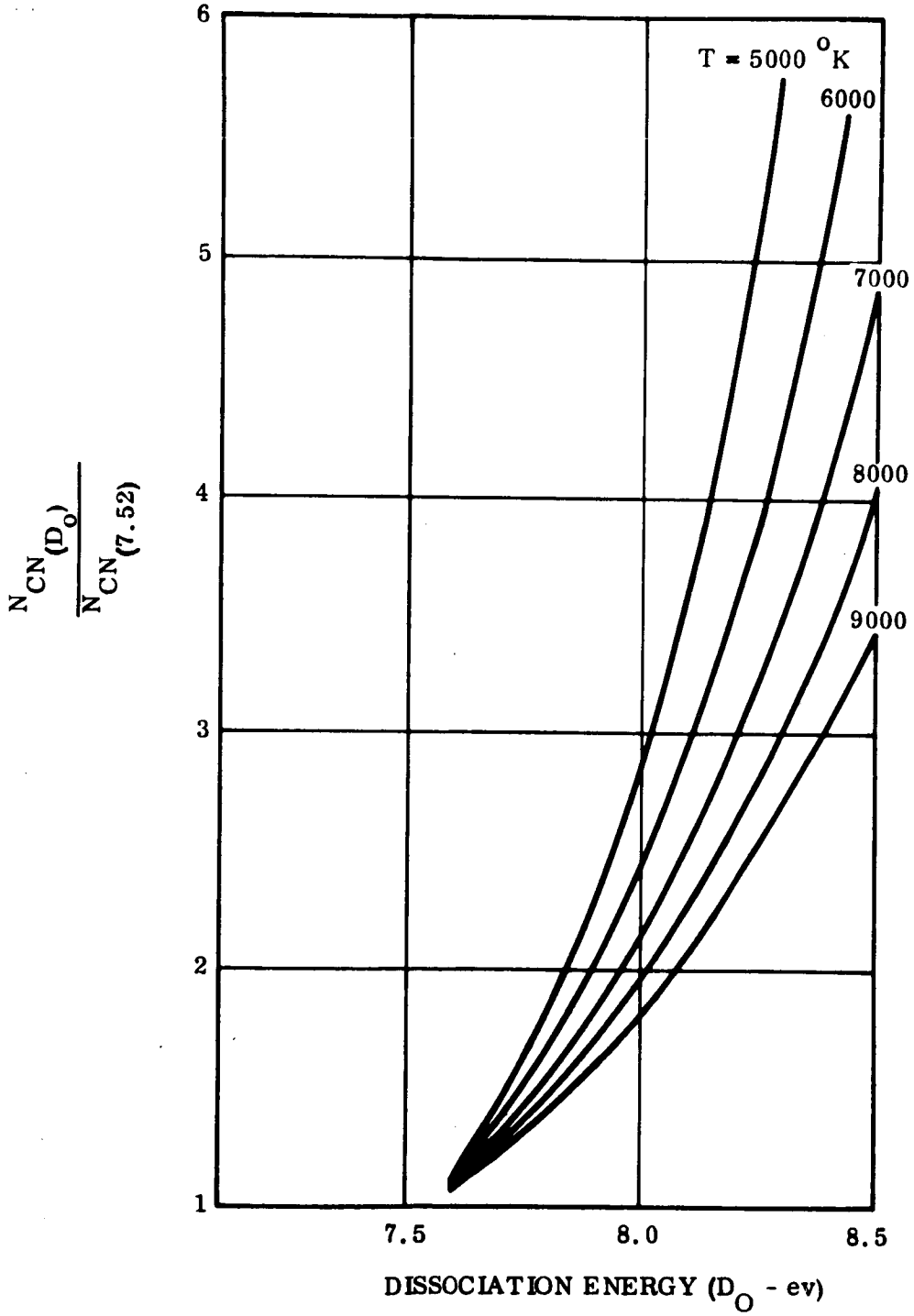

Figure 7-1 Effect of Dissociation of CN on Particle Density

results to agree with the oscillator strength measurements of Bennett and Dalby (Reference 3.59), Reis (Reference 7.2) had to assume D (CN) = 8.4 ev while Fairbairn and Kudrayavtsev had to assume D (CN) = 7.6 ev. If Reis has used D (CN) = 7.5 ev in correlating has experimental results, his f-number would be 0.094. As a result of this, Arnold and Reis (Reference 7.4) have used D (CN) = 8.2 ev and the f-number of 0.02. Some recent experimental data of total radiance of several CO_2 - N_2 gas mixtures (Reference 2.15) also show pronounced disagreement with theoretical predictions which are based on D_o = 7.52 ev. This summary indicates that there exists a large uncertainty in the properties of the CN radical which can have a significant influence on the predicted radiation level.

With the possibility of planetary atmospheres containing large mole fractions of CO_2, radiance of CO molecules must be considered in the total radiative transfer. On the basis of theoretical considerations, it appears that the CO (4+) system can be an important source of radiation in the vacuum ultraviolet part of the spectrum. The results of such calculations, shown previously in Figure 2-2, indicate that in the case of a 60% CO_2 - 40% N_2 atmosphere gas, a CO (4+) system can represent up to 80% of total radiation. Here again the calculations depend on the f-number, for which two values have been reported. One of these, f = 0.148, was obtained from measurements of photon scattering

(Reference 3.57) and the other, $f = 0.25$, from electron collision spectrum (Reference 7.5). In both cases the observed transition involved the ground state of the molecule. In the radiative transfer problem, the emission takes place in transitions to higher vibration levels of the ground electronic state, for which the electronic oscillator strength may be different from the values reported. In any case, these values do not agree with each other and hence introduce considerable uncertainty in the radiation predictions. This should be resolved by determining the radiative properties of CO (4+) at temperatures consistent with those encountered in the shock layer.

Therefore, the effect on the radiation of alternate (extreme) values in the f-numbers and the dissociation energy of CN could be evaluated by making additional calculations. This would establish bounding values for the equilibrium radiation for the cases studied.

7.4 EFFECTS OF CHEMICAL NONEQUILIBRIUM

In chemical nonequilibrium flows, the flow field can be computed as before, with consideration being given to finite chemical reaction rates and the dependence of the radiance on the chemical composition. With many of the excitation and reaction rates known, at best, only approximately, it is clear that the prediction of nonequilibrium radiation is less amenable to theoretical treatment than the equilibrium radiation.

The extent of the nonequilibrium shock layer can be estimated from the experimental data of Reference 2.15. The thickness of the nonequilibrium layer is defined to be $\Delta = V_s t$ where t is the time for the nonequilibrium radiant intensity to reach a level 10 percent above the equilibrium value. The experimentally determined nonequilibrium shock front thicknesses for several gas mixtures are shown in Figure 7-2 (Reference 2.15). For the hyperbolic encounter, $tp_\infty \approx 5 \times 10^{-3}$ micro-sec-atm; therefore, the thickness of the nonequilibrium layer, Δ, is estimated to be approximately 0.75 feet. As the equilibrium, uncoupled shock standoff distance for the sphere cap is 0.72 feet, the shock layers for all configurations will be predominantly in nonequilibrium. This indicates that the nonequilibrium nature of the flow is of major importance from the standpoint of the flow field. From Figure 7-3 total nonequilibrium radiation for a thickness Δ is approximately 12 watts/cm^2 at 20,000 fps, although the uncertainty in the data could make this value as high as 20 or as low as 6. An estimate of the corresponding equilibrium radiation taken from Figure 7.4 (Reference 2.15) is on the order of 8 watts/cm^2. Therefore, the nonequilibrium radiation based on these estimates does not appear to pose a serious problem. This does not, however, take into consideration the fact that the nonequilibrium zone is truncated for the sphere cone shape due to its

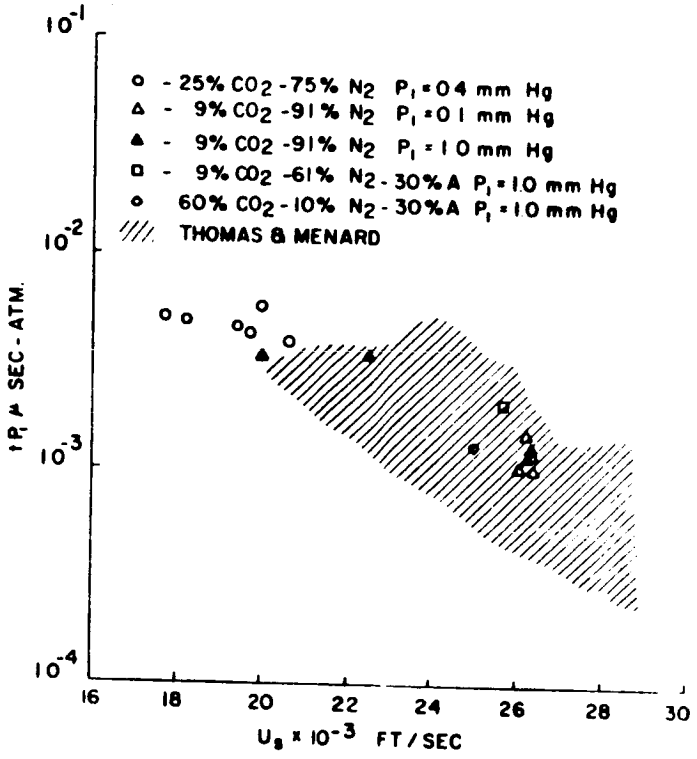

Figure 7 - 2 Nonequilibrium Shock Front Thickness for Several Gas Mixtures

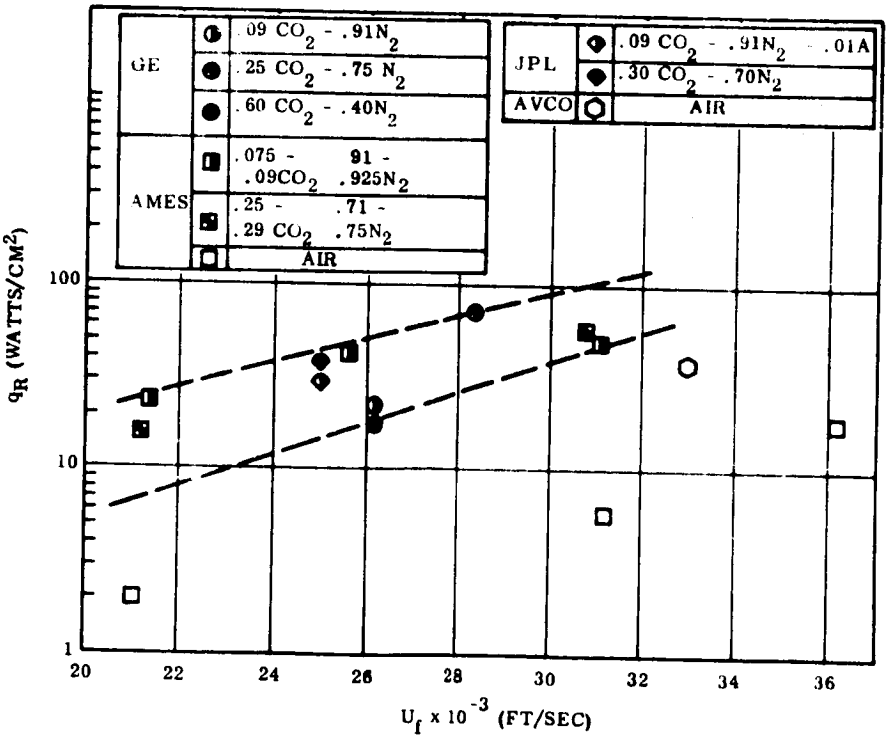

Figure 7 - 3 Comparison of Total Nonequilibrium Radiance for Several Gas Mixtures

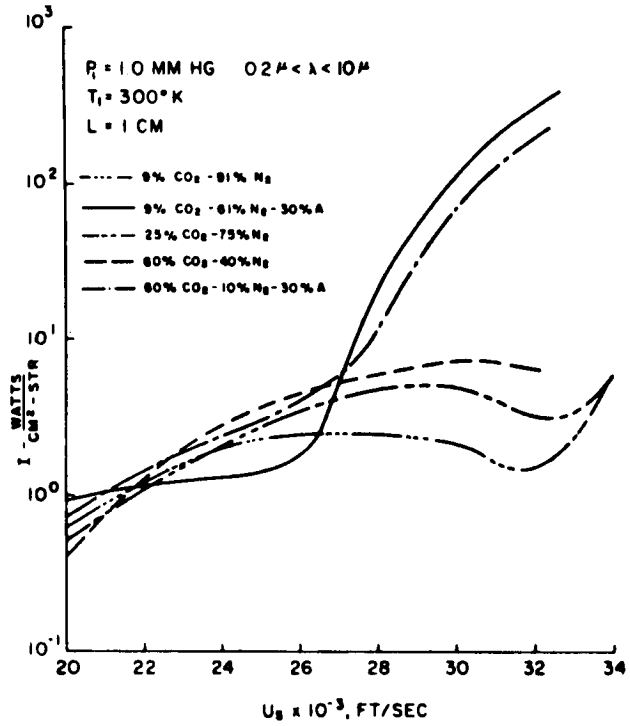

Figure 7-4 Radiance of Shock Layer for Several Gas Mixtures

smaller shock standoff distance. The average ratio of the peak nonequilibrium to equilibrium radiance, as estimated from Figure 15 of Reference 2.16, is on the order of 3 to 4. Thus, even in the case where the nonequilibrium zone is truncated, the radiation does not appear to increase drastically. However, in view of the uncertainties in the properties of the CN radical and CO (4+), and lack of experimental data in the vacuum UV of the spectrum, there is a large uncertainty in the engineering predictions of the total radiative heating.

A study of nonequilibrium flow is recommended as a follow-on effort to the work being proposed in this document. Such a study would be even more meaningful if the flow field methods utilized in the non-equilibrium study were essentially the same as utilized in the present equilibrium study. This is the case with both the inviscid and viscous non-equilibrium flow methods utilized at GE-RSD.

Section 8

REFERENCES

2.1 Goldberg, L. and Scala, S. M., "Mass Transfer in the Hypersonic Low Reynolds Number Viscous Layer", IAS Preprint 62-80, Presented at the IAS Thirtieth Annual Meeting, New York City, January 22, 1962.

2.2 Goldberg, L. and Scala, S. M., "Mass Transfer in the Low Reynolds Number Viscous Layer Around the Forward Region of a Hypersonic Vehicle, General Electric Company, MSD. TIS R65SD27, 1965.

2.3 Hoshizaki, H., "Shock-Generated Vorticity Effects at Low Reynolds Numbers", Lockheed Missiles and Space Division, LMSD 48481, Vol. 1, pp. 9-43, Jan. 1959.

2.4 Oguchi, H., "Blunt Body Viscous Layer With and Without a Magnetic Field", Phys. of Fluids, Vol. 3, pp. 567-580, 1960.

2.5 Hoshizaki, H., Neice, S. and Chan, K. K., "Stagnation Point Heat Transfer Rates at Low Reynolds Numbers", IAS Preprint 60-68, Presented at IAS Nat. Sum. Meet., June 28-July 1, 1960.

2.6 Ho, H. T. and Probstein, R. F., "The Compressible Viscous Layer in Rarefied Hypersonic Flow", Brown University, ARL TN 60-132, Aug. 1960. Also published in Proceedings of the Second Rarefied Gas Dynamics Symposium, Academic Press, pp. 525-552, 1960.

2.7 Ferri, A., Zakkay, V. and Ting, L., "Blunt Body Heat Transfer at Hypersonic Speeds and Low Reynolds Numbers", J. Aero. Sci., Vol. 28, pp. 962-971, 1961.

2.8 Probstein, R. F. and Kemp, N. H., "Viscous Aerodynamic Characteristics in Hypersonic Rarefied Gas Flow", J. Aero. Sci., Vol. 27, pp. 174-192, 218, 1960.

2.9 Levinsky, E. S. and Yoshihara, H., "Rarefied Hypersonic Flow Over a Sphere", Presented at the ARS International Hypersonics Conference, MIT, Cambridge, Massachusetts, 1961.

2.10 Cheng, H. K., "Hypersonic Shock-Layer Theory of the Stagnation Region at Low Reynolds Number", Proceedings of the 1961 Heat Transfer and Fluid Mechanics Institute, Stanford University Press, Stanford, California, 1962.

2.11 Kao, H. C., "Hypersonic Viscous Flow Near the Stagnation Streamline of a Blunt Body: II. Third-Order Boundary-Layer Theory and Comparison with Other Methods", AIAA Jour., Vol. 2, pp. 1897-1906, 1964.

2.12 Goldberg, L., "The Structure of the Viscous Hypersonic Shock Layer", General Electric Company MSD R65SD50, Sept. 1965.

2.13 Cheng, H. K., "The Blunt-Body Problem in Hypersonic Flow at Low Reynolds Number", Cornell Aeronautical Laboratory, CAL Report No. AF-1285-A-10, June 1963.

2.14 Willis, D. R., "Methods of Analysis of Nearly Free Molecule Flow for a Satellite or Other Space Vehicle", General Electric Co., MSVD, TIS R60SD399.

2.15 Gruszczynski, J. S. and Thomas, K. M., "Equilibrium and Non-Equilibrium Radiation in Simulated Planetary Atmospheres", AIAA Plasmadynamics Conference. Paper No. 66-183, March 1966.

2.16 Thomas, G. M. and Menard, W. A., "Experimental Measurements of Nonequilibrium and Equilibrium Radiation from Planetary Atmospheres", AIAA Entry Tech. Conf., Williamsburg, Va., Oct. 1964.

2.17 Goulard, R., "Preliminary Estimates of Radiative Transfer Effects on Detached Shock Layers," AIAA J. Volume 2, No. 3, March 1964.

2.18 Gruszczynski, J. S. and Warren, W. R., "Study of Equilibrium Air Total Radiation", AIAA Journal, pg. 517, April 1967.

2.19 Biberman, L. M., Vorobov, V. S., Norman, G. E., and Iakubov, I. T., "Radiation Heating in Hypersonic Flow", Kosmich Issled 2, 1964.

2. 20 Wilson, K. H. and Hoshizaki, H., "Inviscid, Non-Adiabatic Flow About Blunt Bodies", AIAA Journal, 3, 1965.

2. 21 Howe, J. T. and Viegas, J. R., "Solutions of the Ionized, Radiating Shock Layer, Including Reabsorption and Foreign Species Effects, and Stagnation Region Heat Transfer", NASA Ames Research Center TR R-159,1963.

2. 22 Xerikos, J. and Anderson, W., "A Critical Study of the Direct Blunt Body Integral Method", Douglas Aircraft Company, Report SM-42603, December 1962.

2. 23 Not used.

2. 24 Brunner, M., Dohner, C. V. Langelo, V. A., and Rie, H., "Flow Field Prediction and Analysis - Project Fire", G. E. TIS 64SD727, May 1964.

2. 25 Kyriss, C. L. and Rie, H., "Theoretical Investigation of the Static and Dynamic Stability of Entry Vehicles in the Mars Atmosphere", Proceedings of the AIAA/AAS Stepping Stones to Mars Meeting, Baltimore, March 1966.

3.1 Browne, W. G., "Thermodynamic Properties of Some Atoms and Atomic Ions", General Electric Co. (MSD) Engineering Physics Technical Memo No. 2, (no date).

3.2 Browne, W. G., Thermodynamic Properties of Some Diatoms and Diatomic Ions", General Electric Co. (MSD) Advanced Aerospace Physics Technical Memorandum No. 8, May 14, 1962.

3.3 Browne, W. G., "Thermodynamic Properties of Some Diatomic and Linear Polyatomic Molecules", General Electric Co. (MSD) Engineering Physics Technical Memo No. 3, (no date).

3.4 Browne, W. G., "Thermodynamic Properties of the Species CN, C_2, C_3, C_2N_2, and C^-", General Electric Co. (MSD) Advanced Aerospace Physics Technical Memorandum No. 9, May 14, 1962.

3.5 Browne, W. G., "Comparison of Thermal Functions Generated for Species in the High Temperature Air System with Literature Values", General Electric Co. (MSD) Advanced Aerospace Physics Technical Memo No. 10, May 14, 1962.

3.6 Moore, C. E., National Bureau of Standards, Circular No. 467, I (1949) and III (1958).

3.7 Gilmore, F. F., "Equilibrium Composition and Thermodynamic Properties of Air to 24000°K", Rand Corporation Project RM-1543, August 24, 1955.

3.8 Hogness, T. and Tsai, J., J. Am. Chem, Soc., 54, 123 (1932).

3.9 Kistiakowsky, G. and Gerschinowitz, H., J. Chem. Phys., 1, 433 (1933).

3.10 Robertson, C. and Pease, R., J. Chem. Phys., 10, 490 (1942).

3.11 White, J., J. Chem. Phys., 8, 502 (1940).

3.12 Glockler, G., J. Chem. Phys. 16, 1600 (1948).

3.13 Long, L. G., Proc. Royal Society, A198, 63 (1949).

3.14 Gaydon, A. G.: Dissociation Energies, Dover Publications, New York, 1950.

3.15 Stevenson, D. P., J. Chem. Phys. 18, 1347, 1950.

3.16 Brewer, L., Templeton, L. K. and Jenkins, F. A., J. Am. Chem. Soc. 73, 1462 (1951).

3.17 McDowell, C. A. and Warren, N. J., Trans. Faraday Soc. 48, 1084 (1952).

3.18 Douglas, A. E. and Routly, P. M., Astrophys. J. Suppl. Ser. 1, 295 (1954).

3.19 Carroll, P. K., Can. J. Phys. 34, 83 (1956).

3.20 Herron, J. T. and Dibeler, V. H., J. Am. Chem. Soc. 82, 1555 (1960).

3. 21 Dibeler, V. H., Reese, R. M., and Franklin, J. L., J. Am. Chem. Soc., 83, 1813 (1961).

3. 22 Knight, H. T. and Rink, J. P.: "Dissociation Energy of Cyanogen and Related Quantities by X-ray Densitometry of Shock Waves," J. Chem. Phys., July 1961.

3. 23 Berkowitz, J.: "Heat of Formation of the CN Radical", J. of Chem. Phys. Vol. 36, No. 10, May 1962.

3. 24 Tsang, W., Bauer, S., and Cowperthwaite, M.: "Dissociation Energy and Rate of Decomposition of C_2N_2," J. Chem. Phys. 36, 1768 (1962).

3. 25 Brinkley, S. R., Jr. and Lewis, B., "The Thermodynamics of Combustion Gases; General Considerations", U. S. Bureau of Mines Report of Investigations 4806 - April 1952.

3. 26 Browne, W. G. and Smookler, G., "Thermodynamic Properties of the Planetary Atmosphere ($70\%N_2$ - $30\%CO_2$)", GE-RSD Aerospace Physics Laboratory Technical Memorandum No. 8125-40, Feb. 1967.

3. 27 Hirschfelder, J. O., Curtiss, C. F. and Bird, R. F., "Molecular Theory of Gases and Liquids", Wiley, N. Y., 1954.

3.28 Hirschfelder, J. O., "Heat Conductivity in Polyatomic, Electronically Excited, or Chemically Reacting Mixtures III", Sixth (Int.) Combustion Symposium, Reinhold Publ. Corp. N. Y., 1957, pp. 351-366.

3.29 Westenberg, A. A. and deHaas, N., "Gas Thermal Conductivity Studies at High Temperatures. Line Source Technique and Results in N_2, CO_2 and N_2-CO_2 Mixtures", Phys. Flu., 5, 266, (1962).

3.30 Yun, K. S. and Mason, E. A., "Collision Integral for the Transport Properties of Dissociating Air at High Temperatures", Physics of Fluids, 5, (1962).

3.31 Westenberg, A. A. and deHaas, N., "Gas Thermal Conductivity Studies II. Results for O_2 and O_2-H_2O Mixtures", Phys. Flu., 6, 617, (1963).

3.32 Carnevale, E. H., Carey, C. A. and Larson, G. S., "Experimental Determination of the Transport Properties of Gases", Technical Report AFML-TR-65-141, 1965.

3.33 Amdur, D. and Schuler, L. M., "Diffusion Coefficients of the Systems CO-CO and CO-N_2," Journ. Chem. Phys., 38, 188, (1963).

3.34 Eucken, A., Physik, Z., 14, 324, (1913).

3.35 Gregory, H. and Archer, C. T., Proc. Roy. Soc. (London) (A), 121, 285 (1928).

3.36 Dickens, B. G., Proc. Roy. Soc. (London) (A), 143, 517 (1934).

3.37 Kannuluik, W. G. and Martin, H. L., Proc. Roy. Soc. (London) (A), 144, 496 (1934).

3.38 Johnston, H. L. and Grilly, E. R., Jour. Chem. Phys., 14, 233, (1946).

3.39 Pakurar, T. A. and Terron, J. R., "Self-Diffusion Coefficient of Carbon Dioxide", Jour. Chem. Phys., 43, 2917, (1965).

3.40 Svehla, R., "Viscosities and Thermal Conductivities of Gases at High Temperatures", Technical Report R-132 NASA.

3.41 Breene, Jr., R. G. and Nardone, M. C., "Radiant Emission from High Temperature Equilibrium Air", J. Quant. Spectrosc. Radiat. Transfer, Vol. 2, pp. 272-292, Pergamon Press, February 1962.

3.42 Gruszczynski, J. S. and Bradley, D. A., "Radiative Properties of High Temperature 30% CO_2 - 70%N_2 Gas Mixture", G. E. Space Sciences Laboratory Experimental Fluid Physics Technical Memorandum No. 203, April 1967.

3.43 Herzberg, G., "Molecular Spectra and Molecular Structure, Diatomic Molecules", Van Nostrand, New York, 1950.

3.44 Wurster, W. H., Measured Transition Probability for the first Positive Band System of Nitrogen", CAL Rept. QM 1626-A-3, January 1962.

3.45 Nicholls, R. W., Jarmain, W. R. and Fraser, P. A., Can. J. Phys. 31, 1019, 1953.

3.46 Goody, R. M., Quart. J. Roy. Met. Soc. 78, 165, 1952.

3.47 Bennett, R. G. and Dalby, F. W., J. Chem. Phys. 31, 434, 1959.

3.48 Turner, R. G. and Nicholls, R. W., Can. J. Phys. 32, 475, 1954.

3.49 Jarmain, W. R., Fraser, P. A. and Nicholls, R. W., Astrophys. J. 118, 228, 1953.

3.50 Bethke, G., J. Chem. Phys. 31, 669, 1959.

3.51 Fraser, P. A., Jarmain, W. R. and Nicholls, R. W., Astrophys. J. 119, 286, 1954.

3.52 Kivel, B., Mayer, H. and Bethe, H., Ann. Phys. 2, 57, 1957.

3.53 Clementi, E., Astro. J., 132, 898, (1950).

3.54 Nicholls, R. W., Fraser, P. A., Jarmain, W. R., Combustion and Flame, 3, 13, 1959.

3.55 Breene, R. G., unpublished data

3.56 Nicholls, R. W., Fraser, P. A., Jarmain, W. R., McEachran, R. P., Astro. J. 13, 399, 1960.

3.57 Hexter, R. M., "Evaluation of Lattice Sums in the Calculation of Crystal Spectra", Journal of Chemical Physics, Vol. 37, No. 6, Sept. 1962.

3.58 Nicholls, R. W., "Laboratory Astrophysics", J. Quant, Spectrosc. Radiat. Transfer, Vol. 2, pp. 433-439, Pergamon Press.

3.59 Bennett, R. G. and Dalby, F. W., J. Chem. Phys., 1962.

3.60 Branscomb, L. M., Burch, D. S., Smith, S. J. and Geltman, S., Phys. Rev. 111, 504, 1958.

3.61 Seman, M. L. and Branscomb, L. M., Phys. Review 125, 1602, 1962.

4.1 Gravalos, F. G., "Supersonic Flow About Blunt Bodies of Revolution," Proc. of IV Annual Meeting of the American Astronautical Society, New York, January 1958.

4.2 Gravalos, F. G., Edelfelt, I. H. and Emmons, H. W., "The Supersonic Flow About a Blunt Body of Revolution for Gases at Chemical Equilibrium", Proceedings of the 9th Annual Congress of the International Astronautical Federation, Amsterdam 1958. (Also published as GE TIS R58SD245.)

4.3 Kyriss, C. L. and Townsend, P. C., "Thermodynamic Properties for Calculating Equilibrium Flow Fields in Planetary Atmospheres", GE-RSD Aerodynamics Technology Component Data Memo No. 67-17, April 1967.

4.4 Not used.

4.5 Flugge-Lotz, I. and Blottner, F. G., "Computation of the Compressible Laminar Boundary Layer Flow Including Displacement Thickness Interaction Using Finite Difference Methods", Stanford University Div. of Eng. Mech. Tech. Rep. No. 131, January 1962.

4.6 Blottner, F. G., "Non-Equilibrium Laminar Boundary Layer Flow of Ionized Air", G.E. TIS Report R64SD56, November 1964.

4.7 Schlichting, H., "Boundary Layer Theory", McGraw-Hill Book Co., 1955.

4.8 Chandrasekhar, S., "Radiative Transfer", Oxford at the Clarendon Press, 1950.

4.9 Zhiguler, Romishevskii, and Vertushkin", Role of Radiation in Modern Gasdynamics", AIAA Journal Vol. I, No. 6, June 1963.

4.10 Dohner, C. V., "Hot Gas Radiation Program Procedure", GE-MSD Report No. PIR-HTT-8151-081, March 1963.

4.11 Goodman, M. Y., "Fire Flow Field Hot Gas Radiation Program", GE-MSD Report E. I. and P. Memo No. 1026, December 1964.

4.12 Levine, J. N., "Finite Difference Solution of the Laminar Boundary Layer Equations Including the Effects of Transverse Curvature, Vorticity and Displacement Thickness", General Electric Co., MSD TIS 66SD349, December 1966.

5.1 Krumins, M. V., "A Ballistics Range Study of Aerodynamic Characteristics of Mars Probe/Lander Shapes", AIAA Paper 67-167, 5th Aerospace Sciences Meeting, January 1967.

5.2 Ridyard, H. W. and Storer, E. M., "Stagnation Point Shock Detachment of Blunt Bodies in Supersonic Flow", J. Aerospace Sciences, 29, 1962.

5.3 Li, T. Y. and Geiger, R. E., "Stagnation Point of a Blunt Body in Hypersonic Flow", J. Aero. Sci., Vol. 24, pp. 25-32, 1957.

5.4 Hayes, W. D. and Probstein, R. F., "Hypersonic Flow Theory", Academic Press, New York, 1959.

5.5 Serbin, H., "Supersonic Flow Around Blunt Bodies", J. Aerospace Sciences", January 1958.

5.6 Linnell, R. D., "Hypersonic Flow Around a Sphere", J. Aerospace Sciences", January 1958.

5.7 Not used.

5.8 Hearne, L. F., Chin, J. H., and Lefferdo, J. M., "Re-Entry Heating and Thermal Protection of a Mars-Mission Earth-Re-Entry Module", AIAA Entry Technology Conference, Williamsburg and Hampton, October 1964.

5.9 Fay, J. A. and Riddell, F. R., "Theory of Stagnation Point Heat Transfer in Dissociated Air", J. Aero. Sci., Vol. 25, pp. 78-85, 1958.

5.10 Hoshizaki, H., "Heat Transfer in Planetary Atmospheres at Super-Satellite Speeds", ARS Journal, October 1962.

5.11 Scala, S. M. and Gilbert, L. M., "Theory of Hypersonic Laminar Stagnation Region Heat Transfer in Dissociating Gases", General Electric Co., MSD, TIS R63SD40, April 1963. To be published in Developments in Mechanics, Ed. -S. Ostrach, Pergamon Press.

7.1 Fairbairn, A., "The Spectrum of Shock-Heated Gases Simulating the Venus Atmosphere", AIAA Conference on Physics of Entry Into Planetary Atmospheres, Cambridge, Mass., August 26-28, 1963.

7.2 Reis, V. H., "Oscillator Strength of the CN Violet System", J. Quant. Spectosc. Radiat. Transfer, Vol. 5, pp. 585-594, Pergamon Press, 1965.

7.3 Kudryavtsev, E. M., Gippius, E. F., Derbeneva, S. S., Pechenov, A. N. and Sobolev, N. N., "Determination of the Matrix Element of the Dipole Moment of the Electronic Transition of the Violet Band System of Cyanogen", translated from Teplofizika Vysokikh Temperatur, Vol. 1, No. 3, pp. 376-385, Nov.-Dec., 1963.

7.4 Arnold, J. O., Reis, V. H. and Woodward, H. T., "Studies of Shock-Layer Radiation of Bodies Entering Planetary Atmospheres", AIAA Journal, Vol. 3, No. 11, November, 1965.

7.5 Meyer, V. C., Skerbele, A., Lassettre, E. N., "Intensity Distribution in the Electron-Impact Spectrum of Carbon Monoxide of High-Resolution and Small Scattering Angles", Jour. Chem. Phys. 43, 805-816, August 1, 1965.

Section 9

TABLES OF INVISCID SHOCK LAYER PROPERTIES

Inviscid, equilibrium flow shock layer properties for the sphere cone and sphere cap configurations are given in Tables 9.1 through 9.4, for the hyperbolic entry and ballistic range flight conditions. Included in the tables for each case are the state and motion variable profiles along lines of constant radius through the shock layer. The first point along each line begins with the shock wave, and the profile terminates with the body, where the body and the line intersect. The coordinates of the stagnation point are (0, 0).

TABLE 9.1

SPHERE-CONE SHOCK LAYER PROPERTIES - HYPERBOLIC ENTRY

X/RB	R/RB	P PSF	RHO SLUGS/FT**3	T DEG.R	V FPS	M	S/R
-.01000	0.	.35964E+3	.15492E-4	10299.	1265.	.246	45.455
-.00700	0.	.36726E+3	.15780E-4	10320.	791.	.154	45.455
-.00400	0.	.37095E+3	.15919E-4	10330.	400.	.078	45.455
0.	0.	.37222E+3	.15967E-4	10334.	0.	0.	45.455
-.00898	.023	.35337E+3	.15318E-4	10264.	2278.	.445	45.373
-.00590	.023	.36038E+3	.15562E-4	10289.	1814.	.353	45.402
-.00283	.023	.36364E+3	.15665E-4	10304.	1418.	.276	45.428
.00127	.023	.36462E+3	.15680E-4	10313.	980.	.191	45.455
-.00435	.050	.34425E+3	.15236E-4	10169.	4195.	.830	45.021
-.00107	.050	.33891E+3	.14887E-4	10187.	3524.	.695	45.207
.00329	.050	.33713E+3	.14700E-4	10217.	2742.	.538	45.366
.00652	.050	.33592E+3	.14587E-4	10234.	2171.	.425	45.456
.00230	.075	.32416E+3	.14882E-4	9987.	6205.	1.254	44.402
.00628	.075	.30935E+3	.13950E-4	10040.	5148.	1.031	44.887
.01092	.075	.30643E+3	.13592E-4	10104.	3970.	.788	45.243
.01473	.075	.30352E+3	.13334E-4	10141.	3064.	.606	45.456
.01209	.100	.25930E+3	.14361E-4	9682.	8282.	1.721	43.685
.01701	.100	.29343E+3	.13612E-4	9902.	6518.	1.325	44.414
.02149	.100	.29074E+3	.13123E-4	10013.	5058.	1.014	45.008
.02679	.100	.28855E+3	.12747E-4	10098.	3420.	.679	45.456
.06304	.200	.28317E+3	.14151E-4	9529.	9015.	1.896	43.381
.06774	.200	.28461E+3	.14214E-4	9483.	9004.	1.893	43.381
.07712	.200	.28805E+3	.14051E-4	9621.	8349.	1.737	43.682
.07991	.200	.28843E+3	.13348E-4	9905.	6376.	1.295	45.506
.08453	.200	.28855E+3	.12747E-4	10098.	3420.	.679	45.456
.21081	.500	.28937E+3	.14253E-4	9611.	8647.	1.807	43.546
.23881	.500	.29402E+3	.14462E-4	9621.	8619.	1.800	43.540
.25257	.500	.29487E+3	.14664E-4	9562.	8923.	1.872	43.382
.25773	.500	.29492E+3	.12997E-4	10116.	3272.	.648	45.460
.40471	.900	.28966E+3	.14258E-4	9615.	8630.	1.803	43.553
.46323	.900	.29457E+3	.14479E-4	9625.	8601.	1.795	43.547
.47415	.900	.29492E+3	.14510E-4	9620.	8629.	1.802	43.532
.48142	.900	.29507E+3	.14646E-4	9573.	8872.	1.860	43.410
.48867	.900	.29510E+3	.13004E-4	10117.	3268.	.647	45.460
.42893	.950	.28963E+3	.14257E-4	9614.	8631.	1.803	43.553
.49213	.950	.29474E+3	.14487E-4	9625.	8600.	1.795	43.546
.50826	.950	.27285E+3	.13552E-4	9556.	8826.	1.851	43.524
.51754	.950	.24563E+3	.11036E-4	9968.	4350.	.872	45.460

TABLE 9.1 CONT.

X/RB	R/RB	P PSF	RHO SLUGS/FT**3	T DEG.R	V FPS	M	S/R
.45315	1.000	.28961E+3	.14257E-4	9614.	8633.	1.803	43.552
.49440	1.000	.29342E+3	.14423E-4	9624.	8599.	1.795	43.552
.53808	1.000	.17139E+3	.89769E-5	9197.	9813.	2.110	43.532
.56329	1.000	.81682E+2	.46991E-5	8537.	11122.	2.491	43.519
.50179	1.100	.28305E+3	.14145E-4	9529.	9021.	1.897	43.383
.52440	1.100	.24754E+3	.12406E-4	9492.	8992.	1.895	43.552
.58349	1.100	.13516E+3	.72705E-5	9005.	10240.	2.228	43.551
.62955	1.100	.80315E+2	.46082E-5	8552.	11126.	2.490	43.547
.53018	1.150	.25600E+3	.13723E-4	9106.	10478.	2.270	42.500
.54954	1.150	.22106E+3	.11234E-4	9399.	9265.	1.964	43.541
.63367	1.150	.10498E+3	.58220E-5	8785.	10675.	2.354	43.552
.69443	1.150	.63763E+2	.37685E-5	8354.	11492.	2.605	43.547
.56479	1.200	.22551E+3	.13435E-4	8406.	11924.	2.691	41.570
.59602	1.200	.17419E+3	.91060E-5	9210.	9780.	2.101	43.532
.69896	1.200	.82668E+2	.47235E-5	8580.	11071.	2.474	43.552
.60619	1.250	.19680E+3	.13749E-4	7344.	13174.	3.176	40.500
.61813	1.250	.17953E+3	.12207E-4	7642.	12214.	2.929	41.295
.64993	1.250	.13976E+3	.79060E-5	8704.	10976.	2.437	42.907
.69110	1.250	.10734E+3	.59360E-5	8805.	10636.	2.343	43.553
.73535	1.250	.82958E+2	.47375E-5	8583.	11064.	2.472	43.553

TABLE 9.2

SPHERE-CONE SHOCK LAYER PROPERTIES - BALLISTIC ENTRY

X/RB	R/RB	P PSF	RHO SLUGS/FT**3	T DEG.R	V FPS	M	S/R
—.01350	0.	.11459E+6	.58683E-2	10174.	1346.	.276	34.677
—.00945	0.	.11786E+6	.60053E-2	10227.	844.	.173	34.677
—.00540	0.	.11946E+6	.60719E-2	10249.	428.	.087	34.677
0.	0.	.12001E+6	.60952E-2	10256.	0.	0.	34.677
—.01215	.025	.11332E+6	.58773E-2	10073.	2159.	.445	34.607
—.00804	.025	.11623E+6	.59781E-2	10146.	1678.	.345	34.632
—.00392	.025	.11756E+6	.60140E-2	10193.	1271.	.260	34.654
.00157	.025	.11785E+6	.60050E-2	10226.	845.	.173	34.677
—.00860	.050	.10939E+6	.58979E-2	9746.	3631.	.762	34.393
—.00630	.050	.10927E+6	.58513E-2	9803.	3423.	.717	34.440
—.00175	.050	.10923E+6	.57697E-2	9918.	2957.	.615	34.532
.00242	.050	.10878E+6	.56794E-2	10013.	2470.	.511	34.612
.00635	.050	.10841E+6	.56040E-2	10094.	1985.	.409	34.680
—.00112	.075	.10306E+6	.59406E-2	9223.	5202.	1.126	34.026
.00166	.075	.10166E+6	.57555E-2	9360.	4825.	1.036	34.158
.00439	.075	.10072E+6	.55977E-2	9504.	4406.	.938	34.290
.01068	.075	.09957E+6	.53284E-2	9801.	3382.	.709	34.555
.01460	.075	.09852E+6	.51813E-2	9941.	2761.	.574	34.680
.00887	.100	.94503E+5	.59730E-2	8570.	6759.	1.538	33.495
.01229	.100	.94986E+5	.57583E-2	8852.	6092.	1.355	33.792
.01570	.100	.94446E+5	.55030E-2	9134.	5379.	1.171	34.061
.01911	.100	.93928E+5	.52876E-2	9396.	4681.	1.004	34.290
.02386	.100	.93319E+5	.50529E-2	9700.	3722.	.784	34.555
.02679	.100	.93000E+5	.49413E-2	9851.	3134.	.655	34.680
.05984	.200	.91038E+5	.59735E-2	8323.	7295.	1.694	33.282
.07602	.200	.92818E+5	.58559E-2	8583.	6725.	1.528	33.531
.07802	.200	.92917E+5	.55563E-2	8942.	5848.	1.290	33.917
.07967	.200	.92962E+5	.53511E-2	9225.	5139.	1.113	34.158
.08191	.200	.92992E+5	.51278E-2	9555.	4202.	.893	34.440
.08453	.200	.93000E+5	.49418E-2	9851.	3134.	.655	34.680
.20007	.500	.94703E+5	.59754E-2	8581.	6728.	1.530	33.504
.21528	.500	.95707E+5	.60310E-2	8590.	6718.	1.526	33.499
.23634	.500	.96553E+5	.60566E-2	8623.	6648.	1.507	33.521
.24446	.500	.96737E+5	.62617E-2	8419.	7117.	1.641	33.301
.25206	.500	.96839E+5	.62834E-2	8404.	7152.	1.651	33.283
.25565	.500	.96855E+5	.55243E-2	9292.	4958.	1.069	34.173
.25773	.500	.96856E+5	.51095E-2	9915.	2878.	.599	34.680

TABLE 9.2 CONT.

X/RB	R/RB	P PSF	RHO SLUGS/FT**3	T DEG.R	V FPS	M	S/R
.38472	.900	.94705E+5	.59754E-2	8581.	6728.	1.529	33.504
.43276	.900	.96211E+5	.60551E-2	8600.	6698.	1.521	33.502
.47067	.900	.96731E+5	.60899E-2	8599.	6705.	1.523	33.493
.47958	.900	.96783E+5	.62159E-2	8470.	7001.	1.608	33.354
.48765	.900	.96803E+5	.55218E-2	9291.	4960.	1.069	34.173
.48867	.900	.96790E+5	.51070E-2	9914.	2883.	.600	34.680
.40780	.950	.94681E+5	.59755E-2	8579.	6732.	1.531	33.503
.45516	.950	.96112E+5	.60485E-2	8600.	6697.	1.520	33.503
.49221	.950	.96710E+5	.60804E-2	8608.	6684.	1.517	33.502
.51021	.950	.86255E+5	.56786E-2	8294.	7322.	1.703	33.325
.51638	.950	.78397E+5	.46485E-2	8974.	5639.	1.241	33.173
.51754	.950	.79625E+5	.43498E-2	9611.	3948.	.837	34.680
.43089	1.000	.94670E+5	.59755E-2	8579.	6734.	1.531	33.502
.48405	1.000	.96215E+5	.60540E-2	8602.	6694.	1.520	33.503
.53222	1.000	.61108E+5	.41747E-2	8014.	7716.	1.830	33.496
.56454	1.000	.26928E+5	.21714E-2	7001.	9411.	2.454	33.285
.45399	1.050	.94657E+5	.59755E-2	8578.	6736.	1.532	33.501
.47731	1.050	.95451E+5	.60151E-2	8591.	6715.	1.526	33.503
.53970	1.050	.60726E+5	.41497E-2	8011.	7718.	1.831	33.502
.57555	1.050	.36395E+5	.27155E-2	7440.	8645.	2.155	33.504
.59584	1.050	.26910E+5	.21122E-2	7135.	9127.	2.345	33.494
.47717	1.100	.93629E+5	.59762E-2	8504.	6898.	1.578	33.438
.48985	1.100	.89259E+5	.56949E-2	8499.	6880.	1.573	33.501
.54813	1.100	.60250E+5	.41216E-2	8004.	7729.	1.835	33.504
.59839	1.100	.36087E+5	.26970E-2	7430.	8662.	2.161	33.502
.61725	1.100	.29664E+5	.22896E-2	7234.	8974.	2.282	33.503
.62739	1.100	.26672E+5	.20940E-2	7133.	9127.	2.345	33.503
.50376	1.150	.85265E+5	.59545E-2	7935.	8104.	1.948	32.908
.51600	1.150	.79614E+5	.52358E-2	8288.	7282.	1.693	33.432
.55750	1.150	.60832E+5	.41548E-2	8015.	7711.	1.829	33.503
.62204	1.150	.36237E+5	.27052E-2	7435.	8653.	2.158	33.503
.64647	1.150	.29736E+5	.22942E-2	7236.	8970.	2.281	33.503
.65970	1.150	.26714E+5	.20972E-2	7133.	9127.	2.345	33.502
.57473	1.250	.67680E+5	.57393E-2	6866.	10172.	2.721	31.658
.63108	1.250	.46578E+5	.34031E-2	7594.	8459.	2.084	35.350
.70788	1.250	.30484E+5	.23421E-2	7262.	8930.	2.264	33.504
.72738	1.250	.27434E+5	.21439E-2	7160.	9087.	2.328	33.504

TABLE 9.3

SPHERE-CAP SHOCK LAYER PROPERTIES - HYPERBOLIC ENTRY

X/DB	R/DB	P PSF	RHO SLUGS/FT**3	T DEG.R	V FPS	M	S/R
-.06	0.	.35964E+3	.15493E-4	10299.	1265.	.246	45.455
-.03	0.	.37024E+3	.15893E-4	10328.	498.	.097	45.455
0.	0.	.37222E+3	.15967E-4	10334.	0.	0.	45.455
-.05177	.150	.35534E+3	.15420E-4	10264.	2463.	.481	45.339
-.02118	.150	.36255E+3	.15642E-4	10296.	1709.	.333	45.405
.00941	.150	.36414E+3	.15662E-4	10312.	1011.	.197	45.455
-.03755	.250	.34864E+3	.15312E-4	10207.	3610.	.711	45.146
-.01747	.250	.34883E+3	.15233E-4	10226.	3066.	.602	45.259
.00581	.250	.34984E+3	.15182E-4	10254.	2374.	.464	45.374
.02633	.250	.34896E+3	.15086E-4	10270.	1731.	.338	45.456
-.01666	.350	.33882E+3	.15142E-4	10121.	4822.	.959	48.861
.00695	.350	.33588E+3	.14839E-4	10160.	3965.	.784	45.114
.02943	.350	.33481E+3	.14664E-4	10195.	3178.	.625	45.295
.05218	.350	.33264E+3	.14461E-4	10224.	2282.	.447	45.456
-.00337	.400	.33110E+3	.15007E-4	10051.	5593.	1.122	44.624
.02061	.400	.32660E+3	.14551E-4	10113.	4505.	.895	45.008
.04386	.400	.32332E+3	.14257E-4	10151.	3670.	.725	45.240
.06863	.400	.31916E+3	.13942E-4	10186.	2666.	.524	45.456
.01258	.450	.31873E+3	.14783E-4	9934.	6645.	1.350	44.221
.03195	.450	.31269E+3	.14144E-4	10030.	5359.	1.075	44.798
.05087	.450	.30897E+3	.13814E-4	10075.	4592.	.915	45.064
.07030	.450	.30402E+3	.13471E-4	10105.	3881.	.770	45.277
.08757	.450	.29916E+3	.13163E-4	10129.	3171.	.628	45.456
.03252	.500	.29721E+3	.14393E-4	9704.	8159.	1.692	43.729
.03626	.500	.28729E+3	.13634E-4	9787.	7443.	1.531	44.026
.04773	.500	.27824E+3	.12920E-4	9872.	6508.	1.325	44.504
.06403	.500	.26172E+3	.12011E-4	9894.	5854.	1.186	44.877
.08126	.500	.24055E+3	.11007E-4	9874.	5533.	1.121	45.114
.10913	.500	.20000E+3	.09182E-4	9807.	5289.	1.072	45.456
.05120	.550	.26665E+3	.13881E-4	9288.	9931.	2.125	42.884
.05789	.550	.25687E+3	.12867E-4	9500.	8985.	1.893	43.516
.06693	.550	.24316E+3	.11780E-4	9665.	7981.	1.658	44.080
.08738	.550	.22344E+3	.10541E-4	9778.	6919.	1.420	44.598
.09191	.550	.22357E+3	.10499E-4	9800.	6727.	1.377	44.665
.10559	.550	.17291E+3	.08265E-4	9671.	7102.	1.467	44.816
.12008	.550	.12080E+3	.05962E-4	9442.	7851.	1.648	44.917
.13485	.550	.08118E+3	.04163E-4	9185.	8664.	1.853	44.984

TABLE 9.3 CONT.

X/DB	R/DB	P PSF	RHO SLUGS/FT**3	T DEG.R	V FPS	M	S/R
.08329	.600	.23728E+3	.13502E-4	8715.	11384.	2.528	41.938
.08775	.600	.22980E+3	.12608E-4	8948.	10816.	2.366	42.383
.09443	.600	.22528E+3	.11843E-4	9209.	10033.	2.157	43.042
.11230	.600	.17090E+3	.08579E-4	9428.	8724.	1.844	44.125
.14526	.600	.10454E+3	.05343E-4	9245.	8804.	1.879	44.629
.16506	.600	.07874E+3	.04118E-4	9073.	9194.	1.984	44.742
.12176	.650	.20258E+3	.13589E-4	7580.	12921.	3.047	40.749
.13121	.650	.16985E+3	.10159E-4	8360.	11874.	2.689	41.943
.14388	.650	.13929E+3	.07934E-4	8661.	11134.	2.475	42.761
.16040	.650	.11146E+3	.06114E-4	8857.	10427.	2.291	43.613
.17133	.650	.09779E+3	.05295E-4	8911.	10148.	2.222	43.957
.19889	.650	.07271E+3	.03942E-4	8861.	10024.	2.199	44.367
.17199	.700	.15525E+3	.14271E-4	5811.	14777.	4.138	38.595
.17503	.700	.14750E+3	.12806E-4	6280.	14324.	3.917	39.183
.19266	.700	.11190E+3	.07525E-4	7577.	12774.	3.041	41.535
.20474	.700	.09627E+3	.06021E-4	8028.	12181.	2.807	42.354
.23510	.750	.12134E+3	.13379E-4	5178.	15938.	4.971	37.074
.23566	.750	.12042E+3	.13184E-4	5226.	15879.	4.933	37.167

TABLE 9.4

SPHERE-CAP SHOCK LAYER PROPERTIES - BALLISTIC ENTRY

X/DB	R/DB	P PSF	RHO SLUGS/FT**3	T DEG.R	V FPS	M	S/R
-.07650	0.	.11459E+6	.58683E-2	10174.	1346.	.276	34.677
-.03825	0.	.11905E+6	.60550E-2	10243.	563.	.115	34.677
0.	0.	.12001E+6	.60952E-2	10256.	0.	0.	34.677
-.06535	.175	.11284E+6	.58785E-2	10028.	2377.	.491	34.583
-.02626	.175	.11583E+6	.59594E-2	10143.	1699.	.349	34.634
.01283	.175	.11628E+6	.59392E-2	10205.	1113.	.228	34.677
-.04446	.300	.10989E+6	.58945E-2	9787.	3479.	.729	34.422
-.02179	.300	.10999E+6	.58249E-2	9898.	3054.	.636	34.508
.00579	.300	.11016E+6	.57573E-2	10006.	2537.	.525	34.590
.03810	.300	.10948E+6	.56502E-2	10110.	1895.	.390	34.680
-.01987	.400	.10585E+6	.59225E-2	9451.	4577.	.977	34.186
.00398	.400	.10469E+6	.57029E-2	9666.	3910.	.825	34.377
.02907	.400	.10386E+6	.55576E-2	9807.	3388.	.709	34.508
.05002	.400	.10296E+6	.54392E-2	9910.	2946.	.613	34.600
.06863	.400	.10200E+6	.53313E-2	9997.	2513.	.521	34.680
-.00392	.450	.10206E+6	.59461E-2	9143.	5408.	1.177	33.970
.01049	.450	.10065E+6	.56772E-2	9388.	4743.	1.017	34.193
.03553	.450	.99275E+5	.54449E-2	9605.	4079.	.864	34.396
.07229	.450	.96448E+5	.51551E-2	9807.	3337.	.699	34.600
.08757	.450	.95000E+5	.50289E-2	9884.	3003.	.626	34.680
.01602	.500	.95412E+5	.59720E-2	8635.	6611.	1.497	33.552
.02184	.500	.93021E+5	.56229E-2	8861.	6044.	1.343	33.841
.03332	.500	.90855E+5	.53127E-2	9091.	5452.	1.192	34.079
.06183	.500	.82661E+5	.46923E-2	9289.	4879.	1.056	34.377
.07454	.500	.77939E+5	.44117E-2	9299.	4822.	1.043	34.465
.09673	.500	.68242E+5	.38747E-2	9270.	4864.	1.054	34.600
.10913	.500	.62000E+5	.35409E-2	9238.	4954.	1.074	34.680
.03573	.550	.85894E+5	.59598E-2	7974.	8020.	1.921	32.949
.04440	.550	.81961E+5	.53605E-2	8330.	7478.	1.665	33.436
.05390	.550	.78421E+5	.49105E-2	8602.	6535.	1.478	33.798
.07201	.550	.71816E+5	.43434E-2	8823.	5958.	1.325	34.193
.08522	.550	.70043E+5	.41616E-2	8944.	5669.	1.251	34.310
.10260	.550	.53531E+5	.32747E-2	8698.	6125.	1.374	34.433
.11837	.550	.36851E+5	.23792E-2	8284.	6881.	1.589	34.510
.13384	.550	.24203E+5	.16671E-2	7828.	7664.	1.833	34.560

TABLE 9.4 CONT.

X/DB	R/DB	P PSF	RHO SLUGS/FT**3	T DEG.R	V FPS	M	S/R
.06709	.600	.77416E+5	.58882E-2	7442.	9085.	2.290	32.360
.07651	.600	.72601E+5	.52130E-2	7751.	8380.	2.045	32.904
.08196	.600	.71212E+5	.49494E-2	7937.	7932.	1.901	33.181
.10551	.600	.54660E+5	.35795E-2	8256.	7058.	1.636	33.941
.13300	.600	.37523E+5	.25121E-2	8060.	7306.	1.718	34.254
.15827	.600	.26188E+5	.18317E-2	7751.	7810.	1.883	34.372
.10472	.650	.69379E+5	.57707E-2	6964.	9984.	2.646	31.765
.10581	.650	.67373E+5	.56569E-2	6919.	10052.	2.676	31.730
.11294	.650	.60591E+5	.48810E-2	7113.	9598.	2.497	32.228
.12100	.650	.54075E+5	.42344E-2	7244.	9249.	2.368	32.504
.13018	.650	.47817E+5	.36476E-2	7362.	8892.	2.243	32.985
.14090	.650	.41806E+5	.31142E-2	7469.	8564.	2.132	33.345
.15372	.650	.36108E+5	.26439E-2	7541.	8328.	2.054	33.655
.16933	.650	.30506E+5	.22262E-2	7535.	8242.	2.031	33.893
.18892	.650	.24961E+5	.18390E-2	7455.	8321.	2.065	34.069
.15132	.700	.54666E+5	.53747E-2	6155.	11447.	3.322	30.648
.15785	.700	.49648E+5	.46344E-2	6390.	10931.	3.085	31.218
.16916	.700	.42572E+5	.37171E-2	6674.	10281.	2.797	32.020
.18347	.700	.36082E+5	.30603E-2	6795.	9933.	2.661	32.475
.20137	.700	.29989E+5	.24729E-2	6909.	9561.	2.523	32.958
.22488	.700	.24242E+5	.19543E-2	6989.	9253.	2.417	33.414
.20865	.750	.44021E+5	.49507E-2	5556.	12394.	3.862	29.729
.22225	.750	.36907E+5	.38245E-2	5899.	11740.	3.508	30.669
.24191	.750	.30026E+5	.28735E-2	6227.	10995.	3.152	31.649

Section 10

NOMENCLATURE

Symbol	Definition
a	coefficient in curve fit of γ^*
b	coefficient in curve fit of γ^*
B	Planck's black-body function
c	specie concentration
c	speed of light
C_D	drag coefficient
C_p	specific heat at constant pressure
D_B	base diameter
D	dissociation energy
e	internal energy
E_t	total energy emission rate per unit volume
f	u/u_e
f_{el}	electronic oscillator strength
f_{nm}	transition oscillator strength
f(r)	equation of bow shock in subsonic program
g	h/h_e
g(r)	equation of the body in subsonic program
h	static enthalpy
h	Planck's constant

Symbol	Definition
$h(x)$	equation of upper boundary in subsonic program
H	total enthalpy
I	radiant intensity
J_T	total equilibrium radiance
k	thermal conductivity
k	Boltzmann constant
l	distance along characteristic line
l	$\rho\mu/\rho_w\mu_w$
L	thickness of isothermal layer
M	Mach number
M	mixture molecular mass
n	distance normal to body surface
N	particle density
N_o	Avogadro's number
p	pressure
Pr	Prandtl number
$\dot{q}$	heat transfer
$q_{v'v''}$	Franck-Condon factor
Q	conduction plus radiation heat transfer
r	radial polar coordinate
$\bar{r}$	internuclear separation

Symbol	Definition
R	gas contstant
R	r/r_B in viscous analysis
R_B	base radius
R_N	nose radius
Re	Reynolds number
$Re(\bar{r})$	factor allowing for electronic transition moment with internuclear separation
s	wetted length
s	radiation path length
S	entropy, made dimensionless by gas constant R
T	temperature
u	velocity component
v	velocity component
V	total velocity
V	transformed normal coordinate in viscous flow analysis
x	axial coordinate
x	mole fraction
Z	compressibility factor
α	absorptance of surface
β	pressure gradient parameter $= 2\xi (du_e/d\xi)/u_e$
$\bar{\gamma}$	ratio of specific heats $= h/e$

Symbol	Definition
γ^*	$\equiv \rho(\partial p/\partial \rho)_S/p$
Γ	radiation coupling parameter
δ	boundary layer thickness
δ^*	boundary layer displacement thickness
Δ	shock detachment distance
ϵ	density ratio across normal shock, ρ_∞ / ρ_s
ϵ	emissivity of gas volume increment
η	transformed coordinate
θ	flow direction
θ	boundary layer momentum thickness
θ	angle from body normal (spherical coordinates) for radiation
κ	absorption coefficient of gas
λ	wave length
μ	fluid viscosity
μ	Mach angle
ν	wave number
ξ	transformed coordinate
ρ	fluid density
τ	viscous stress tensor
τ	transmittance of gas for radiant energy

Symbol	Definition
ϕ	angle around body normal (spherical coordinates) for radiation
$\varphi(r)$	Lennard-Jones potential
Φ	dissipation function
ψ	inviscid flow stream function

Subscripts

B	body
c	convective
c	classical
e	boundary layer outer edge
HG	hot gas
i	species
N	nose
o	standard conditions
R	radiation
s	shock
st	stagnation point
S	constant entropy
x, r	partial derivatives
w	surface
ξ, η	partial derivatives
ϑ	wave number
∞	free stream conditions